XFEM-based cycle-by-cycle simulation of fatigue crack growth

Louis Muys

Supervisors: Prof. dr. ir. Wim De Waele, Prof. Stijn Hertelé
Counsellor: Jie Zhang

Master's dissertation submitted in order to obtain the academic degree of
Master of Science in Electromechanical Engineering

Department of Electrical Energy, Metals, Mechanical Constructions & Systems
Chair: Prof. dr. ir. Luc Dupré
Faculty of Engineering and Architecture
Academic year 2016-2017

GHENT
UNIVERSITY

XFEM-based cycle-by-cycle simulation of fatigue crack growth

Louis Muys

Supervisors: Prof. dr. ir. Wim De Waele, Prof. Stijn Hertelé
Counsellor: Jie Zhang

Master's dissertation submitted in order to obtain the academic degree of
Master of Science in Electromechanical Engineering

Department of Electrical Energy, Metals, Mechanical Constructions & Systems
Chair: Prof. dr. ir. Luc Dupré
Faculty of Engineering and Architecture
Academic year 2016-2017

GHENT
UNIVERSITY

Preface

As this dissertation marks the last step in obtaining the academic degree of Master of Science in Electromechanical Engineering at Ghent University, I would like to use this opportunity to thank some of the people who have played a significant role over the past years and especially those who were essential to this work.

First of all, I would like to thank my promotors prof. Wim De Waele and prof. Stijn Hertelé, whose engaging courses over the past years aroused my interest and convinced me to choose this thesis subject. Their professional guidance and interesting insights over the past year were crucial in order to obtain a good and professional result.

Likewise, I would like to thank Jie Zhang for his professional guidance, for being available in case I experienced any issues and for the occasional brief conversations in Dutch. Moreover, this dissertation would never have succeeded without the experimental work of Steven De Tender. Last but not least, I want to thank Nahuel Micone for taking the effort to extract the data from Steven's work and to post-process it to my needs.

Next to this, I would like to thank my parents for supporting me since day one. I am also grateful to my girlfriend Lieselotte for her willingness to spend numerous hours together working at our theses.

XFEM-based cycle-by-cycle simulation of fatigue crack growth

Louis Muys

Supervisors: Prof. dr. ir. Wim De Waele, Prof. Stijn Hertelé
Counsellor: Jie Zhang

Master's dissertation submitted in order to obtain the academic degree of
Master of Science in Electromechanical Engineering

Department of Electrical Energy, Metals, Mechanical Constructions & Systems
Chair: Prof. dr. ir. Luc Dupré
Faculty of Engineering and Architecture
Academic year 2016-2017

Abstract: In variable amplitude fatigue, overloads can severely retard subsequent crack propagation for a number of cycles. This retardation effect has to be taken into account in order to avoid an overly conservative fatigue lifetime assessment. The category of plastic zone models, consisting of the Wheeler models and the Willenborg models, is selected as the most suitable variable amplitude fatigue crack propagation model for predicting retardation, based on the need for a detailed and fast cycle-by-cycle simulation of high cycle fatigue for high strength low alloy (HSLA) steel. Based on the identified weaknesses of the existing models the extended Wheeler model and Willenborg model are developed in this work. It is concluded that the extended Wheeler model outperforms all other plastic zone models that were investigated. Furthermore, the Extended Finite Element Method (XFEM) is explored to take care of the conversion of the applied load to the stress intensity factor at the crack tip, which is needed as input in all plastic zone models. This enables the developed algorithms to be used for non-standardized specimen geometries.

Keywords: fatigue; variable amplitude; retardation; plastic zone; Wheeler; Willenborg; XFEM;

Extended abstract

Introduction

Offshore structures are continuously subjected to variable amplitude fatigue due to the varying loading conditions caused by wind, waves and currents. Under these conditions, crack growth retardation is often observed. This effect is absent in constant amplitude fatigue and is a consequence of load interaction, which means that previous fatigue cycles can an impact on subsequent crack growth [1]. If this retardation effect is not taken into account into the fatigue lifetime assessment, fatigue crack growth will be overestimated, leading to overly conservative inspection intervals or dimensioning.

Variable amplitude fatigue tests on small-scale specimens are performed in order to gain a better understanding about the retardation effect. Fatigue cycles applied in such experiments are often based on actual variable amplitude loading conditions. Input for the fatigue crack propagation analyses in this dissertation are based on the work of De Tender [2], who applied different sequences of block loads in which the stress intensity factor range ΔK is kept constant during each respective block. This is termed K-controlled loading. Two differently sorted sequences for two different high strength offshore steels are considered here. For each case retardation was observed [2]. K-controlled loading is however only feasible if a standardized specimen is used. In this is not the case, blocks are often defined by a constant force range ΔP, so called force-controlled loading.

Three main parts can be distinguished. In the first part, fatigue crack propagation models capable of describing the retardation effect will be examined and their performance will be compared. The input load history for all the considered models must be described in terms of K. In order to be able to use force-controlled input, transfer functions from P to K are required. This is explored in the second part. In the final part, the algorithms to conduct the fatigue crack propagation analyses are discussed for both K-controlled and force-controlled loading.

Variable amplitude fatigue crack propagation

A suitable model for the case considered must fulfil several requirements. The model has to be able to analyse a load history cycle by cycle because even a single overload can have a significant effect on subsequent crack growth. Moreover, the computational cost per cycle must be low and only a limited amount of experimental data should be required. After an extensive literature review, plastic zone models were selected as suitable candidates since they fulfil all requirements.

Plastic zone models

Essential input for all plastic zone models is the size of the plastic zone that is caused ahead of the crack tip due to plastic deformation. The size is dependent on load level, yield strength and the plastic zone size factor α. Two different approaches for estimating α are compared, namely the linear-elastic fracture mechanics (LEFM) approach and the strip yield (SY) approach. It is found that α is a function of normalized thickness τ, which is a measure of whether an assumption of plane strain or plane stress is justified.

Moreover, all plastic zone models share a common interpretation of how the retardation effect is caused. This is termed the load interaction concept and is based on the effect of a single overload. A single overload, characterized by $K_{\mathrm{max,OL}}$, causes a plastic zone of size $r_{\mathrm{p,OL}}$. Subsequent cycles, characterized by $K_{\mathrm{max}} < K_{\mathrm{max,OL}}$ will cause plastic zones of size $r_{\mathrm{p}} < r_{\mathrm{p,OL}}$. The load interaction concept states that as long as the plastic zone of subsequent cycles is embedded within the overload plastic zone, retardation will occur. The difference between r_{p} and the hypothetical plastic zone size r_{p}^{*} is used to quantify this effect.

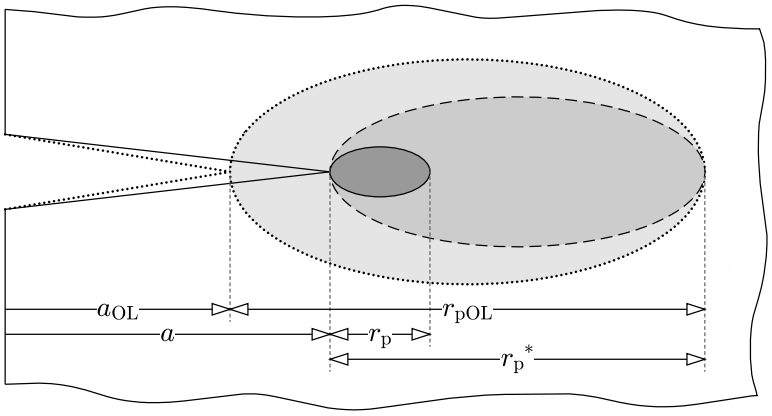

Figure 1.: Post-overload plastic zones considered in the load interaction concept

Plastic zone models can be further divided in two subcategories, namely the Wheeler models and the Willenborg models. Both approaches differ in terms of how r_{p} and r_{p}^{*} are combined to quantify the retardation effect. Within both subcategories, modified models exist which reduce the experimental nature or which attempt to improve accuracy by accounting for proximity to crack arrest. Some of their formulas are re-derived and key assumptions are questioned. One such assumption is the use of a constant α, which is clearly not true in every case according to Figure **??**. To avoid this assumption and to make the model applicable in the transition range between plane stress and plane strain, the extended Wheeler model and the extended Willenborg model are developed in this dissertation. The suggested models are clearly exceeding the state of the art.

Simulations

Next, performance of the considered plastic zone models is measured by comparing the simulated crack growth curves to the experimentally measured crack growth, which was also obtained by De Tender [2]. Based on the magnitude of the applied loads, it is reasoned that an assumption of plane strain might not be entirely correct.

A performance comparison of different Wheeler and Willenborg models is given in Figure 2 for a semi-random block load sequence. The modified Wheeler model (Mod. Wh.) and the generalized Willenborg model (Gen. Wb.) take into account the correction for proximity to crack arrest. The extended variants (Ext. Wh. and Ext. Wb. respectively) also take into account the dependency of α on normalized thickness τ. It is concluded that Willenborg models generally underestimate the amount of retardation more than Wheeler models. The most significant result however is the improvement that the extended models provide, especially the extended Wheeler model. Almost perfect correlation of the extended Wheeler model was not always found, but it did generally outperform all other plastic zone models.

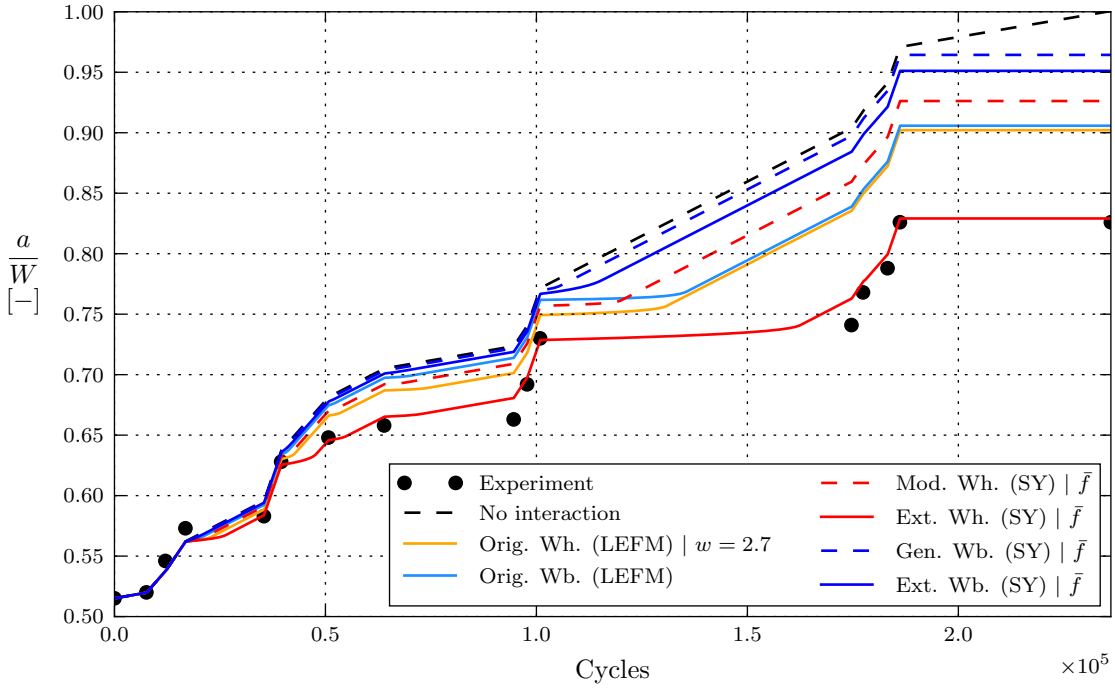

Figure 2.: Simulation result

Stress intensity factor calculation

In case of force-controlled loading, a transfer function from P to K is required. At present the finite element method (FEM) is most widely utilized due to its versatility and maturity of the theoretical basis. However, some serious drawbacks (such as computational cost) manifest if used in a cycle-by-cycle analysis of a propagating crack. Therefore, the possibilities of the Extended Finite Element Method (XFEM) were explored. In XFEM, accurate results can be obtained from a rather coarse mesh which does not need to be updated when the crack propagates. Moreover, the crack can have any arbitrary shape and is not bound to the mesh geometry.

In Figure 3 the results of an XFEM analysis for a standardized specimen are given and compared to the standardized solution. F is a geometry geometry factor which is responsible for the changing proportionality between P and K. It is a function of the dimensionless crack length a/W. Correlation is found to be near-perfect. This gives confidence that XFEM can also be applied for other specimen geometries.

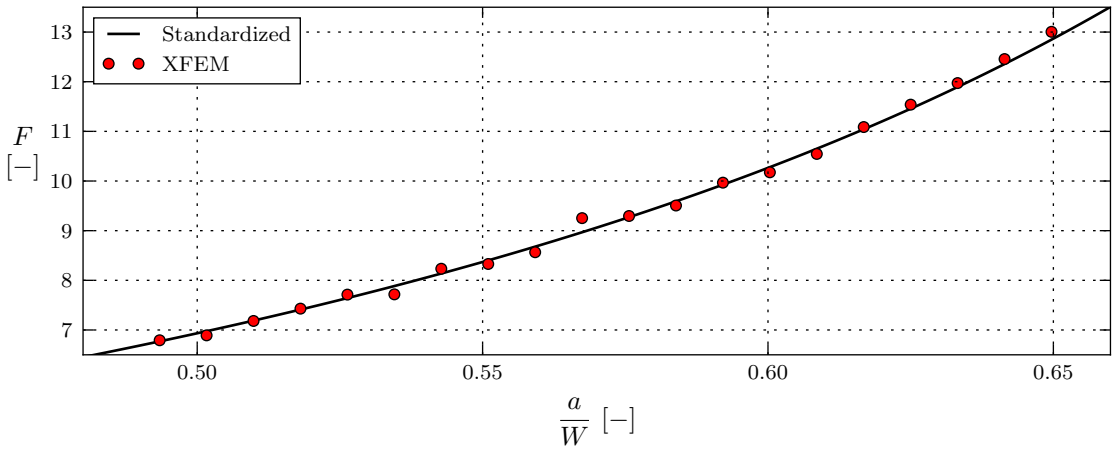

Figure 3.: Comparison

Software implementation

In the last part of this dissertation the algorithms to conduct the fatigue crack propagation analyses are discussed for both K-controlled and force-controlled loading. First, a cycle-by-cycle algorithm for K-controlled loading was developed. The stress intensity factor calculation was built as a separate module for the sake of modularity. At last, both parts of this dissertation are joined as the module is implemented in the global cycle-by-cycle algorithm without modifying program flow.

Contents

Nomenclature

Latin symbols

a	crack length	mm
a_0	initial crack length	mm
a_{OL}	crack length at application of overload	mm
C	Paris coefficient	
C_0	Paris coefficient for $R = 0$	
K	stress intensity factor	$\mathrm{MPa}\sqrt{\mathrm{m}}$
K_{min}	minimum stress intensity factor	$\mathrm{MPa}\sqrt{\mathrm{m}}$
K_{max}	maximum stress intensity factor	$\mathrm{MPa}\sqrt{\mathrm{m}}$
$K_{\mathrm{max,OL}}$	maximum stress intensity factor of overload cycle	$\mathrm{MPa}\sqrt{\mathrm{m}}$
K^*_{max}	hypothetical maximum stress intensity factor	$\mathrm{MPa}\sqrt{\mathrm{m}}$
K_{red}	stress intensity factor reduction	$\mathrm{MPa}\sqrt{\mathrm{m}}$
ΔK	stress intensity factor range	$\mathrm{MPa}\sqrt{\mathrm{m}}$
ΔK_{eff}	effective stress intensity factor range	$\mathrm{MPa}\sqrt{\mathrm{m}}$
ΔK_{th}	fatigue threshold	$\mathrm{MPa}\sqrt{\mathrm{m}}$
m	Paris law exponent	
m_0	Paris law exponent for $R = 0$	
n	strain hardening exponent	
N	number of cycles	
P	force	N
r_{p}	plastic zone size	mm
$r_{\mathrm{p,0}}$	reference plastic zone size	mm
$r_{\mathrm{p,OL}}$	overload plastic zone size	mm
r^*_{p}	hypothetical plastic zone size	mm
R	load ratio	
R_{eff}	effective load ratio	
R_{OL}	overload ratio	
R_{SO}	shut-off overload ratio	
t	specimen thickness	mm
W	specimen width	mm

Greek symbols

α	plastic zone size factor
η	global constraint factor
ϕ	retardation factor
λ	Willenborg correction factor
σ_y	yield strength
τ	normalized thickness

1. Introduction

Offshore structures are typically subjected to variable amplitude fatigue. The ambition of this work is to study and predict the involved effects in order to improve fatigue life estimations for such conditions.

1.1. Context

Offshore structures are continuously subjected to varying loading conditions caused by wind, waves and currents. It is said that the structure is subjected to variable amplitude fatigue. Under these conditions, effects such as crack growth retardation and acceleration are often observed. These so called load interaction effects are absent in constant amplitude fatigue [1]. In design of offshore structures often a fail-safe design philosophy is adopted [3]. Safe operation is based on regular non-destructive inspection intervals during which fatigue cracks might be revealed. The decision of whether or not to repair the structure or component and when to plan a next inspection then depends on a fatigue lifetime assessment, based on principles of fracture mechanics [4]. Predictions of crack growth propagation benefit from a more accurate simulation of the load interaction effects and their influence on fatigue lifetime. This may reduce the sometimes overly conservative safety factors involved, and lower material usage and cost [1].

In order to better understand load interaction effects, variable amplitude fatigue tests on small-scale specimens are often performed. Fatigue cycles applied in such experiments are often based on actual measurements of variable amplitude loading conditions. An example is given by Figure 1.1a, which shows the stresses that were observed at the bottom of an offshore wind turbine in the North Sea. This measured load history can in turn be reduced to a load history that is suitable for applying in a fatigue test, e.g. by distilling a number of discrete blocks in which all fatigue cycles are similar. An example is given in Figure 1.1b [1].

In this dissertation, input for the fatigue crack propagation analyses will be based on the work of De Tender [2], who considered the virtual case of an offshore wind turbine on a monopile structure in the North Sea. Using the JONSWAP wave spectrum, which is representative for conditions in the North Sea, De Tender was able to get an idea of the stresses that would occur in this virtual structure. Stresses were then translated to a representative stress intensity factor K that would occur in case a crack would be present in the virtual structure. Based on this, several realistic values for K were selected and block loads of a certain ΔK, the range in which K varies within a fatigue cycle, were defined. The idea is that loading conditions in the North Sea can be

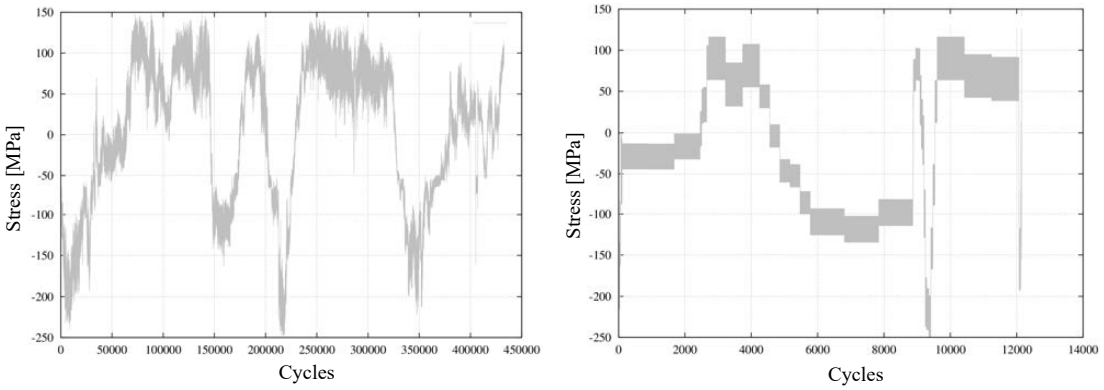

(a) measured (b) reduced

Figure 1.1.: Measured and reduced load history for an offshore wind turbine in the North Sea [1]

simulated by applying representative fatigue cycles to a test specimen [2].

De Tender also performed multiple variable amplitude fatigue tests based on the defined block loads. Three different sequences were examined, namely a low-high sequence (in which the blocks are applied from low to high ΔK), a low-high-low sequence and a semi-random sequence (in which blocks are randomly distributed). All three sequences were applied to two standardized test specimens made of different high strength offshore steels. Only the low-high-low and semi-random sequence will be examined in this dissertation because load interaction, more specifically retardation, was observed for these sequences [2].

In the test procedure the total crack growth increment to be achieved in each block was specified in advance. Due to retardation, a higher number of fatigue cycles than in constant amplitude fatigue was required to achieve a similar amount of crack growth. To facilitate this, an online crack length measurement technique was developed. This technique also made it possible to define cycles in terms of K, despite the fact that the testing equipment in fact applies a force, and that the relation between P and K changes as the crack grows. Conversion from the desired K to applied P was done using standardized formula for the test specimen, coupled with online fatigue crack growth measurements. [2, 5].

The described procedure of applying a constant ΔK is called K-controlled loading. It is only achievable if a standardized specimen is used. In case another geometry is used or in case crack growth in a real-life structure is to be predicted, standardized transfer functions will no longer be available. Often blocks of constant force range ΔP are considered then [1]. This is further referred to as force-controlled loading.

Based on the input load history, either K-controlled or force-controlled loading, fatigue crack propagation can be estimated. In order to accurately take into account variable amplitude loading conditions, each fatigue cycle must be analysed individually. Cycle-by-cycle fatigue crack propagation models were developed for aluminium

under flight loading conditions, since interaction effects were first observed in this industry in the 1970s [6].

1.2. Problem statement

In the previous section, a hint was already given to possible gaps in literature. One such gap concerns the fatigue crack propagation models. A suitable model for the case considered must fulfil several requirements. First of all, the model has to be able to analyse a load history cycle by cycle. Second, as this case concerns high cycle fatigue, computation time needed for every cycle must be limited. Third, the model should be able to yield satisfactory results using a limited amount of experimental data, since generation of this data is a time-consuming and costly process. As most models found in literature have been developed for aluminium in flight loading conditions, good correlation for offshore steel grades is not guaranteed.

Most of the existing models take K-values as input for their predictions. From the previous section it is clear that this poses a challenge for use in real-life scenarios. A modelling technique needs to be found that is able to convert forces to stress intensity factors. As this technique needs to be used in a cycle-by-cycle analysis, short calculation times are of the essence. However, this time limitation may not compromise accuracy.

As performance of the selected or developed fatigue crack propagation models needs to be examined, a software algorithm needs to be developed to process a large amount of fatigue cycles in an automated way. This is the subject of the third aspect of this work. Besides computation speed, the algorithm must meet some other requirements as well. The most important is modularity. It should be able to work with K-controlled or P-controlled input, with different propagation models and different techniques for calculating K, all without needing to change the global algorithm.

1.3. Outline of this dissertation

The body of this dissertation consists of three parts, a literature review, a case study and the software implementation. Within these parts, the three ambitions that were identified earlier are treated in separate chapters.

Concerning the first ambition, variable amplitude fatigue crack propagation models available in literature are discussed in Chapter 2. Special attention is paid to plastic zone models, and more specifically to estimating the plastic zone size, a parameter used in these models. Moreover, some of the formulas involved are re-derived as errors were found in literature. From this literature review, suitable models are selected and their performance is measured in Chapter 4, a case study with the experimental data introduced in Section 1.1. Within this chapter, a sensitivity analysis is done to gain knowledge about the different parameters involved. Afterwards, modifications to existing models are proposed and their performance is compared for different materials and load histories. The suggested modifications are clearly exceeding the state of the art.

The solution for calculating the stress intensity factor follows the same structure as the first ambition. In Chapter 3, a literature study is done and based on the stated requirements, a technique called extended finite element method is chosen. The performance of this technique is then tested in a case study in Chapter 5.

The third part of this dissertation, Chapter 6, treats the software algorithm that was developed in a rather abstract way. For more details about this part, the reader is referred to the software manual accompanying the code.

In the last chapter, Chapter 7, the main conclusions of this dissertation and its limitations are critically assessed and perspectives for future research are given.

Part I.

LITERATURE REVIEW

2. Modelling of variable amplitude fatigue crack propagation

2.1. Starting point – constant amplitude fatigue

Variable amplitude fatigue crack propagation models generally modify existing crack propagation models for constant amplitude fatigue. Therefore, a basic knowledge of those is required first. Generally, constant amplitude fatigue crack growth rate is assumed to be dependent on 2 out of the following 4 crack driving force parameters that characterize the applied constant amplitude loading. $K_{\max}$ denotes the stress intensity factor at the crack tip when the maximum load of the fatigue cycle is applied, while $K_{\min}$ corresponds to the minimum load. K is a function of applied load P, geometry and defect size or crack length a. Two derived crack driving force parameters are the stress intensity factor range ΔK and the load ratio R. Their relations are given in Eqs. (2.1)-(2.2) [7].

$$\Delta K = K_{\max} - K_{\min} \tag{2.1}$$

$$R = \frac{K_{\min}}{K_{\max}} \tag{2.2}$$

Generally, the derived crack driving force parameters are used. The constant amplitude crack growth rate can then be calculated by Eq. (2.3). N is the number of applied cycles, so $^{da}/_{dN}$ denotes the crack growth increment per cycle [7].

$$\frac{da}{dN} = f(\Delta K, R) \tag{2.3}$$

The function f is obtained experimentally. In such an experiment, usually the load ratio is fixed and the crack growth rate $^{da}/_{dN}$ is plotted against ΔK in a double logarithmic graph such as Figure 2.2. Usually, three stages can be distinguished in such a plot. A first stage is characterized by a fatigue threshold value ΔK_{th}, below which no fatigue crack propagation occurs. In the second stage, the relation appears linear on a double logarithmic scale. The third stage is related to unstable crack growth when $K_{\max}$ reaches a critical value K_c. Given a certain R-value, this is translated into an asymptotic increase of ΔK [4]. As the scope of this dissertation is high cycle fatigue, the first and second stage are of particular interest.

Paris equation Paris and Erdogan [8] described the second stage behaviour by Eq. (2.4). Two fitting parameters, namely the Paris exponent m and the Paris coefficient C

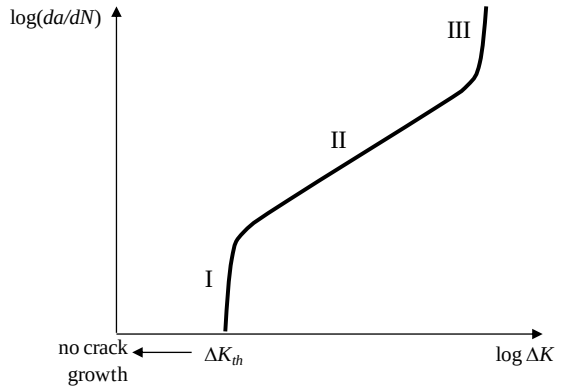

Figure 2.2.: Typical $^{da}/_{dN}$-ΔK relation for fixed R in a double logarithmic graph [4]

have to be determined experimentally. m is the slope of the linear relation in a double logarithmic graph and C is obtained from the intersection with the y-axis. Eq. (2.4) is conveniently termed the Paris equation from now on [9]. The Paris equation considered the second stage to be fairly independent of R and is therefore only dependent on ΔK [4].

$$\frac{da}{dN} = C \cdot \Delta K^m \tag{2.4}$$

Walker equation Literature indicates however that in some cases an influence of R can be observed. This is illustrated in Figure 2.3. The focus here is on the second stage. Generally the slope is constant but C is a function of R [10]. To account for this load ratio effect, the Walker equation is commonly used, given by Eq. (2.5). Its form is similar to the Paris equation, but Walker proposed to use a parameter ΔK_{eq}, which is an equivalent ΔK for $R = 0$ that causes the same crack growth as the actual $(\Delta K, R)$ combination. C_0 and m_0 are the Paris coefficient and exponent, respectively, for $R = 0$. The third fitting parameter, the Walker exponent γ, is found by consolidating the different straight lines (obtained for at least two different R values) on a double logarithmic plot of $^{da}/_{dN}$ versus ΔK_{eq}. If $\gamma = 1$, R has no effect on crack growth rate [9]. Dowling et al. concluded that the Walker equation yields superior results in comparison to other approaches. From an extensive study they observed a dependency of γ on σ_u, the ultimate tensile strength of the material. Values for γ typically ranged between 0.4 and 0.8. The higher σ_u, the more sensitive the material is to load ratio and the lower γ is [11].

$$\frac{da}{dN} = C_0 \cdot \Delta K_{\text{eq}}^{m_0} = C_0 \left[\frac{\Delta K}{(1-R)^{1-\gamma}} \right]^{m_0} \tag{2.5}$$

Accounting for multiple stages The need for a crack growth law with wider applicability encourages development of models capable of describing multiple stages or even all three. The Forman equation is one of the most well-known models for this purpose.

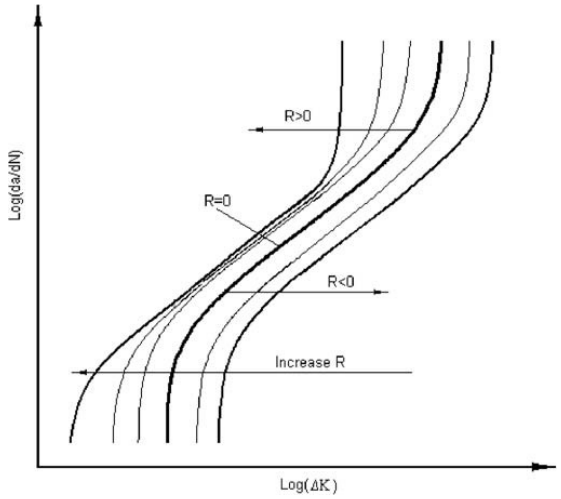

Figure 2.3.: Crack growth rate curves under different R-ratios [10]

However, as multiple fitting parameters are required, it is not suitable for the purpose of this dissertation. An extensive overview of this model and others can be found in the work of Beden et al. [9]. A major challenge in these models is the dependency of ΔK_{th} on R in the near-threshold region, as can be seen in Figure 2.3. Often, this is explained by the crack closure concept, introduced in Subsection 2.5.1.

2.2. Load interaction effects in variable amplitude fatigue

The best documented load interaction effect is that caused by a single overload introduced in between constant amplitude load cycles. The influence on crack propagation is shown in Figure 2.4 for multiple single overload cycles. After application of each overload a decrease of the rate at which the crack length increases can be observed. This phenomenon is termed retardation. After a number of cycles the crack growth rate approaches its steady state value and the retardation has vanished out. The overload ratio $R_{\mathrm{OL}} = {}^{K_{\mathrm{max,OL}}}/_{K_{\mathrm{max}}}$ is the major parameter for the amount of retardation [12].

In the experiment described in Figure 2.4 the overloads were applied sufficiently remote to ensure that retardation has vanished out before the next overload is applied. If this is not the case, additional interaction effects between overloads can occur as well. An extreme case consists of applying overloads following each other in an overload sequence. If the overload sequences last long enough, a regime for the higher overload fatigue cycles can develop. This is called block loading. Underloads can be applied as well, both isolated or following an overload. For the former an acceleration effect is reported in literature, but it is usually relatively small compared to retardation. However, when applied right after an overload, underloads can play a significant role as they reduce the retardation effect [12].

The distinction between single overloads, overload sequences and overload blocks in

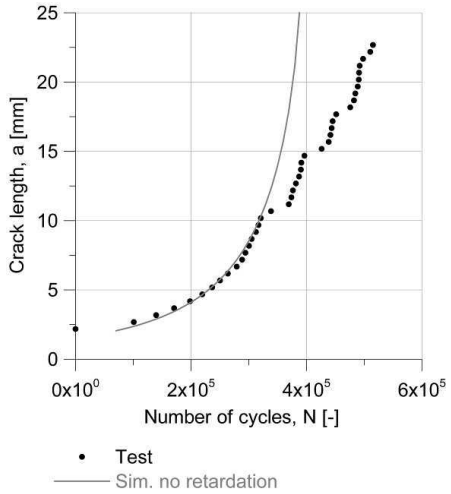

Figure 2.4.: Influence of single overloads on crack propagation [1]

K-controlled loading conditions is examined in literature. In Figure 2.5 it is observed that an overload block gives rise to more retardation then a single overload does. Additionally, the transition between both cases was examined by increasing the number of consecutive overload cycles. These experiments indicated that the amount of retardation approaches the limit case of a block overload for a number of overload cycle in the order of 10. Past this number, the length of the block no longer influences the amount of retardation [13].

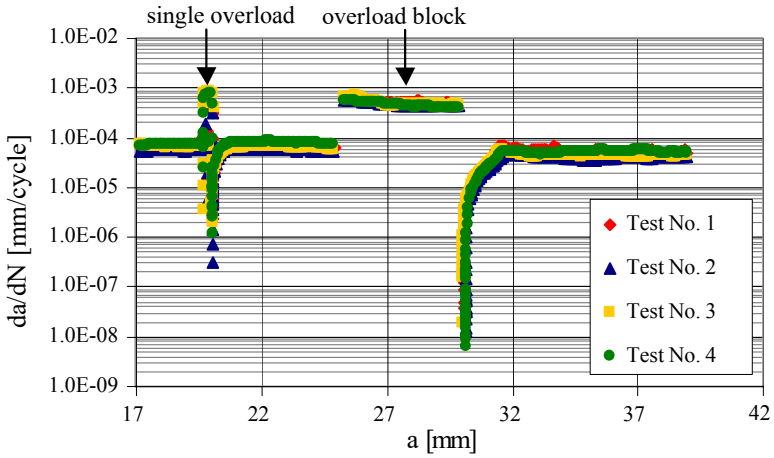

Figure 2.5.: Comparison of crack growth rate for a single overload versus an overload block (adapted from [13])

2.3. Overview of modelling approaches

From the previous section it can be concluded that most load interaction effects cause retardation. Consequently, overly conservative predictions are often obtained in variable amplitude loading when these effects are not taken into account [6]. Several modelling approaches and corrections to existing models have been developed. A schematic overview is given in Figure 2.6. A high-level distinction can be made based on the way the load history is processed.

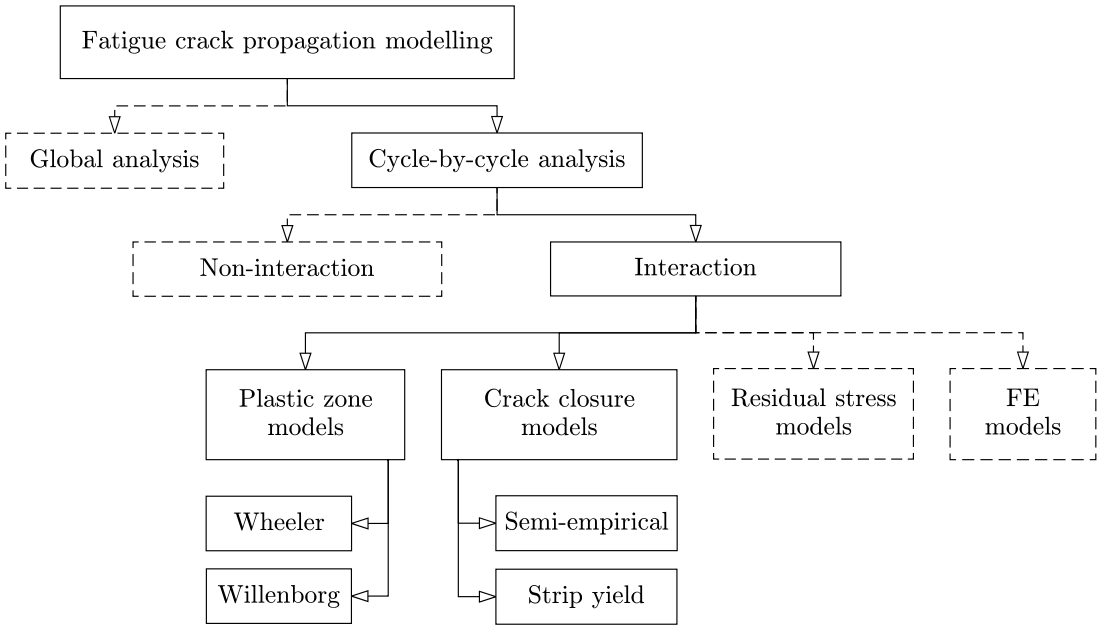

Figure 2.6.: Classification of available modelling approaches

Global analysis In a global analysis the load history is considered as a whole. The aim of this approach is to calculate only one stress intensity factor range based on the statistical description of the load spectrum. This single value should yield the same mean crack growth rate as using the full load spectrum. One of the earliest implementations was the root mean square (RMS) method, given by Eq. (2.6). This mean value can then be inserted in the Paris equation to get a global crack growth rate.

$$\Delta K_{\mathrm{rms}} = \sqrt{\frac{1}{N}\sum_{i=1}^{N}\Delta K_i^2} \tag{2.6}$$

Further models have been developed based on this method. In general, all global analysis models deliver acceptable results if the load sequence is uniformly stochastically distributed. This means that retardation by single overloads cannot be modelled by this approach as cycles are not examined individually [14].

Cycle-by-cycle analysis It should be clear by now that the load history has to be examined cycle by cycle to be able to capture load interaction effects of single overloads. The most basic form is the non-interaction cycle-by-cycle analysis. It is the foundation of all interaction cycle-by-cycle models.

Non-interaction model The non-interaction cycle-by-cycle approach basically sums up crack growth increments caused by every individual cycle based on the constant amplitude fatigue crack growth rate. The formula for this linear damage accumulation approach is given by Eq. (2.7). It is clear that dependency of the crack growth increment in a given cycle on the preceding load history is ignored.

$$a_n = a_0 + \sum_{i=1}^{n} f(\Delta K_i, R_i) \tag{2.7}$$

Satisfactory predictions are only found when overall load interaction is negligible or when retardation and acceleration phenomena cancel out each other [14].

Interaction models The remainder of this chapter will concentrate on available crack growth prediction models that account for load interaction phenomena, the so-called *interaction models*. A classification will be made based on their physical concept. Although these models do not impose any requirements with respect to the load sequence or material, it has to be noted that they have been primarily developed for simulating flight loading of aluminium structures [15]. Generally, interaction models can be divided into four main categories. The most well-known model categories, **plastic zone models** and **crack closure models**, differ conceptually in their choice of which crack region to consider. While the former is based on plasticity ahead of the crack-tip, the latter concentrates on the wake of the crack. Both modelling approaches will be thoroughly discussed in the following sections. The remaining models mentioned in Section 2.6 will not be discussed in detail, therefore a short review is given here. **Residual stress models** were developed as an alternative to crack closure prediction techniques and simulate the residual stresses in front of the crack tip in a detailed manner. Some well-known residual stress models are *UniGrow*, *Lang's model* and *AfGrow*. All have in common that they require a thorough and lengthy experimental calibration of the model [14, 15]. **Finite elements models** offer more of a brute force approach. They provide a complete stress tensor, strain tensor and displacement vector at any point of the model at any applied load level. Hence, any crack driving force parameter related to the stress/strain/displacement behaviour of a cracked body can be determined. Both two-dimensional and three-dimensional analyses are common but require immense computing power to get reasonable total analysis times for regular load histories [14, 15].

2.4. Plastic zone models

Development of plastic zone models – alternatively called crack tip plasticity models – started in the early 1970s [6]. Differences between non-interaction predictions and experiments were explained by the load interaction zone concept [16], which attributes load interaction effects to the plastic zone (PZ) in front of the crack tip. Therefore, a correct estimation of the plastic zone size is essential, as discussed in Subsection 2.4.1. Afterwards, the load interaction concept itself is explained in Section 2.4.2. Based on the load interaction zone concept, two main modelling approaches emerged, namely the Wheeler model (Subsection 2.4.3) and the Willenborg model (Subsection 2.4.4). Both models started as a means for modelling the effect of a single overload [6, 16]. Later, modifications were introduced to account for proximity to crack arrest [17–20]. Aiming to accommodate for more varied loading conditions, corrections for overload-underload and overload interactions have also been investigated as well [21–23].

2.4.1. Plastic zone size estimation

Although linear-elastic stress analysis of sharp cracks predicts infinite stresses at the crack tip, real materials exhibit finite stresses because the crack tip radius must be finite. Additionally, stress relaxation happens due to plastic deformation at the crack tip [7], causing a plastic zone of size r_p. Generally, two approaches for estimating r_p are distinguished in literature [7]. Both are based on the concepts of linear-elastic fracture mechanics (LEFM), but the former uses the LEFM stress field solutions [4, 24], while the other moves away from this and calculates the stress field using the strip yield (SY) model [25]. To keep things simple, the approaches will be termed the LEFM approach and the strip yield (SY) approach for the remainder of this dissertation.

Generally, the form of Eq. (2.8) is employed regardless of the chosen approach. r_p is a function of the squared ratio of K over σ_y, the yield strength of the material. A dimensionless plastic zone size factor α is introduced to express the influence of geometry and material properties [26–28].

$$r_\mathrm{p} = \alpha \left(\frac{K}{\sigma_\mathrm{y}} \right)^2 \tag{2.8}$$

2.4.1.1. LEFM approach

Using LEFM, Irwin [24] derived a first-order plastic zone size estimate r_y by determining the radius at which the normal stress on the crack plane, $\sigma_{22} = {}^{K}/\sqrt{2\pi r}$, exceeds σ_y, thereby assuming plane stress conditions. As stresses within this yield zone cannot exceed the material's yield strength, redistribution must take place in order to satisfy equilibrium. This is illustrated in Figure 2.7. As the load bearing capacity of the plastic zone decreases, the resulting (second-order) plastic zone size r_p must increase. In fact, it doubles in size. In plane strain, the triaxial stress state increases the tensile stress needed for yielding, which results in a smaller plastic zone [4, 24]. The results are given in Eq. (2.9). Often, the plane stress plastic zone size is represented as $r_{\mathrm{p},0}$ and used as

reference [26, 27]. Early plastic zone models opted for the LEFM approach. Wheeler adopted the plane strain value, while Willenborg believed that plane stress was more accurate [6, 16].

$$r_\mathrm{p} = \begin{cases} \dfrac{1}{\pi}\left(\dfrac{K}{\sigma_\mathrm{y}}\right)^2 = r_{\mathrm{p},0}, & \text{plane stress} \\ \dfrac{1}{3\pi}\left(\dfrac{K}{\sigma_\mathrm{y}}\right)^2 = \dfrac{1}{3} r_{\mathrm{p},0}, & \text{plane strain} \end{cases} \tag{2.9}$$

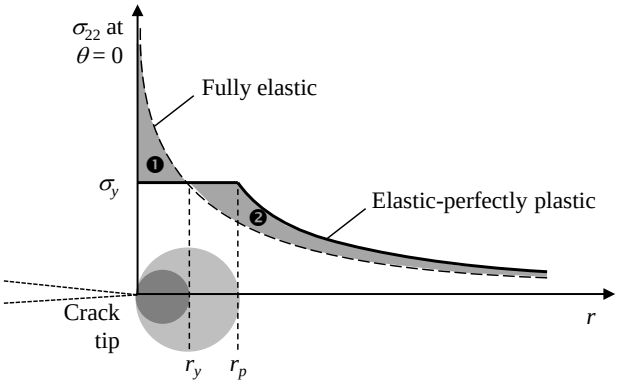

Figure 2.7.: Visual representation of the LEFM approach [4]

In some cases, the assumption of plane stress or plane strain is an acceptable approximation, while in others, an intermediate value would be better suited. For the sake of uniformity, normalized thickness $\tau = t/r_{\mathrm{p},0}$ is introduced here. When the material thickness t is small relative to $r_{\mathrm{p},0}$, τ is small and plane stress can be assumed, and vice versa. First, a rule of thumb was introduced that justifies plane stress if $\tau \leq 0.5$, meaning that r_p must be at least two times the material thickness [29]. Later, Eq. (2.10) was proposed to describe the thickness effect in more detail when neither of the assumptions is applicable [26, 27]. It is basically a linear interpolation between plane stress and plane strain values in case neither assumption is valid.

$$\alpha = \begin{cases} \dfrac{1}{\pi}, & \text{for } \tau \leq 1 \\ \dfrac{1}{3\pi} + \dfrac{2}{3\pi}\dfrac{2.5\pi - \tau}{2.5\pi - 1}, & \text{for } 1 \leq \tau \leq 2.5\pi \\ \dfrac{1}{3\pi}, & \text{for } \tau \geq 2.5\pi \end{cases} \tag{2.10}$$

2.4.1.2. Strip yield approach

The strip yield model was developed by Dugdale [25] considering small-scale yielding conditions as a complement to linear elastic fracture mechanics. The model assumes

that all deformation concentrates in a strip in front of the crack [4]. Elastic-plastic behaviour is approximated by superimposing two elastic solutions for a through crack of length $2a + 2r_\mathrm{p}$ in an infinite plate in plane stress. Remote tension over the entire crack length is supplemented with closure stresses at both crack tips over a length r_p, the length of the long, slender plastic zone. The closure stress is equal to the σ_y. This is visualized in Figure 2.8. By using superposition, finite stresses are obtained and the stress singularity at the crack tips of the real crack with length $2a$ is avoided. By imposing that K due to remote tension must cancel the closure K at the real crack tips, $\alpha = \pi/8$ is found [7]. This value is substantially different from the LEFM approach. Again, the plane stress plastic zone size $r'_{\mathrm{p},0}$ ($\neq r_{\mathrm{p},0}$) can be used as reference.

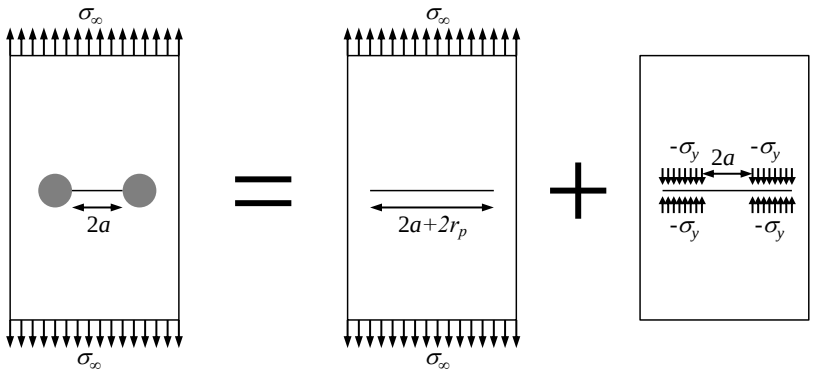

Figure 2.8.: Visual representation of the strip yield model (modified from [4])

Guo [28] extended the strip yield model three-dimensionally to obtain valid solutions for plates of finite thickness. A dimensionless global constraint factor η was introduced to simulate effects of out-of-plane and in-plane constraints in a two-dimensional analysis, as can be seen in Eq. (2.11).

$$r_\mathrm{p} = \frac{\pi}{8}\left(\frac{K}{\eta \cdot \sigma_\mathrm{y}}\right)^2 \tag{2.11}$$

For elastic-perfectly plastic materials, $\eta = 1$ in plane stress and the reference value $r'_{\mathrm{p},0}$ of the two-dimensional strip yield model is found. As plate thickness increases, η approaches the plane strain value $\eta_\mathrm{max} = 1/1-2\nu$, valid for a perfectly elastic material [28]. ν is the Poisson's ratio of the material. The strip yield limit values are summarized in Eq. (2.12).

$$r_\mathrm{p} = \begin{cases} \dfrac{\pi}{8}\left(\dfrac{K}{\sigma_\mathrm{y}}\right)^2 = r'_{\mathrm{p},0}, & \text{plane stress} \\ \dfrac{\pi(1-2\nu)^2}{8}\left(\dfrac{K}{\sigma_\mathrm{y}}\right)^2, & \text{plane strain} \end{cases} \tag{2.12}$$

In between plane stress and plane strain, η is highly dependent on stress levels and requires solving an integral equation. A unified curve of η against normalized thickness

$\tau' = {}^{t}/_{r'_{p,0}}$ was obtained, independent of material yield strength, stress level and geometry. For real materials, a minor dependency on the strain hardening exponent n – related to the Ramberg-Osgood stress-strain relationship [30] – was observed. In Figure 2.9, an elastic-perfectly plastic material ($n = \infty$) is compared to a real strain hardening material with $n = 10$. As a strain hardening material is able to carry a higher stress in regions where the yield strength is exceeded, a smaller plastic zone is generated so η will be higher. These curves were also validated by finite element analysis [28].

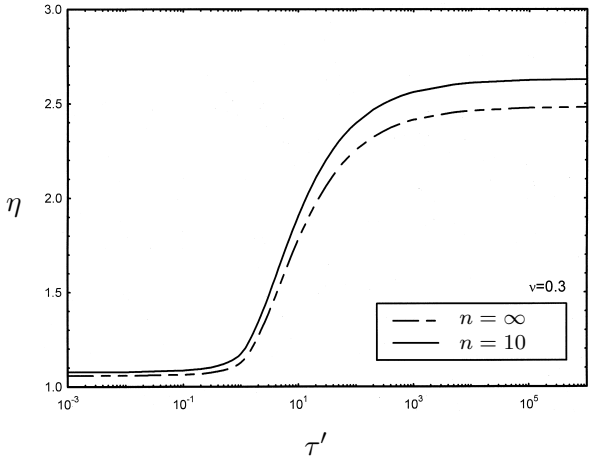

Figure 2.9.: Influence of τ' and strain hardening on η (adapted from [28])

2.4.1.3. Comparison

In Figure 2.10, the different approaches mentioned above for estimating α are compared.[1] In order to do this, τ' has to be transformed to τ, so that $\eta(\tau')$ can be written as $\eta(\tau)$. The proportionality is given in Eq. 2.13.

$$\tau = \frac{\pi^2}{8}\tau' \tag{2.13}$$

First, the aforementioned rule of thumb for plane stress ($\tau \leq 0.5$) seems to be valid. In plane stress, the LEFM estimation largely agrees with that of the three-dimensional SY approach. The original SY plane stress value, however, deviates significantly as the effect of in-plane stress ratio was not taken into account by Dugdale [28]. This value thus only provides an upper bound. In plane strain, a larger deviation between both approaches is observed. The three-dimensional SY model predicts a smaller plastic zone size (almost half) due to an increased constraint on the crack tip by taking into account both the effect of T-stress and strain hardening [28]. Additionally, the width of the transition zone is different for both approaches ($1 < \tau < 10$ for LEFM vs. $1 < \tau < 100$

[1] Data from the three-dimensional SY model was extracted from Figure 2.9 instead of solving the integral equation [31]

for SY) as well as their α-values. Note that the SY limit values were calculated for an elastic-perfectly plastic material. The reason that the curve for $n = 10$ can fall below this limit value was discussed above.

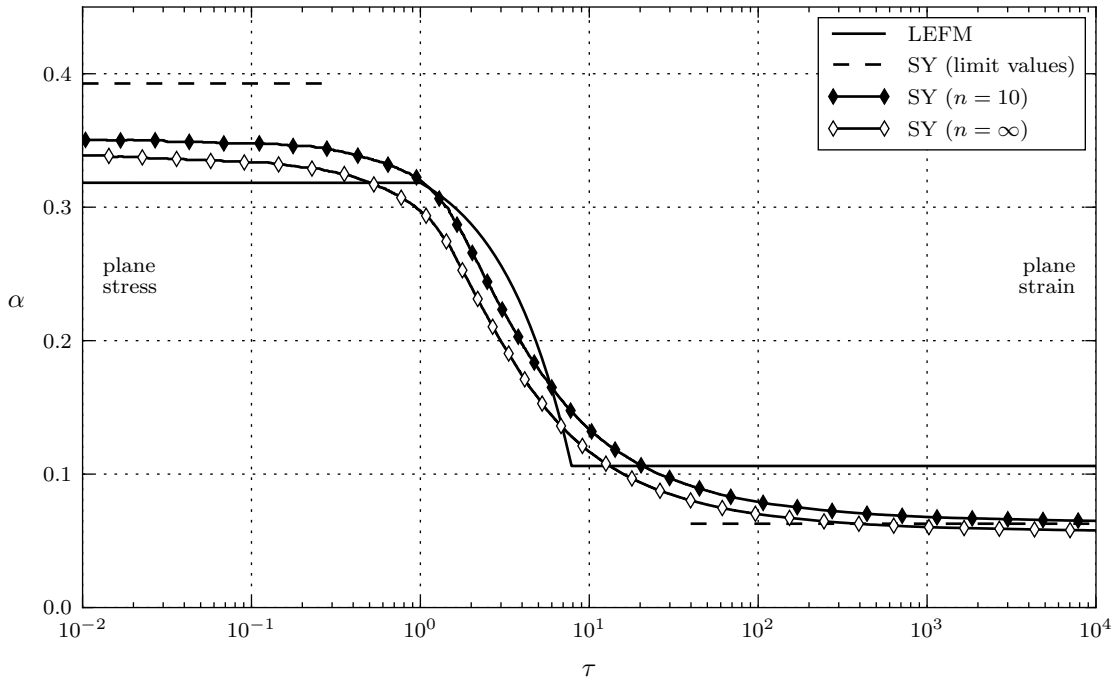

Figure 2.10.: Comparison of approaches for estimating α

2.4.2. Load interaction zone concept

Plastic zone models account for retardation and related effects by considering the plastic zone state in front of the crack tip, shown in Figure 2.11. This state contains the locations of all relevant elastic-plastic yield interfaces caused by current or previous fatigue cycles, and is therefore a representation of relevant loading history. In case of a single overload at crack length a_{OL}, the material yields in the vicinity of the crack tip and a plastic zone of size $r_{\mathrm{p,OL}}$ is caused. $r_{\mathrm{p,OL}}$ is calculated from $K_{\mathrm{max,OL}}$, which is known or can be derived from the characteristic overload ratio $R_{\mathrm{OL}} = {}^{K_{\mathrm{max,OL}}}/_{K_{\mathrm{max}}}$.

Subsequent nominal loads, applied at increasing crack length a, will cause a plastic zone of size r_{p} in front of the propagating crack tip. Since $r_{\mathrm{p}} < r_{\mathrm{p,OL}}$, the current PZ will be fully embedded in the overload PZ for a certain number of cycles. It is assumed that crack growth rate is reduced during these cycles [6, 16]. Once the current elastic-plastic interface intersects the one caused by the overload, the current PZ becomes the relevant PZ and the interaction effect disappears until a new overload event happens, upon which the above is repeated.

Based on the above reasoning, the condition for retardation was defined $a_{\mathrm{OL}} + r_{\mathrm{p,OL}} >$

$a + r_\mathrm{p}$ [6]. This led to the definition of r_p^*, given in Eq. (2.14) [16]. r_p^* represents the hypothetical 'no interaction' plastic zone size, more specifically the size that the current PZ should have in order for it to touch the overload elastic-plastic interface. The equivalent condition for retardation then becomes $r_\mathrm{p}^* > r_\mathrm{p}$. As the crack propagates, r_p^* will approach r_p and the interaction effect will vanish.

$$r_\mathrm{p}^* = r_\mathrm{p,OL} - (a - a_\mathrm{OL}) \tag{2.14}$$

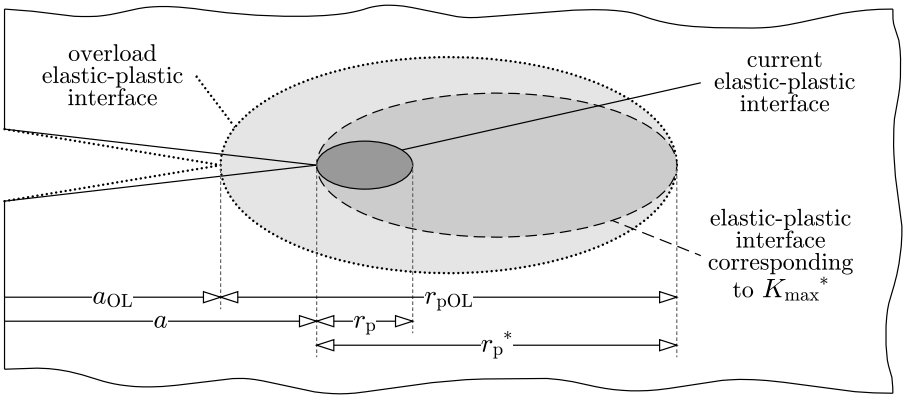

Figure 2.11.: Post-overload plastic zones considered in the load interaction concept

Willenborg proposed to quantify the retardation effect by using a combination of both values, since their difference represents the proximity of both elastic-plastic interfaces [16]. Later, the hypothetical stress intensity factor K_max^*, Eq. (2.15), corresponding to r_p^* was introduced [17]. It has to be noted that this proportionality in Eq. (2.15) is only valid when a constant α-factor is assumed. Load interaction occurs when $K_\mathrm{max}^* > K_\mathrm{max}$.

$$K_\mathrm{max}^* = K_\mathrm{max,OL}\sqrt{\frac{r_\mathrm{p}^*}{r_\mathrm{p,OL}}} = K_\mathrm{max,OL}\sqrt{1 - \frac{a - a_\mathrm{OL}}{r_\mathrm{p,OL}}} \tag{2.15}$$

Although Wheeler models, Subsection 2.4.3, and Willenborg models, Subsection 2.4.4, are based on the same load interaction zone concept, two main differences exist. First, r_p and r_p^* (or K_max and K_max^*) are differently combined in order to quantify retardation. Both quantifications represent the proximity of elastic-plastic interfaces. Second, both models modify the crack growth rate differently, either direct or indirect, respectively. In order to show the analogy between both models, an indirect formulation of the Wheeler model will also be given.

2.4.3. Wheeler models

Wheeler [6] modified the non-interaction model by introducing a retardation factor ϕ, which takes a positive value below 1, with 1 being the case of no interaction. The Wheeler model does not alter input for the crack growth law (e.g. ΔK and R), so the

straightforward Paris equation can be employed, provided that it was obtained under the correct load ratio. This is shown in Eq. (2.16), in which n is the number of applied cycles. Load interaction effects can potentially be simulated as the net crack growth rate is no longer independent of prior load history.

$$a_n = a_0 + \sum_{i=1}^{n} \phi_i \cdot C(R)(\Delta K_i)^m \tag{2.16}$$

As shown in (2.17), the retardation effect can also be expressed indirectly by introducing ΔK_{eff}, the effective ΔK, and assuming the Paris law [19, 20].

$$a_n = a_0 + \sum_{i=1}^{n} C(R)(\Delta K_{\text{eff},i})^m \quad \text{with} \quad \Delta K_{\text{eff},i} = \phi_i{}^{\frac{1}{m}} \Delta K_i \tag{2.17}$$

2.4.3.1. Retardation factor

A relation for ϕ is obtained by combining $K_{\max}$ and $K^*_{\max}$ as a ratio and raising it to the power $2w$, as shown in Eq. (2.18) [17, 19]. It clearly shows the analogy with Willenborg models, which are discussed further in this chapter. The shaping exponent w allows for correlation with test data or can be obtained theoretically. For $w = 0$, the non-interaction model is found as $\phi = 1$.

$$\phi = \begin{cases} \left(\dfrac{K_{\max}}{K^*_{\max}}\right)^{2w} & \text{for} \quad K^*_{\max} > K_{\max} \\ 1 & \text{for} \quad K^*_{\max} \leq K_{\max} \end{cases} \tag{2.18}$$

However, the relation as originally reported by Wheeler [6] is given by Eq. (2.19) and expressed in terms of crack size and plastic zone size. Eq. (2.18) was only introduced later, hence the factor 2 in the exponent. It was developed as an attempt to show the similarity to Willenborg models [15, 17, 19]. However, in line with previous remarks, the original form, Eq. (2.19) and equivalent form, Eq. (2.20), are preferred as these do not require any assumptions on α.

$$\phi_{wh} = \begin{cases} \left(\dfrac{r_{\text{p}}}{a_{\text{OL}} + r_{\text{pOL}} - a}\right)^{w} & \text{for} \quad a_{\text{OL}} + r_{\text{pOL}} > a + r_{\text{p}} \\ 1 & \text{for} \quad a_{\text{OL}} + r_{\text{pOL}} \leq a + r_{\text{p}} \end{cases} \tag{2.19}$$

$$= \begin{cases} \left(\dfrac{r_{\text{p}}}{r^*_{\text{p}}}\right)^{w} & \text{for} \quad r^*_{\text{p}} > r_{\text{p}} \\ 1 & \text{for} \quad r^*_{\text{p}} \leq r_{\text{p}} \end{cases} \tag{2.20}$$

In case that alpha is assumed independent of load level, all three presented forms are fully equivalent.

2.4.3.2. Shaping exponent

Originally, the shaping exponent w had to be determined experimentally for a given material and type of loading, as dependence on these factors was observed [6, 32, 33]. This experimental constant was, besides being impractical, not feasible in general. To avoid such disadvantages, a theoretical derivation was developed later [19, 20].

Experimental approach Wheeler's intent was to determine the shaping exponent w by fitting the model to experimental data. Table 2.1 gives an idea of the range of values that can be expected. He observed that w is dependent on the material (e.g. yield strength) and the type of loading sequence [6]. Both observations were confirmed by Alawi [32], who examined three different steels under various random loading distributions. Sheu et al. [33] observed that w increases with increasing overload ratio $R_{\mathrm{OL}} = {}^{K_{\mathrm{max,OL}}}/_{K_{\mathrm{max}}}$ and initial crack length. Table 2.1 gives an indication of experimentally obtained shaping exponents for different materials found in literature.

Table 2.1.: Different experimentally obtained Wheeler shaping exponents

Material	Variant	w	Source
Steel	D6ac	1.3	Wheeler [6]
Titanium	Ti-6Al-4V	3.4	Wheeler [6]
Aluminium	5083-O	0.94–2.19	Sheu et al. [33]
	6061-T651	1.36–1.98	Sheu et al. [33]

Remark 2.1. Some observed dependencies can potentially be explained by the chosen plastic zone shape factor, which is often wrongly taken as a constant. For example, a higher R_{OL} is associated with a higher $K_{\mathrm{max,OL}}$, which may become so high that the plane strain assumption [6] is no longer valid and the real plastic zone size will be larger than predicted.

Theoretical approach – modified Wheeler model Gray and Gallagher [19, 20] recognised the shortcomings of an experimentally obtained shaping exponent w. Although such an exponent may provide good correlation with a particular set of experimental data, its generic application is not feasible. Therefore, they proposed a theoretical relation for determining w without relying on data fitting. It is based on the observation that crack arrest can take place immediately after an overload when the overload ratio R_{OL} is above a specific value R_{SO}, the shut-off overload ratio. Table 2.2 gives an idea of possible R_{SO} values.

Gray and Gallagher reasoned that crack arrest occurs because the effective ΔK is below the threshold value ΔK_{th} of the material. They examined the limiting case of $R_{\mathrm{OL}} = R_{\mathrm{SO}}$. Since crack arrest happens right after an overload, $a = a_{\mathrm{OL}}$. The

Table 2.2.: Overload ratio above which crack arrest occurs

Material	Variant	R_{SO}	Source
Steel	4340	2.3	Gray [19]
Titanium	Ti-6Al-4V	2.8	Gray [19]
Aluminium	2024-T3	2.3	Gray [19], Gallagher [18]

theoretical retardation factor can be found by solving the equality in Eq. (2.21) for w.

$$\Delta K_{\mathrm{th}} = (\phi|_{a=a_{\mathrm{OL}}})^{\frac{1}{m}} \Delta K = \left(\frac{r_{\mathrm{p}}}{r_{\mathrm{p,OL}}}\right)^{\frac{w}{m}} \cdot \Delta K \tag{2.21}$$

Solving for w yields Eq. (2.22) [19, 20]. However, this relation is found by assuming a constant α. Implications of this assumption on accuracy have not been considered in literature so far. One could avoid the assumption by using $\sqrt{r_{\mathrm{p,OL}}/r_{\mathrm{p}}}$ at shut-off instead of R_{SO}. This suggestion is explored in Chapter 4.

$$w = \frac{m}{2}\left(\log\frac{\Delta K_{\mathrm{th}}}{\Delta K} \Big/ \log\frac{1}{R_{\mathrm{SO}}}\right) \tag{2.22}$$

The advantage of the theoretical approach is the limited experimental work as the input can be extracted from relatively simple experiments. It is clear that the shaping exponent is no longer constant but a function of material properties and loading. This can explain some of the dependencies observed for the experimental approach.

Although simulations using the indirect form of the Wheeler model (using ΔK_{eff}) cannot be found in literature, its use is recommended here. Accuracy in near-threshold regime, namely predicting crack arrest, is possibly improved because the discontinuity in the Paris law for $\Delta K = \Delta K_{\mathrm{th}}$ will be accounted for. This is illustrated by the following example. Consider the case where ΔK is slightly above ΔK_{th}, implementations used in literature will predict a crack growth rate $^{da}/_{dN} \neq 0$, even after correction with the retardation factor as $\phi \neq 0$. While the correction of Gray & Gallagher accounts for proximity to crack arrest, crack arrest itself will never be predicted. On the other hand, when the indirect form is employed, the calculated ΔK_{eff} will possibly be lower than ΔK_{th} and the crack propagation curve will correctly predict crack arrest.

2.4.3.3. Other modifications

Accounting for overloads and proximity to crack arrest does not cover all possible load interaction effects. One of the attempts to improve the Wheeler model further was made by Huang et al. [23], who addressed the effect of an underload that immediately follows an overload. An underload reverses the plastic flow and depletes the resulting plastic zone. To account for this, $r_{\mathrm{p,OL}}$ is decreased by the size of the reversed plastic zone. A fitted shaping exponent $w = 0.5$ is found for 350WT steel [23]. This is not

further elaborated as overload-underload effects are assumed negligible for the loading type considered in this dissertation.

Another influential contribution was made by Yuen and Taheri [22]. Additional factors ϕ_{D} and ϕ_{I} were introduced to account for delay retardation and overload interaction respectively. However, the experimental nature of these additional factors stands in contrast to the objectives of this dissertation [22]. Therefore, they will not be investigated.

The effect of block overloads instead of single overloads on the accuracy of the Wheeler model has been investigated experimentally in literature [21], but no model corrections were proposed.

2.4.4. Willenborg models

The approach of Willenborg models is different from that of Wheeler models in that the input for the crack growth law, ΔK and R, is modified. The reduced crack growth rate is thus obtained indirectly. The net cumulative growth is given by Eq. (2.23).

$$a_n = a_0 + \sum_{i=1}^{n} f(\Delta K_{\mathrm{eff},i}, R_{\mathrm{eff},i}) \tag{2.23}$$

Since the Willenborg model calculates a different effective load ratio R_{eff} for each retarded cycle, one or more Paris curves for the applied load ratio(s) are no longer sufficient, and a crack growth law that is a continuous function of load ratio is required. Literature recommends the use of the Forman equation or the Walker equation, although the Paris equation can also possibly be adopted if a quantification of the load ratio effect is lacking or if the load ratio effect can be neglected [16, 17].

2.4.4.1. Stress intensity factor reduction

Willenborg [16] assumed that retardation occurs because the stresses caused by the current load cycle are reduced due to residual compressive stresses within the overload plastic zone. The stress reduction was redefined in terms of a stress intensity factor reduction K_{red}, given in Eq. (2.24) [17]. Whereas Wheeler models define a ratio, Willenborg models quantify K_{red} through subtraction, without the use of an experimental parameter. The resulting equation is very straightforward.

$$K_{\mathrm{red}} = K^*_{\mathrm{max}} - K_{\mathrm{max}} \tag{2.24}$$

The idea is that both K_{max} and K_{min} are reduced by K_{red} to their effective non-negative values, given by Eqs. (2.25) and (2.26). Afterwards, ΔK_{eff} and R_{eff} can be calculated, given respectively by Eqs. (2.27) and (2.28).

$$K_{\mathrm{max,eff}} = \max(K_{\mathrm{max}} - K_{\mathrm{red}}, 0) \tag{2.25}$$

$$K_{\mathrm{min,eff}} = \max(K_{\mathrm{min}} - K_{\mathrm{red}}, 0) \tag{2.26}$$

$$\Delta K_{\text{eff}} = K_{\text{max,eff}} - K_{\text{min,eff}} = \begin{cases} K_{\text{max}} - K_{\text{red}}, & \text{for } K_{\text{min}} \leq K_{\text{red}} < K_{\text{max}} \\ \Delta K, & \text{for } K_{\text{red}} < K_{\text{min}} \end{cases} \tag{2.27}$$

$$R_{\text{eff}} = \frac{K_{\text{min,eff}}}{K_{\text{max,eff}}} = \begin{cases} 0, & \text{for } K_{\text{min}} \leq K_{\text{red}} < K_{\text{max}} \\ \dfrac{K_{\text{min}} - K_{\text{red}}}{K_{\text{max}} - K_{\text{red}}}, & \text{for } K_{\text{red}} < K_{\text{min}} \end{cases} \tag{2.28}$$

We can observe from Eqs. (2.27) and (2.28) that for small overload ratios ($K_{\text{red}} < K_{\text{min}}$), only R is adjusted to R_{eff}. For higher overloads, ΔK is adjusted as well. The lower R_{eff} (and possibly ΔK_{eff}), the lower the net crack growth rate will be. For $K_{\text{red}} > K_{\text{max}}$, the residual stresses in the overload plastic zone become so high that crack arrest occurs.

2.4.4.2. Crack arrest correction – generalized Willenborg model

A deeper study of Eqs. (2.24)–(2.28) shows that crack arrest ($K_{\text{max}} = K_{\text{red}}$) is predicted for $R_{\text{OL}} = 2$ at all times. However, literature indicates that crack arrest happens at a characteristic overload value $R_{\text{SO}} \neq 2$, as discussed in Section 2.4.3.2 and Table 2.2. Since this can lead to non-conservative predictions, a correction was developed. A reasoning similar to Wheeler's crack arrest correction was followed: at crack arrest the effective crack driving force cannot exceed the threshold of the material. Since the Willenborg model does not contain any empirical parameter, a correction factor λ for K_{red} is introduced and solved for [18]. The result is given in Eq. (2.29). When this correction is applied, the model is often called the generalized Willenborg model.

$$\begin{aligned} \Delta K_{\text{th}} &= \Delta K_{\text{eff}}|_{a=a_{\text{OL}}} \\ &= K_{\text{max}} - \lambda\, K_{\text{red}}|_{a=a_{\text{OL}}} \\ &= K_{\text{max}} - \lambda \left(K^*_{\text{max}}|_{a=a_{\text{OL}}} - K_{\text{max}} \right) \\ &= K_{\text{max}} - \lambda \left(K_{\text{max,OL}} - K_{\text{max}} \right) \\ \lambda &= \frac{1 - \dfrac{\Delta K_{\text{th}}}{K_{\text{max}}}}{R_{\text{SO}} - 1} \end{aligned} \tag{2.29}$$

2.4.4.3. Other modifications

Other improvements proposed in literature mainly focus on dealing with an underload that is applied immediately after an overload. The modified generalized Willenborg model introduces a dependency of λ on the underload ratio $R_{\text{UL}} = {}^{K_{\text{max,UL}}}/_{K_{\text{max,OL}}}$. The Walker-Chang-Willenborg model is another possibility [15]. In general, little research on improving the Willenborg model can be found in recent literature.

2.5. Crack closure models

Crack closure models consider the crack closure mechanism to be the controlling factor in load interaction effects under variable amplitude loading. This concept is introduced in 2.5.1. Afterwards, the two main approaches for quantifying crack closure are described.

2.5.1. Crack closure concept

The concept of crack closure was first introduced by Elber [34] after discovering that the fracture surfaces of a fatigue crack could be in contact even though a tensile loading was applied, sometimes even above the minimum cycle load. He attributed this phenomenon to a plastically deformed zone of compressive residual stresses left in the wake of a growing crack. Nowadays, this mechanism is called *plasticity-induced crack closure*, as there exist several other mechanisms responsible for crack closure, such as *roughness-induced crack closure* and *oxide-induced crack closure*. The existence of plasticity-induced crack closure under plane strain and the latter mechanisms are subject of some intense discussions [35].

Elber postulated that a crack could not grow when both crack surfaces are in contact. This led him to believe that the crack will only open, and thus grow, when the compressive contact stresses between both surfaces disappear. This can happen at a load level above the minimum cycle load. Therefore, he introduced the opening stress intensity factor $K_{\text{op}} > 0$, the K-value at which the crack is fully opened during loading. ΔK_{eff} can then be calculated by using K_{op} rather than K_{min}, as shown in Eq. (2.30). The larger K_{op}, the smaller ΔK_{eff} would be, leading to a decreased net crack growth. K_{op} is dependent on the material and previous load history [15].

$$\frac{da}{dN} = C(K_{\text{max}} - K_{\text{op}})^m = C(\Delta K_{\text{eff}})^m \tag{2.30}$$

Since $\Delta K = (1-R)K_{\text{max}}$ and crack arrest happens for ${}^{da}/_{dN} = 0$ and $\Delta K \leq \Delta K_{\text{th}}$, Eq. (2.30) implies that $\Delta K_{\text{th}} = (1-R)K_{\text{op}}$ when it is assumed that closure is the only crack arrest mechanism. Furthermore, ΔK_{eff} is dependent on the stress ratio R. Later, it was found that crack closure was also dependent on the ratio between maximum stress σ_{max} and the material flow strength σ_{fl}, and on the plastic zone size factor α. Therefore, the crack opening function $f(\frac{\sigma_{\text{max}}}{\sigma_{\text{fl}}}, \alpha)$ was introduced in Eq. (2.31). If f is defined like this, crack closure models are only able to explain the load ratio effect in constant amplitude loading [36]. However, several models have been developed to include load interaction effects in the value of f [14,15]. Sometimes, U is introduced as the effective SIF closure parameter [37]. The most rudimentary approach is to obtain the variation of U experimentally [38]. The applicability of this approach is however limited. More advanced models are discussed next.

$$\Delta K_{\text{eff}} = (1-f)K_{\text{max}} = \frac{1-f}{1-R}\Delta K = U\Delta K \tag{2.31}$$

2.5.2. Semi-empirical models

Semi-empirical models have in common that they determine the crack opening stress intensity factor K_{op} analytically for every cycle. Some of the most well-known models are ONERA, PREFFAS and CORPUS. The ONERA model determines K_{op} by taking a barycentric combination of two empirical functions that were obtained for the extreme cases of constant amplitude loading and a single overload. The PREFFAS model considers the K_{op} caused by previous cycles on the current cycle and takes the largest value. It is not adequate in cases of significant Δa, such as for higher crack growth rates and for long, periodically applied overload blocks, since effects of crack advance are neglected. The CORPUS model aims at covering periodic overloads and directly considers plastic deformation in the crack wake, which is in line with the plasticity-induced crack closure point of view. However, some assumptions on the shape of the crack wake are adopted. An overload generates a hump in the crack wake. This hump can be flattened by subsequent lower loads. Generally, ONERA and CORPUS models give better results. However, all semi-empirical models have one major disadvantage: they have to be tuned for specific load histories and are as such constrained models. Additionally, a large amount of experimental work is required [14, 15]. This concise description of semi-empirical models was given for the sake of completeness, as it is clear that they are not adequate for the goals of this dissertation.

2.5.3. Strip yield crack closure models

In contrast to semi-empirical models, the strip yield model determines the opening SIF by means of numerical simulations using a strip yield modelling technique that is modified to account for crack closure. The strip of fictitious crack length a_{fict}, consisting of the plastic zone in front of the crack tip and the plastic wake along the crack, is discretized into bar elements for numerical purposes. This is illustrated by Figure 2.12. The plastic zone ahead of the crack tip is modelled as an infinitely thin strip, similar to the approach used for estimating the plastic zone size in Section 2.4.1. To make the fictitious crack opening displacement for $a \leq x \leq a_{\text{fict}}$ equal to the plastic deformation of the strip material, a compressive yield stress is applied. Within this zone, bar elements are intact and able to carry both tensile and compressive stresses. In the crack wake, elements are broken and only compressive stresses can be carried when both crack surfaces are in contact. Outside of the strip, perfectly elastic material is assumed. In case of a growing crack, the strip material is disconnected over a distance corresponding to the crack growth increment. Consequently, a strip of plastically deformed material is building up in the crack wake. Stresses and lengths of the strip elements are computed for the maximum and minimum load of each fatigue cycle. For the displacement between the plastic strip and the surrounding elastic material to be compatible, it is also required to apply stresses on segments in the crack wake $x < a$ where the plastic elongation of the strip exceeds the fictitious crack opening displacement. These so-called contact stresses ensure displacement compatibility. The computation of K_{op} is then based on the distribution of the local plastic stretches behind the crack tip [14, 15].

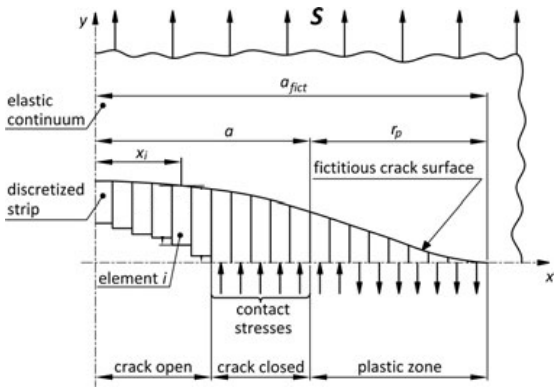

Figure 2.12.: Schematic of the strip yield model for crack closure [15]

Over the years, several implementations of the strip yield model emerged. Two of the most well-known models were developed by Newman and de Koning. The main difference lies in the definition of the constraint factor, similar to the concepts introduced in Section 2.4.1. Newman assumed a constant constraint factor dependent on the load level. De Koning, on the other hand, defined the constraint factor as a parabolic function along the considered elements and assumed plane stress at the end of the plastic zone [14].

2.6. Conclusions

This chapter's main ambition was to provide an exhaustive overview of existing variable amplitude fatigue crack propagation models available in literature. More attention was paid to models which aligned more with the requirements that were set in the introduction. Two main categories were selected for a deeper review.

The plastic zone models, the first category of interaction models that were discussed in detail, are all based on the same load interaction concept. The important role of the plastic zone size α was observed and it was reasoned that a correct estimation of α might be crucial to obtaining accurate results. Therefore, special attention was paid to approaches for estimating α more accurately by taking into account geometry and loading conditions. The assumption of a constant α, which is often found even in recent literature, was questioned and its implications on the model equations were identified. After a foundation was established, existing plastic zone models were presented and three common characteristics can be observed. First of all, less crack propagation will be predicted compared to the non-interaction model since only retardation of crack growth is simulated. Consequently, these models could potentially yield satisfactory results for overload-dominated load histories such as the case considered in this dissertation. The second common characteristic (except for the original Wheeler model) is the theoretical foundation. This makes them perfectly suited for applications in which a limited amount of experimental work and general applicability is required. In this regard, Willenborg may be disadvantageous since the effect of load ratio on crack growth rate has to be quantified, which requires additional experimental work. The third common characteristic is the short computing times since only simple calculations have to be performed. It has to be noted that the original Wheeler model is more of a relative approach since satisfactory prediction accuracy can only be obtained when the considered load history is similar to the one used to determine the shaping exponent.

The second category of discussed models were the crack closure models. The low applicability and extensive experimental characterization make them suitable only for niche applications. Strip yield models, on the other hand, are not constrained and are applicable to a variety of load histories, therefore being a versatile and robust crack growth prediction concepts. However, they have a major disadvantage in terms of computing time, as the solution for the crack surface displacements has a high computational cost. The potentially higher versatility and robustness of strip yield crack closure models does not compensate for the requirement of high computational capacity and running times. Their performance will not be examined further.

It is concluded that the plastic zone models offer the most potential to fulfil the aims of this dissertation as they fulfil all requirements. Their limited experimental work needed and fast calculation times are perfectly suited for this application. Their capabilities will be examined further in Chapter 4

3. XFEM-based stress intensity factor calculation

Load history, as presented in the previous chapter, was introduced as a chronologically ordered representation of all loading cycles that were applied to the structure or specimen in question. It was assumed that $K_{\max}$ and $K_{\min}$ are known (either directly or indirectly via ΔK and R). However, in real-life a certain K-value cannot be directly applied. Instead, only the load history in terms of a load P (expressed in units of force) is usually known. K is then calculated from the stress field near the crack tip, as a way of representing it as a singular value to work with. Transfer functions from P to K have been proposed in standards for various standardized specimen geometries [39]. An example of such a formula can be found in Chapter 5. However, one of the main goals of this work is to explore the possibility for developing a model capable of predicting fatigue crack propagation for arbitrary geometries. For this, numerical analysis is necessary. At present the finite element method (FEM) is most widely utilized due to its versatility and maturity of the theoretical basis. For a stationary crack, this approach is a preferred choice. However, some serious drawbacks manifest when the crack is allowed to propagate. To avoid some of these drawbacks, the Extended Finite Element Method (XFEM) was developed [40]. This is briefly explained in the second section. For a more thorough insight on XFEM, the reader is referred to the extensive work of Pommier et al. [41].

3.1. Finite element modelling of stationary crack problems

Finite element modelling of a stationary crack is straightforward. Just as for a regular structural analysis, the mesh must conform to the boundaries of the specimen. The crack, although infinitely sharp, is considered as such a boundary. Singularity problems near the crack tip are reduced by refining the mesh locally. Element size is decreased the closer the element is to the crack. Theoretical singularities can be attained by collapsing nodes at the crack tip [40].

Simulating a propagating crack introduces a whole new level of difficulty. One conventional implementation is the use of nodal relaxation or nodal release. For this, the whole region in which the crack is expected to propagate is refined. As the crack propagates, nodes are released and elements become disconnected. This is shown in Figure 3.13. When the crack tip moves from node 9 to node 4 new crack faces must be created in between. Therefore, node 9 is replaced by separate nodes 10 and 11. Another interpretation is that nodes 10 and 11 are initially glued together and this

glue is then 'released'. Besides the fact that the propagating crack must conform to the defined mesh (in terms of length and direction), an additional disadvantage is the huge computational cost involved. By refining a whole region, the number of elements and the associated degrees of freedom substantially increase. At every iteration, a large portion of the region is unnecessarily refined since the crack tip is only at one specific (but changing) location [40].

Another popular technique is remeshing. For every crack increment a new local mesh refinement is calculated around the new crack tip. The propagating crack does no longer have to conform to a predefined mesh since it is renewed every iteration. Therefore, remeshing is the only option in case the crack path is not known in advance. Although the degrees of freedom significantly drop, the computational cost of calculating a new mesh every iteration cannot be underestimated either [40].

Modern uses of FEM often combine remeshing and nodal relaxation to obtain a minimal computational cost for a propagating crack with an unknown trajectory. Over time, several tools were added to improve results and lower computational time further. Additionally, different crack growth criteria, either based on stress or energy, were developed [40]. These are of no interest to this work as only an accurate description of the stress field is needed.

3.2. Extended finite element method

In conventional FEM, the infinitely sharp crack is considered part of the geometry. Immensely small element sizes are required to accurately obtain the higher stress gradients around this singularity. Another way of tackling this problem is to consider the crack as a discontinuity within the material and not as a geometric feature. The problem is that FEM requires continuous material properties due to its use of continuous shape functions or interpolation functions. This is where Extended Finite Element Method (XFEM) comes into play. It allows the shape functions to be discontinuous inside an element. For example, the crack tip singularity is addressed by introducing a modified or enriched finite element which accounts for the crack tip singularity in its internal definition. Another enriched element, the cut-through element, is defined for elements through which the crack has fully propagated. It are in fact the nodes of these elements that are enriched. The advantage of this approach is that the mesh does no longer have to conform to the crack, as the elements themselves account for its presence [40, 41]. In fact it is the other way around: by enriching the nodes of an existing mesh, a crack can be introduced (and propagated) without remeshing [42]. In Figure 3.14 enriched nodes have been marked for an edge crack in a uniform mesh and a middle crack in a non-uniform mesh. The distinction between the different types of enriched nodes will be explained further.

The concept of the enriched nodes is based on the conventional FEM displacement function, given by the first term in Eq. (3.1), where N_i and u_i are respectively the conventional shape functions and the conventional degrees of freedom (DOF). Γ is the collection of all nodes in the finite element model [42].

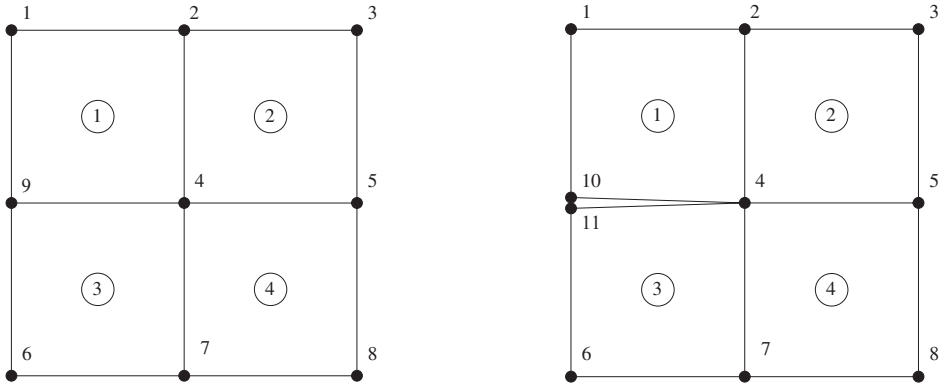

(a) No separation (b) Separation

Figure 3.13.: Node relaxation (adapted from [41])

$$u = \sum_{i \in \Gamma} N_i(x) \cdot u_i + \sum_{i \in \Gamma_c} N_i(x) \cdot H(x) a_i + \sum_{i \in \Gamma_t} N_i(x) \cdot \sum_{\alpha=1}^{4} F_\alpha(x) b_i^\alpha \tag{3.1}$$

A first type of enrichment is done by the discontinuous enrichment functions located around the crack, denoted as the subset Γ_c and indicated in blue in Figure 3.14. These functions allow the element to open the crack faces [42, 43]. Such a discontinuous element is modelled as the superposition of two continuous elements with phantom nodes. This is illustrated in Figure 3.15. The crack $C-D$ is assumed to follow a straight line through each element until it hits the boundary. The effect of the discontinuity is localized by enforcing continuity at the non-enriched nodes A and B. Then all non-cracked elements can be standard elements [44]. The additional DOF introduced by the phantom nodes are represented by a_i. The sign function $H(x)$ takes a value of $+1$ or -1 depending on which side of the discontinuity the node is located [42].

A second type of enrichment is done for nodes surrounding the crack tip. In linear elastic materials, the asymptotic solutions $u_i(r, \theta)$ for the crack tip singularity are known. These displacements, the so-called crack tip enrichment functions, are added to the conventional displacement field for all nodes around the crack tip. These nodes are denoted as the subset Γ_t and indicated in red in Figure 3.14. F_α and b_i^α are the crack tip functions and the corresponding enriched DOF [42, 43].

The advantages of XFEM are abundantly clear from the previous discussion. In Abaqus, the finite element software that is used to apply XFEM, the implementation of XFEM is not perfect and some limitations still exist, for example the fact that an enriched element cannot be intersected by more than one crack. These limitations do not have any consequences for the problem that is considered in this dissertation [40].

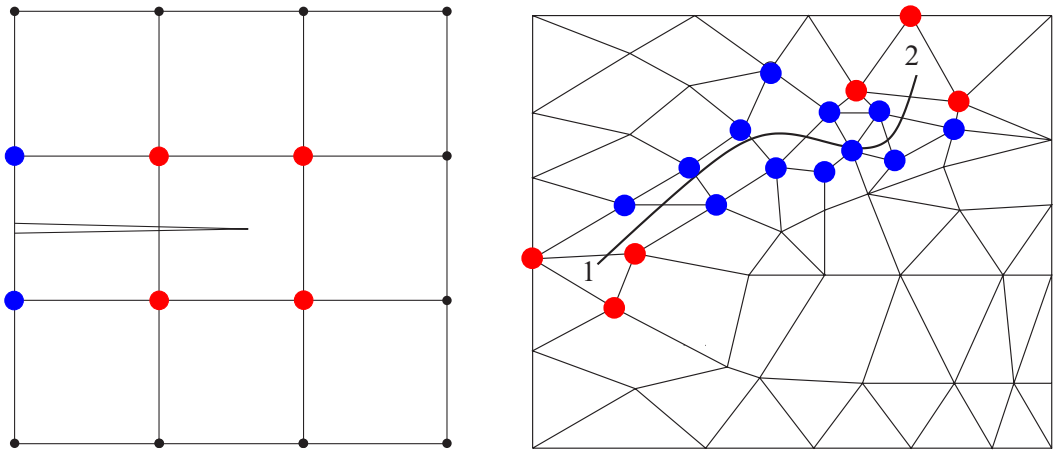

(a) uniform mesh (b) non-uniform mesh

Figure 3.14.: Enriched nodes of an XFEM mesh (adapted from [41])

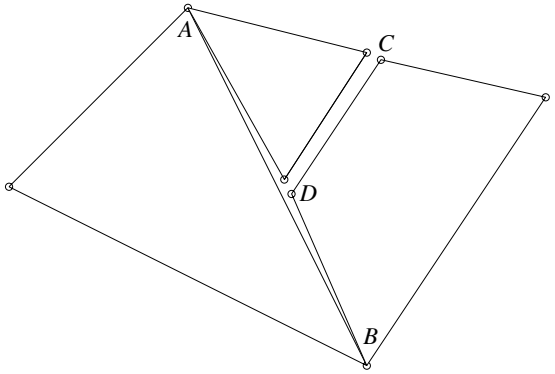

Figure 3.15.: Discontinuous element with phantom nodes [44]

3.3. Stress intensity factor evaluation

Once the stress field solution is known, the stress intensity factors are calculated along the crack front at every point where the crack front intersects an element boundary. At every evaluation point, K calculated using a contour integral, which is basically a volume integral that is evaluated along a contour and whose value is independent of the chosen path [7,41]. The contour domain for the volume integral is constructed from rings of elements around the crack tip element [45]. This is shown in Figure 3.16.

At each evaluation point a contour integral calculation is performed for all specified element rings. Because finite element solutions are approximate, the value of the integral is not completely independent of the chosen path, but is instead expected to converge as the ring domain increases. Therefore, the first few contours are usually discarded [45].

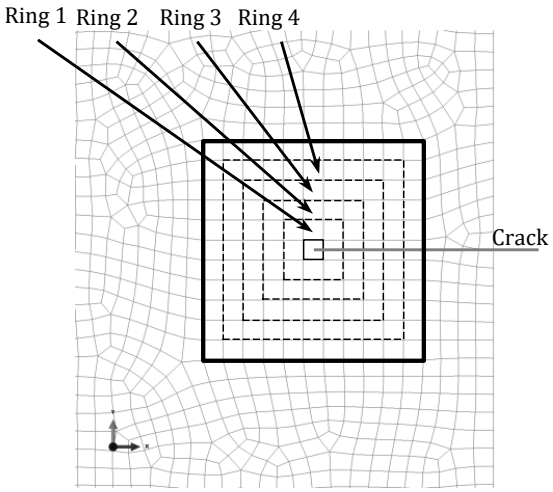

Figure 3.16.: Contour domain for evaluation of K [45]

3.4. Conclusion

In this chapter, the possibilities of calculating stress intensity factors for a propagating crack in arbitrary geometries were explored. The conventional FEM approach was introduced and its limitations were identified. In order to avoid some of these limitations, the Extended Finite Element Method was studied. Based on the key requirement of low computational cost, it can be concluded that XFEM suits the needs of the problem at hand. Performance of this technique will be analysed in Chapter 5.

Part II.

CASE STUDY – THE ESET SPECIMEN

4. Comparison of fatigue crack propagation simulations

In this chapter the potential of plastic zone models (presented in Chapter 2) to describe experimentally obtained crack propagation curves is examined. The presented crack growth curves are calculated using the algorithm that will be presented in Chapter 6. All input for these curves, if not accompanied by a reference, is based on the experimental work of De Tender [2, 5]. As mentioned before, De Tender performed two different types of block load fatigue tests that are of particular interest to this dissertation. These sequences were applied to eccentrically-loaded single edge crack tension (ESET) specimens of different materials. More details about these specimens will be provided in Section 4.3. As block loading was K-controlled, detailed knowledge of specimen geometry is not required since no stress intensity factors have to be calculated. It was introduced earlier that crack growth propagation models tend to overestimate crack growth. Therefore measured crack growth, which was obtained in between different loading blocks, will be used a lower bound reference to aim for. The non-interaction model will be used as an upper bound reference. All loading cycles were applied with $R = 0.1$ and also the Paris law was obtained at this load ratio.

Before the performance of these models can be accurately judged, it is necessary to gain an understanding about the different parameters involved, such as plastic zone size, experimental fitting parameters, shut-off overload ratio or fatigue threshold. Therefore, a sensitivity analysis is presented first.

Afterwards, two improved models, so called extended plastic zone models, starting from the plastic zone models presented in Chapter 2 are proposed. The improvement is based on accounting for variable plastic zone size. These models are then gauged against existing models in a performance analysis.

4.1. Sensitivity analysis

The virtual load history that is applied for all sensitivity analyses within this section is given in Figure 4.17. To make sure that the applied loads are in the same order of magnitude as in real-case scenarios, the load history used in this sensitivity analysis is based on the low-high-low sequence defined by De Tender and applied for material A (see Section 4.3). All fatigue cycles are applied with $R = 0.1$ and the Paris law for material A was used. The load history in Figure 4.17 consists of several parts. First, $\Delta K = 20\,\mathrm{MPa}\sqrt{\mathrm{m}}$ is applied during 5000 cycles in order to obtain a linear crack growth curve. Next, a single overload of $\Delta K = 30\,\mathrm{MPa}\sqrt{\mathrm{m}}$ is applied and an overload

plastic zone is established. Afterwards, the previous constant loading is resumed for 50000 cycles. The non-interaction model will give the same slope as before, while the interaction models should deviate due to retardation. At last, two lower block loads, $\Delta K = 15\,\mathrm{MPa}\sqrt{\mathrm{m}}$ and $10\,\mathrm{MPa}\sqrt{\mathrm{m}}$ respectively, are applied for 50000 cycles each. For these blocks, it is assumed that the overload plastic zone is induced by the last cycle of the previous higher block. This means that the length of the block have no influence of the amount of retardation that is calculated. It must be realized that this assumption may not be acceptable.

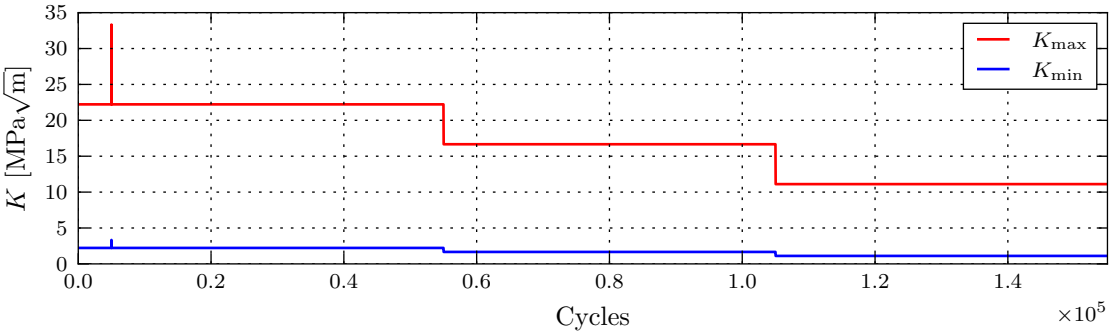

Figure 4.17.: Virtual load history used in sensitivity analysis

Wheeler models will be analysed first since they only need the aforementioned Paris law. Afterwards, this law will be extended using the Walker equation to account for load ratio, so that it can be used for an in-depth analysis of the Willenborg models.

4.1.1. Wheeler models

Evidently, an import parameter in all plastic zone models, thus also in all Wheeler models, is the plastic zone size, more specifically α. The second important parameter is the shaping factor w. This can be either a constant value, as employed in the original Wheeler model (Wh.), or a varying function of R_{SO} and ΔK_{th} based on the theoretical approach of the Modified Wheeler model (Mod. Wh.). This was explained in more detail in Section 2.4.3.

Influence of plastic zone size In Figure 4.18 the influence of α on the amount of retardation is investigated for the original Wheeler model. By comparing the solid and dashed lines, plane strain and plane stress[1] respectively, it is obvious that α has an enormous effect on the amount of retardation. This is fully in line with what one might expect: a higher α (less constrained crack tip) will result in a larger plastic zone. Consequently, the amount of retarded cycles increases. This effect is self-reinforcing since this larger plastic zone will give smaller ϕ-values and thus lower crack growth rates. It can be concluded that a correct estimation of plastic zone size is crucial to achieve accurate results.

[1] based on the LEFM approach

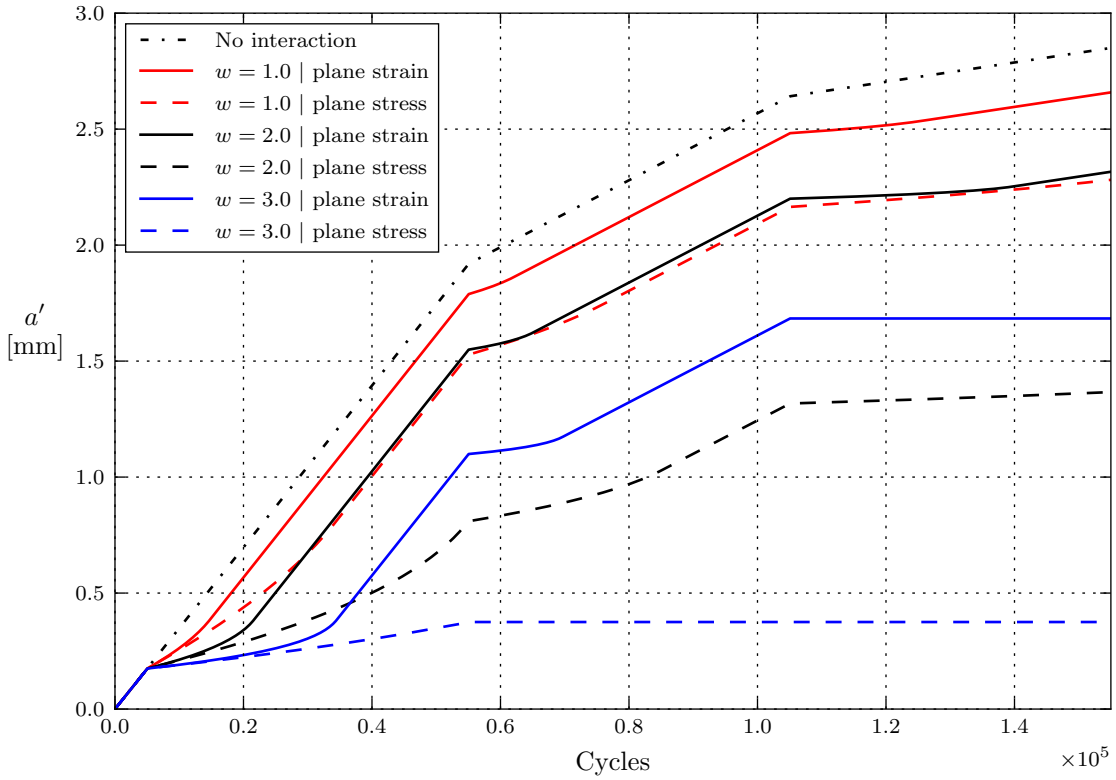

Figure 4.18.: Influence of plastic zone size factor α and shaping exponent w in the original Wheeler model

Influence of shaping exponent Another influence that is investigated in Figure 4.18 is the retardation factor. An intuitive value of $w = 2$ is compared to lower and higher values of 1 and 3, respectively. Again, the influence is found to be significant. The 'no interaction' line is equivalent to the Wheeler model for $w = 0$. The values that were taken for w are realistic, as will be clear from Figure 4.19 and the following paragraphs.

Figure 4.18 also shows that the influence of α and w are different. α, on the one hand, does not influence crack growth significantly at the beginning of retardation but will rather influence the duration of retardation. This is seen by comparing the blue curves for example. w, on the other hand, influences crack growth rate at all stages of retardation.

Influence of fatigue threshold A first influencing parameter of the Modified Wheeler model is ΔK_{th}. From Figure 4.19 it can be judged that w decreases for an increase in ΔK_{th}, so increasing the fatigue threshold will decrease the amount of retardation. This is counterintuitive at first, but actually very logical. If it is assumed that the fatigue threshold corresponds to the point where the crack growth rate goes below a certain value, then a higher ΔK_{th} means that crack growth rates in function of applied ΔK

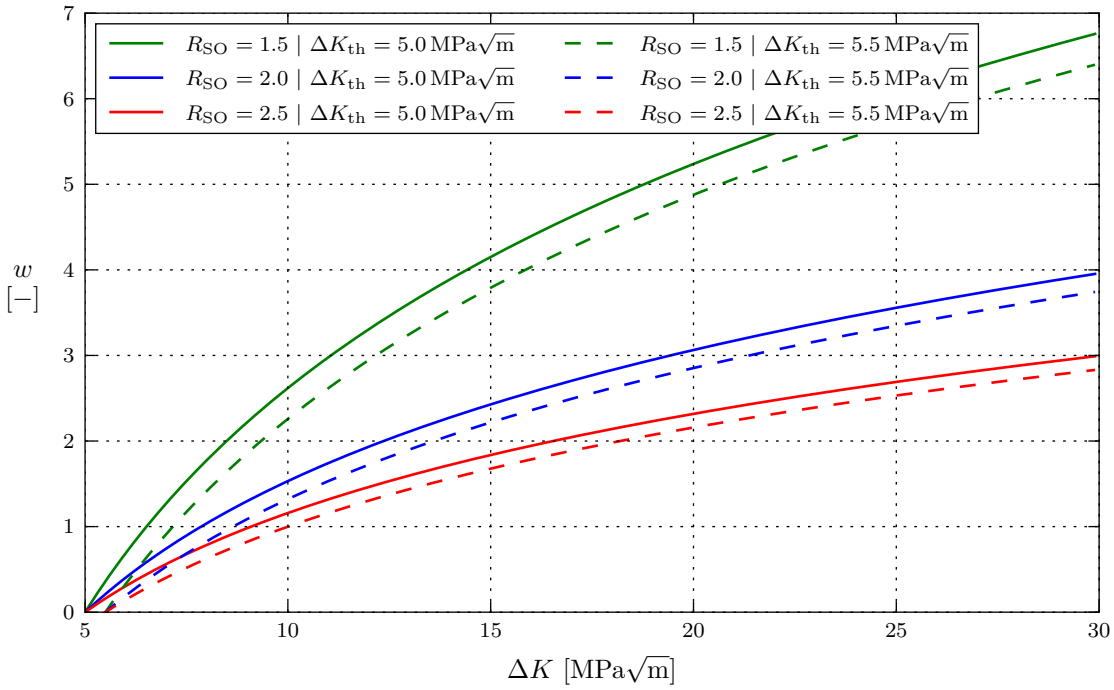

Figure 4.19.: Influence of shut-off overload ratio R_{SO} and fatigue threshold ΔK_{th} on the theoretical shaping exponent

are generally lower (see Figure 4.21 further in this section). These lower crack growth rates justify a lower retardation factor. Generally, ΔK_{th} does not vary significantly so its influence will be less pronounced [46].

Influence of shut-off overload ratio Figure 4.19 indicates a much more pronounced influence factor, namely R_{SO}. It is clear that w can vary significantly in function of ΔK, and that a constant value is too much of a simplification. The influence of R_{SO} on crack propagation predictions is shown in Figure 4.20. A non-linear dependence can be observed. A lower R_{SO} increases w and accordingly the amount of retardation, since overload ratios R_{OL} are relatively closer to shut-off. As R_{SO} approaches the overload ratio $R_{OL} = 1.5$ of the single overload, the correction for proximity to crack arrest becomes more and more pronounced. For $R_{SO} < 1.5$ crack arrest is indeed predicted after the first overload. For $R_{SO} = 1.6$ crack arrest is predicted after the first block overload because the plastic zone of the single overload is still active and $R_{OL} = 2 > 1.6$.

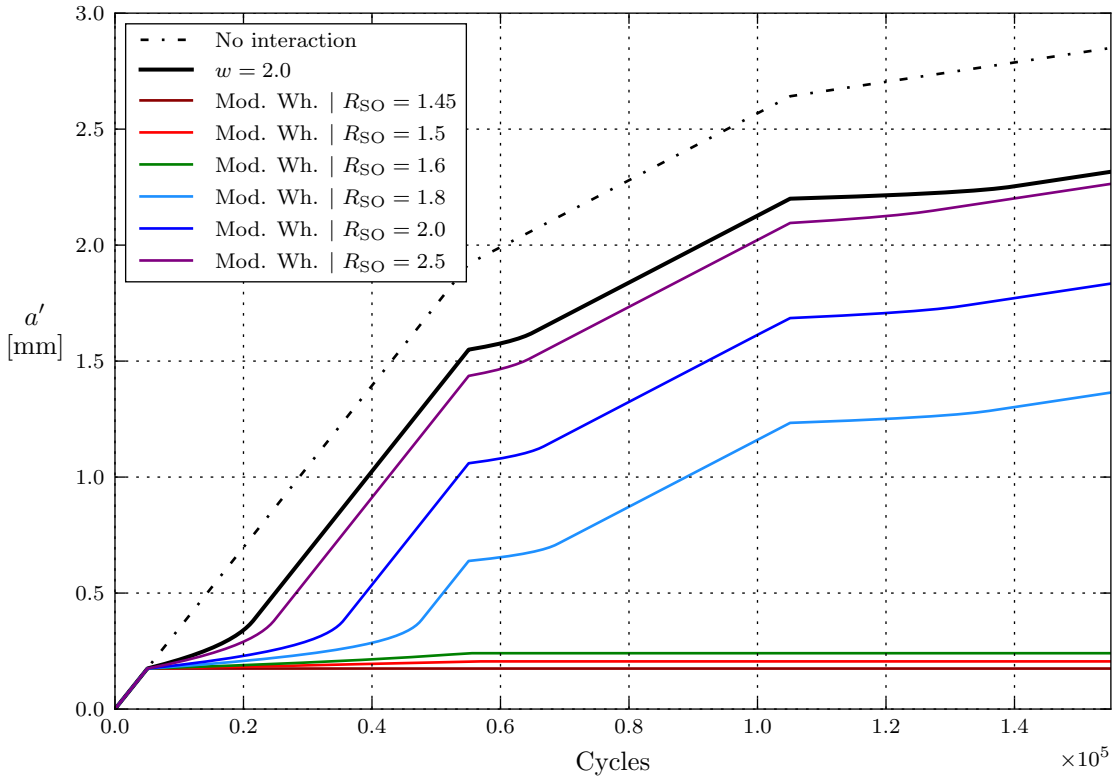

Figure 4.20.: Influence of shut-off overload ratio R_{SO} on the Wheeler models

4.1.2. Willenborg models

As discussed before, one of the impractical aspects of the Willenborg model is the use of an effective load ratio $R_{eff} < R$. In practical applications, often only the Paris law for a single value of R is known. If this is used for Willenborg predictions, only part of the potential retardation effect is accounted for. If this is the case, the Walker equation, Eq. (2.5), can be adopted to account for the influence of load ratio on crack growth rate. The unknowns C_0 and m_0 can be found by equating the Walker equation for the known load ratio to the available Paris law for the corresponding load ratio. The formula are given in Eqs. (4.2)–(4.1). $(1 - \gamma)$ represents the sensitivity to load ratio, with $\gamma = 1$ meaning no influence of R. For metals, typical γ-values range from 0.4 to 0.8, with main dependence on the ultimate tensile strength [11]. A graphical representation of the Walker equation is given in Figure 4.21. It is assumed here that the crack growth rate just above the fatigue threshold is independent of load ratio. It is given that $\Delta K_{th} = 5.0$ for $R = 0.1$. This value is shifted accordingly for all other load ratios. It has to be remarked that this discontinuity is not a fully accurate representation of reality, and that a smoother transition, such as in Figure 2.3, would be better suited. The effects of this are not considered here.

$$m_0 = m \tag{4.1}$$

$$C_0 = C \cdot (1 - 0.1)^{(1-\gamma)m_0} \tag{4.2}$$

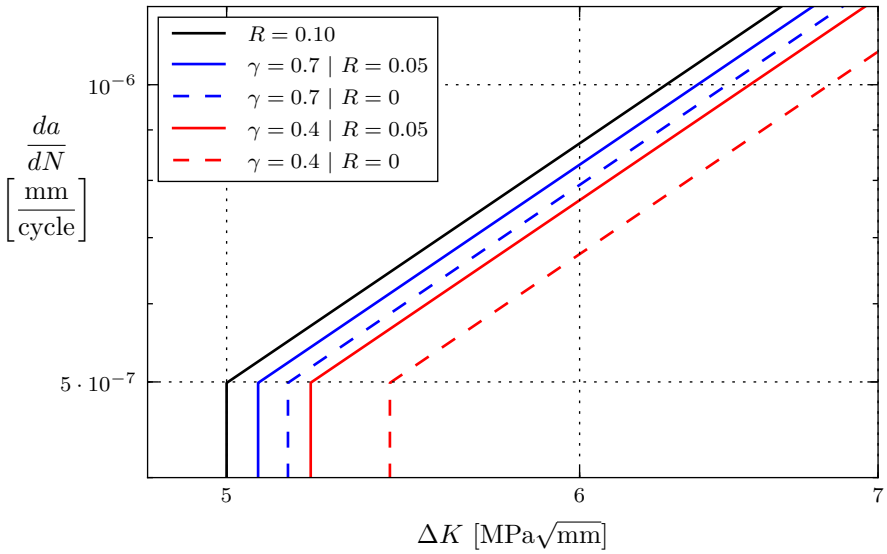

Figure 4.21.: Effect of load ratio R on crack growth rate according to the Walker equation for different Walker exponents γ

Influence of load ratio The improvement when accounting for both ΔK_{eff} and R_{eff} instead of only ΔK_{eff} can be observed in Figure 4.22. It is clear that an increase in retardation can be expected when sensitivity to the load ratio effect increases. Moreover, the effect is largest for plane stress and almost negligible for plane strain. This observation can be linked to the fact that in plane stress the reductions in K and R are much larger, thus the effect of γ is more pronounced.

Influence of plastic zone size The influence of α on the amount of retardation is investigated for the Willenborg models as well. From Figure 4.22 it is again clear that retardation significantly increases when plane stress is assumed. Again, a self-reinforcing effect is in play, since the larger plastic zone size will also result in a higher K_{red}. Crack arrest is not predicted for the original Willenborg model since all overload ratios are below 2.

Influence of fatigue threshold The influence of ΔK_{th} on the proportionality factor λ of the generalized Willenborg model is shown in Figure 4.23. Again, a counterintuitive influence is observed, since a higher fatigue threshold will decrease λ and the total

reduction in K. The reasoning is analogous to the one given for the modified Wheeler model. Also here the influence of ΔK_{th} seems to be insignificant to the overall λ-value.

Influence of shut-off overload ratio Next to ΔK_{th}, R_{SO} is another parameter for the determination of λ. In Figure 4.23, it is clear that for $R_{\text{SO}} = 2$, $\lambda < 1$ and K_{red} will be lower than for the original Willenborg model, although both models predict crack arrest for $R_{\text{SO}} = 2$. This discrepancy is explained by the fact that the original Willenborg model assumes $\Delta K_{\text{th}} = 0$, resulting in a step function at $\Delta K = 0$. In reality however, the fatigue threshold is higher, crack growth rates are lower and λ does not need to be as high. This decreased amount of retardation is also visible by comparing the black and blue lines in Figure 4.24.

A lower R_{SO} increases λ and accordingly the amount of retardation, since overload ratios R_{OL} are relatively closer to shut-off. For the single overload $R_{\text{OL}} = 1.5$ applies and crack arrest should be predicted for $R_{\text{SO}} < 1.5$, as is the case. For the red curve (corresponding to $R_{\text{SO}} = 1.5$) crack arrest is predicted after the first block overload because the plastic zone of the single overload is still active and $R_{\text{OL}} = 2$. In general, sensitivity to R_{SO} is found to be lower when compared to the modified Wheeler model.

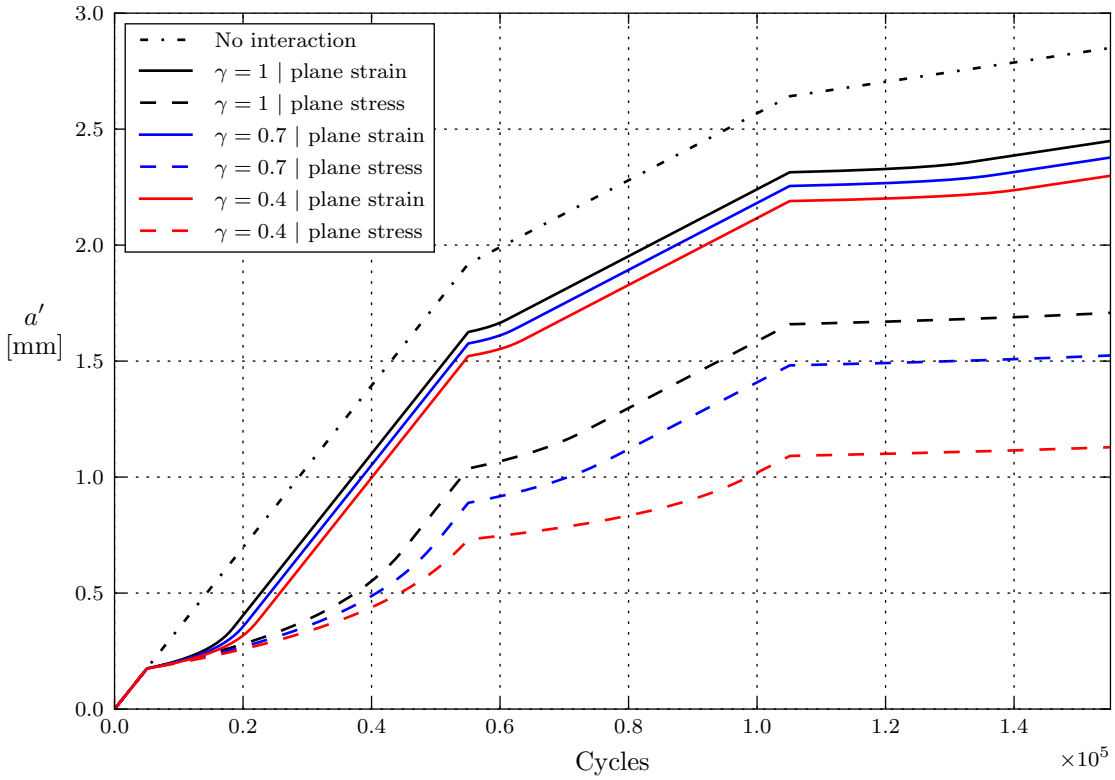

Figure 4.22.: Influence of plastic zone size factor α and Walker exponent γ on the original Willenborg model

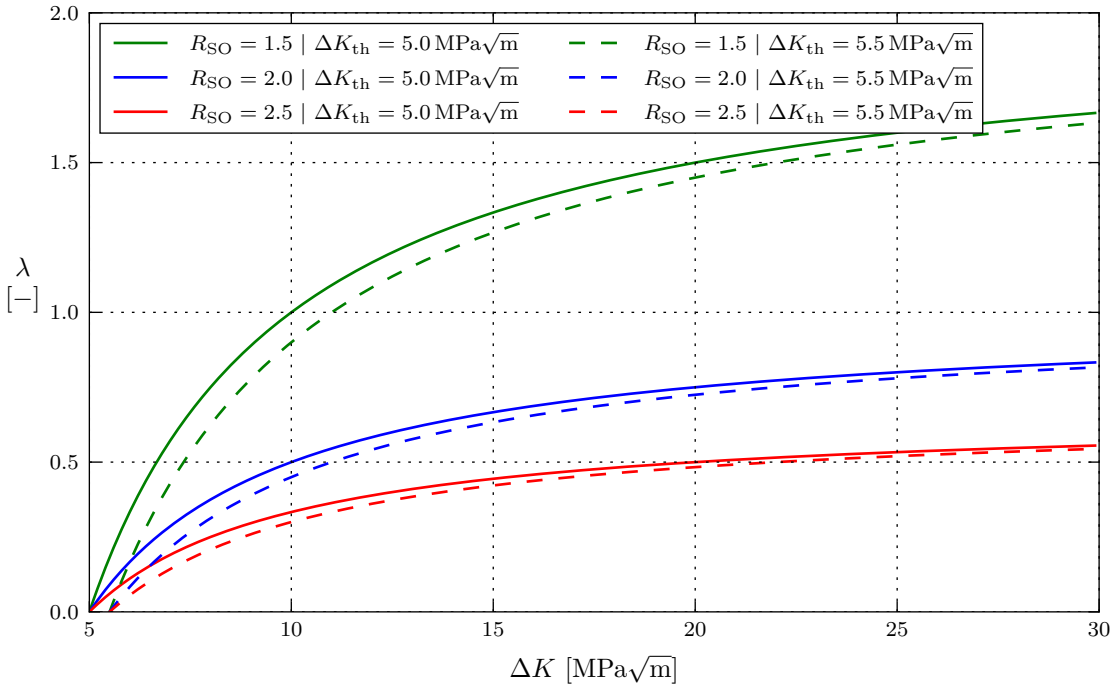

Figure 4.23.: Influence of shut-off overload ratio R_{SO} and fatigue threshold ΔK_{th} on the Willenborg correction factor λ

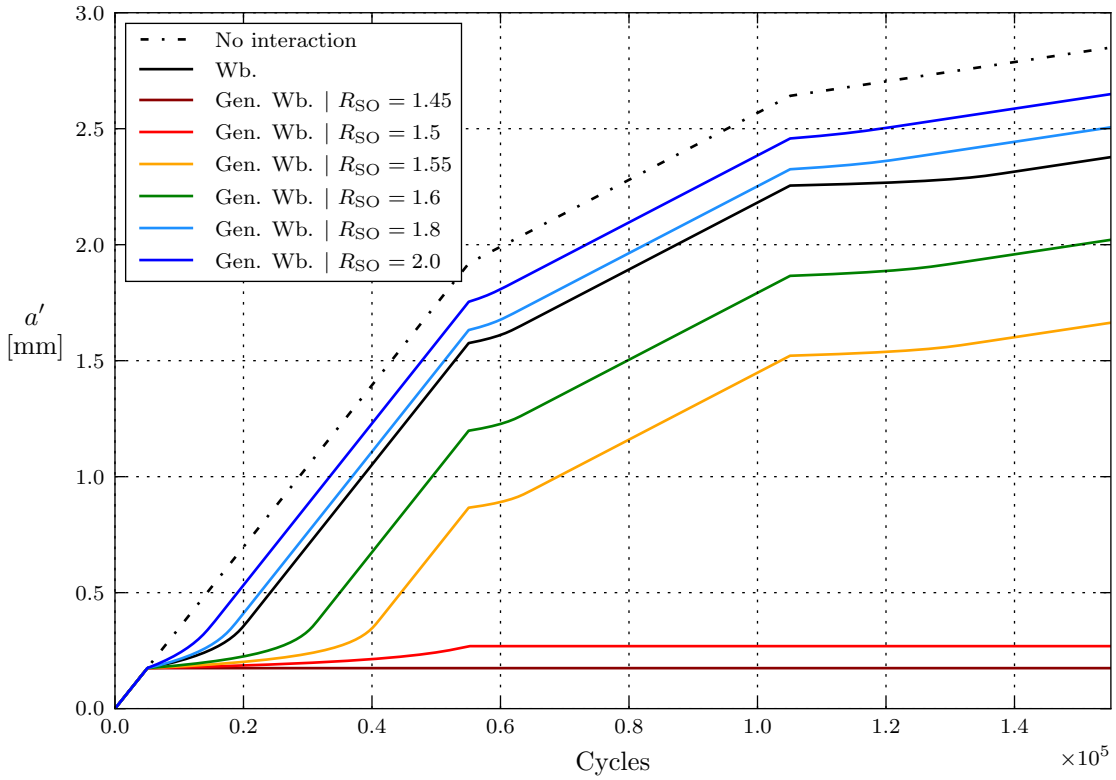

Figure 4.24.: Influence of shut-off overload ratio R_{SO} on the generalized Willenborg model

4.2. Extended plastic zone models

In the previous section, plastic zone size was identified as one of the main influence factors. Therefore, it is essential to estimate α correctly. In Chapter 2, different estimation approaches were compared in function of normalized thickness τ. The τ-range applicable for this case study can be found by transforming the applied $K_{\max}$-values (Figure 4.27 further in this chapter) to τ-values using Eq. (2.9) together with the appropriate specimen thickness and yield strength. The result for both specimens is given in Figure 4.25. Plane strain can be safely assumed according to the LEFM α-estimation. The SY approach however considers the τ-range to be in the transition zone, although at first sight a plane strain assumption does seem acceptable as well. The consequences of this choice will be examined in Section 4.3. Preference is given to the SY approach due to its continuity and the fact that it was confirmed by finite element analysis. $n = \infty$ will be assumed since differences to the curve for $n = 10$ are small and for conservatism.

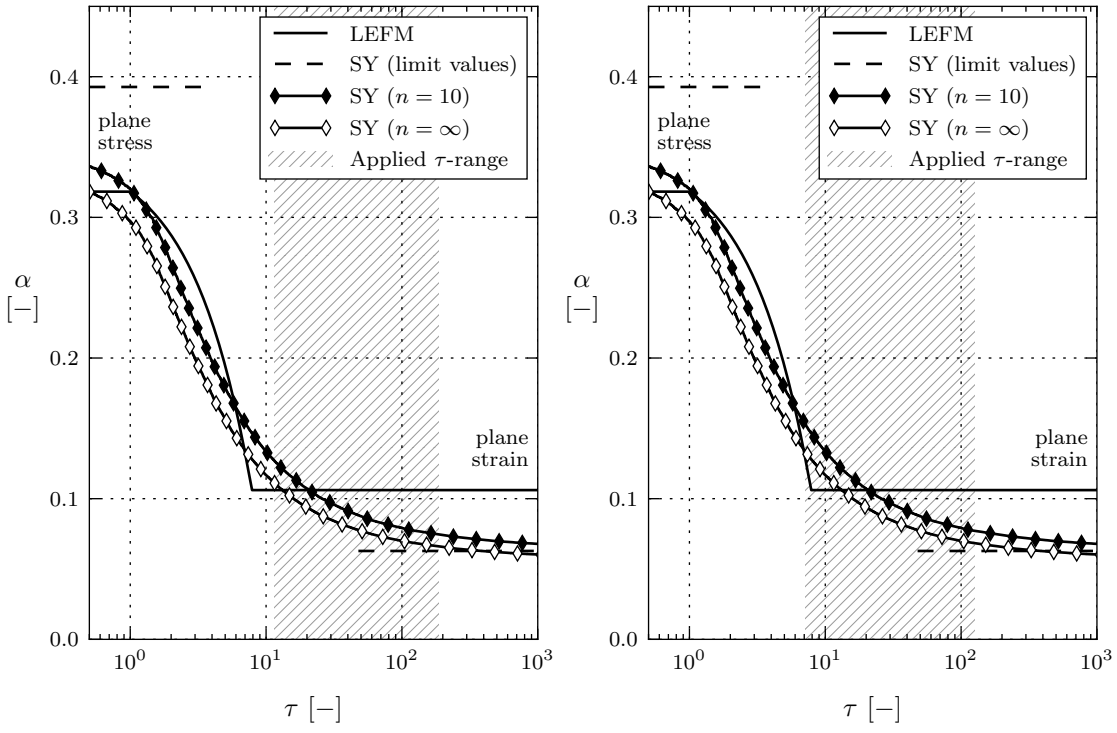

(a) specimen A (b) specimen B

Figure 4.25.: Applied range of normalized thickness τ

It is mentioned in Chapter 2 that the derivation for w (Wheeler model) and $K^*_{\max}$ assumes a constant plastic zone factor. However, if α is a function of $K_{\max}$, as is proposed here, these derivations become invalid. In this dissertation, an extension for both the modified Wheeler model and the generalized Willenborg model is proposed to

account for a varying plastic zone size. The resulting models are named the extended Wheeler model and extended Willenborg model respectively.

4.2.1. Extended Wheeler model

As stipulated in Chapter 2, Eq. (2.19) should be used instead of Eq. (2.18). This avoids a first constant α assumption. However, for the theoretical derivation of w, such an assumption was done again for R_{SO}. A more general formula for w is found by employing a corrected shut-off overload ratio R'_{SO} instead of R_{SO}. Their relation is expressed in Eq. (4.3).

$$R'_{\mathrm{SO}} = \sqrt{\frac{r_{\mathrm{p,OL}}}{r_{\mathrm{p}}}} = \sqrt{\frac{\alpha_{\mathrm{OL}} \cdot K^2_{\mathrm{max,OL}}}{\alpha \cdot K^2_{\mathrm{max}}}} = \sqrt{\frac{\alpha_{\mathrm{OL}}}{\alpha}} R_{\mathrm{SO}} = R_\alpha R_{\mathrm{SO}} \tag{4.3}$$

A correction factor R_α is introduced to account for a load-dependent α-value. Overload ratios are typically measured as a ratio of stress intensity factors (R_{OL}), so a transformation to R'_{OL} is needed for an accurate use of the extended Wheeler model. After an overload $R_\alpha > 1$ and $R'_{\mathrm{SO}} > R_{\mathrm{SO}}$. As a result, less retardation would be expected according to the sensitivity analysis. However, this effect is counteracted by the fact that the overload plastic zone size is larger, giving more retardation. The net result of both influences will be investigated in the performance analysis further in this chapter. In case a constant α-value is assumed, $R_\alpha = 1$ and the extended Wheeler model is fully equivalent to the modified Wheeler model.

4.2.2. Extended Willenborg model

For the Willenborg models, the assumption of a constant α occurs already at the definition of K^*_{max} (see Chapter 2), since its calculation is based on this very assumption. A more general form of the proportionality used is given in Eq. (4.5). Both members of the equation are multiplied by their respective α-factors which are not necessarily equal. This leads to the general formula for K^*_{max} given in Eq. (4.4). Since α^* is a function of K^*_{max}, Eq. (4.4) has to be iteratively solved. The proposed correction results in a higher K^*_{max}, K_{red} and consequently more retardation. Further derivations for the Willenborg model are done in terms of stress intensity factors instead of plastic zone sizes, so no additional corrections are required. This also means that λ is calculated using the regular R_{SO}-value. In case a constant α-value is assumed, the extended Willenborg model is fully equivalent to the generalized Willenborg model.

$$\alpha^* \frac{K^*_{\mathrm{max}}}{r^*_{\mathrm{p}}} = \alpha_{\mathrm{OL}} \frac{K_{\mathrm{max,OL}}}{r_{\mathrm{p,OL}}} \tag{4.4}$$

$$K^*_{\mathrm{max}} = K_{\mathrm{max,OL}} \sqrt{\frac{r^*_{\mathrm{p}}}{r_{\mathrm{p,OL}}}} \sqrt{\frac{\alpha_{\mathrm{OL}}}{\alpha^*}} \tag{4.5}$$

4.3. Performance analysis

4.3.1. Input data

In previous sections, insight into the effect of different parameters on the prediction of retardation was established and extended plastic zone models were proposed. The performance of all presented plastic zone models can now be analysed by comparing their predictions to experimentally obtained crack growth curves. The properties of the two ESET specimens used for these experiments are summarized in Table 4.1. Specimen geometry is visualized in Figure 4.26. The thickness t of the specimen is needed to estimate the plastic zone size, while the width W provides a means to express crack length as a dimensionless value a/W. Crack length was measured in between different loading blocks and will be used as a lower bound reference. As before, the non-interaction model is used as an upper bound reference. γ can be determined based on σ_u for both materials [11].

Table 4.1.: Specimen properties

	Material			Geometry		Fatigue			
	Type	σ_y [MPa]	σ_u [MPa]	W [mm]	t [mm]	C	m	ΔK_{th} [MPa$\sqrt{\text{m}}$]	γ [−]
A	NV F460	560	635	60.8	15.0	$3.6{\cdot}10^{-9}$	3.064	5.0	0.7
B	NV F500	630	680	40.8	10.0	$3.0{\cdot}10^{-9}$	3.268	5.0	0.7

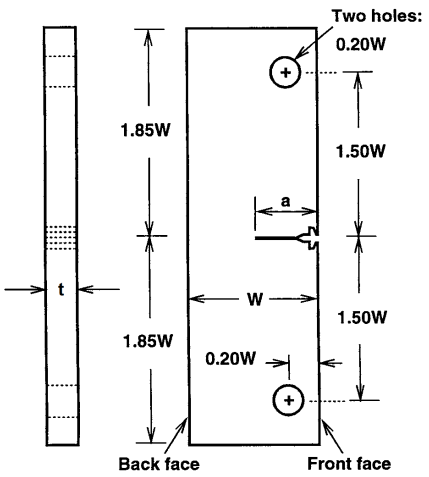

Figure 4.26.: Standard eccentrically-loaded single edge crack tension specimen [39]

Load history For each specimen, two different types of block load sequences were applied. The first type is a low-high-low (LHL) block sequence, as shown in Figures

4.27a and 4.27c. Up to and including the highest block, no retardation effects are expected and the predictions of the non-interaction model should correlate well to crack length measurements. The second loading is a semi-random (SR) block sequence. Block loads have been randomly ordered in order to better simulate real life loading conditions. Since it was made sure that crack arrest can only occur at the end, the ordering is not fully random and semi-random may be a better term. The SR block sequences for both specimens are given in Figures 4.27b and 4.27d.

Shut-off overload ratio Besides the load histories and the specimen properties given in Table 4.1, R_{SO}-values for both specimens are also required. Sensitivity to R_{SO} increases rapidly as it approaches the applied overload ratio R_{OL}. In order to get an idea of appropriate R_{SO}-values, the R_{OL}-values from all presented load histories can be plotted in function of $K_{\max}$. This is done in Figure 4.28. R'_{OL} is provided as well in order to be able to estimate R'_{SO}, which is required in case the extended Wheeler model is used.

Based on measured crack growth, two types of $(R_{\mathrm{OL}}, K_{\max})$-pairs are distinguished, namely those for which crack arrest occurs and those for which crack growth continues. Apparently, the assumption of a constant R_{SO}-value is an oversimplification. In reality, an upward trend can be noticed as the relation $R_{\mathrm{SO}} = f(K_{\max})$ must lie somewhere in between points of crack arrest points and those of crack propagation. In order to gauge whether a more accurate experimental characterization of this behaviour might be worthwhile in the future, an upper bound $f_{\geq}$ and lower bound $f_{\leq}$ are introduced in Figure 4.28a. A constant value is assumed for high $K_{\max}$. Additionally, it was reasoned that both bounds must go through a common point $(R_{\mathrm{OL}} = 1, K_{\max,\mathrm{th}})$ as crack arrest occurs below the fatigue limit even for constant amplitude loading. $K_{\max,\mathrm{th}} = \Delta K_{\mathrm{th}}$ is assumed. The discontinuous bounds are presumably unrepresentative of real-life behaviour. Therefore, $\bar{f}$ is introduced to smoothen the upper bound curve, especially in the near-threshold region. For this case study the R_{SO}-functions are only sampled at the $K_{\max}$-values for which R_{OL} was obtained. Since $\bar{f} = f_{\geq}$ at these points, either function can be chosen as an upper bound. In the following simulations, the consequences of choosing either $\bar{f}$ or $f_{\leq}$ will be examined. The difference between their respective predictions gives an idea of the potential improvement that a more detailed characterisation of R_{SO} can give. It should be noted that the lower bound does not have a kink at the fatigue threshold to make sure that the curve provides a true lower bound as we do not know the behaviour of R_{SO} in this region.

4.3.2. Low-high-low block load sequence

In Figure 4.29, measured crack growth for the LHL sequences of both specimens is compared to the non-interaction model predictions. In line with our expectations, good correlation is found for the first 5 block loads. For these blocks, all presented interaction models will yield the same predictions as the non-interaction model. The fifth and highest block is responsible for the retardation effect during the sixth block

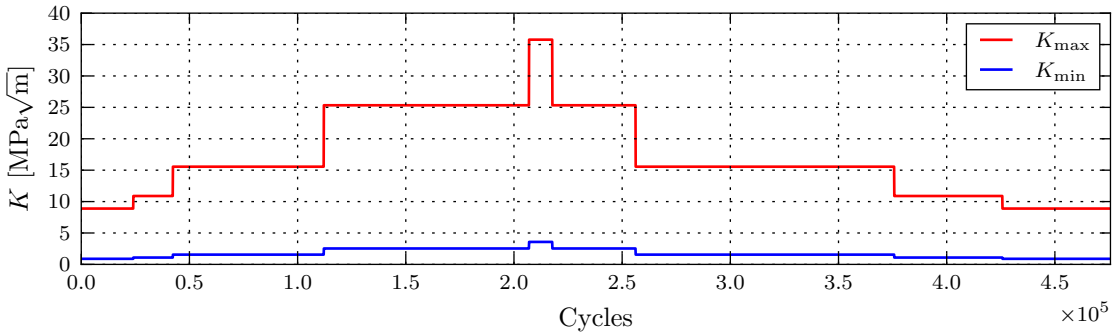

(a) LHL sequence, specimen A

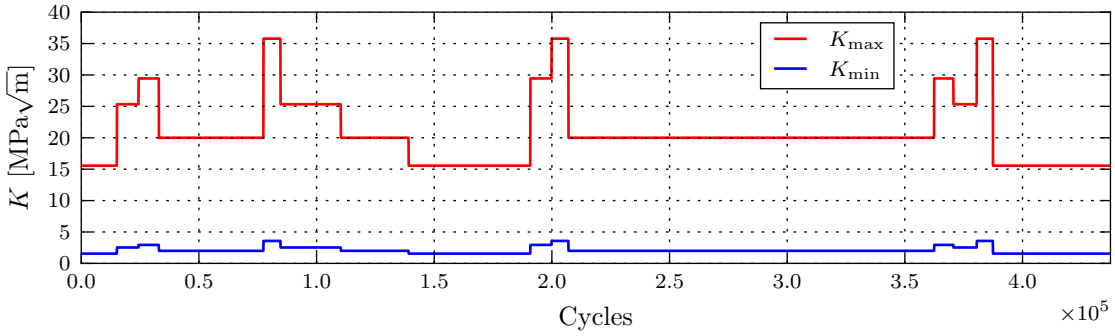

(b) SR sequence, specimen A

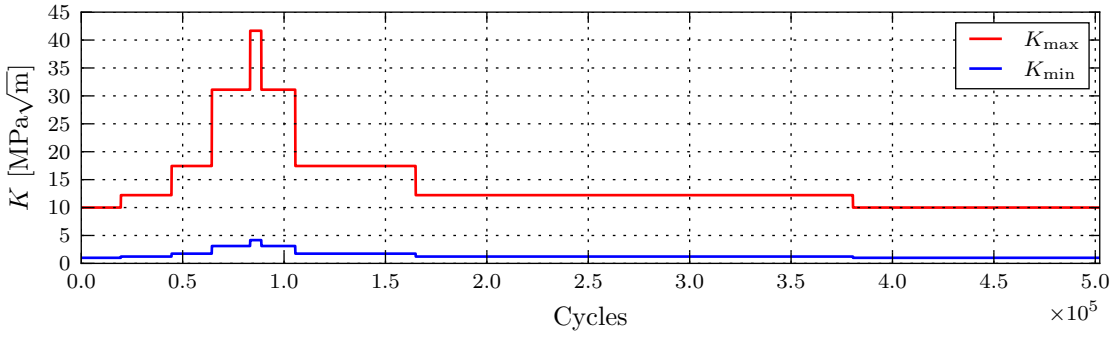

(c) LHL sequence, specimen B

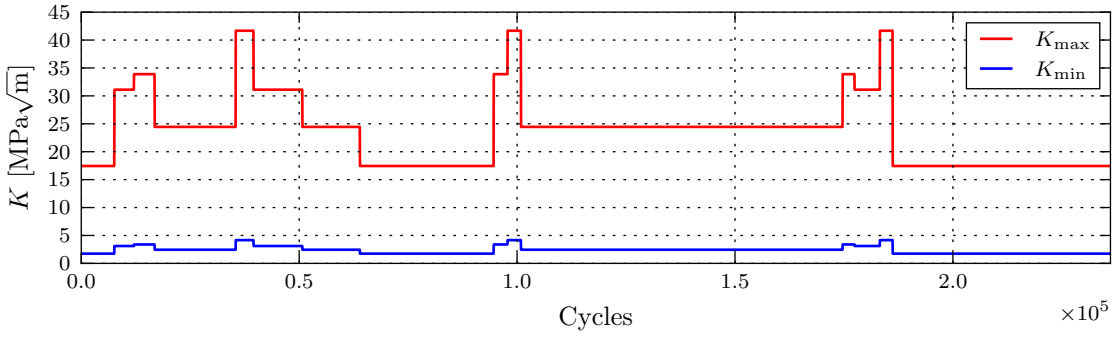

(d) SR sequence, specimen B

Figure 4.27.: Applied load histories

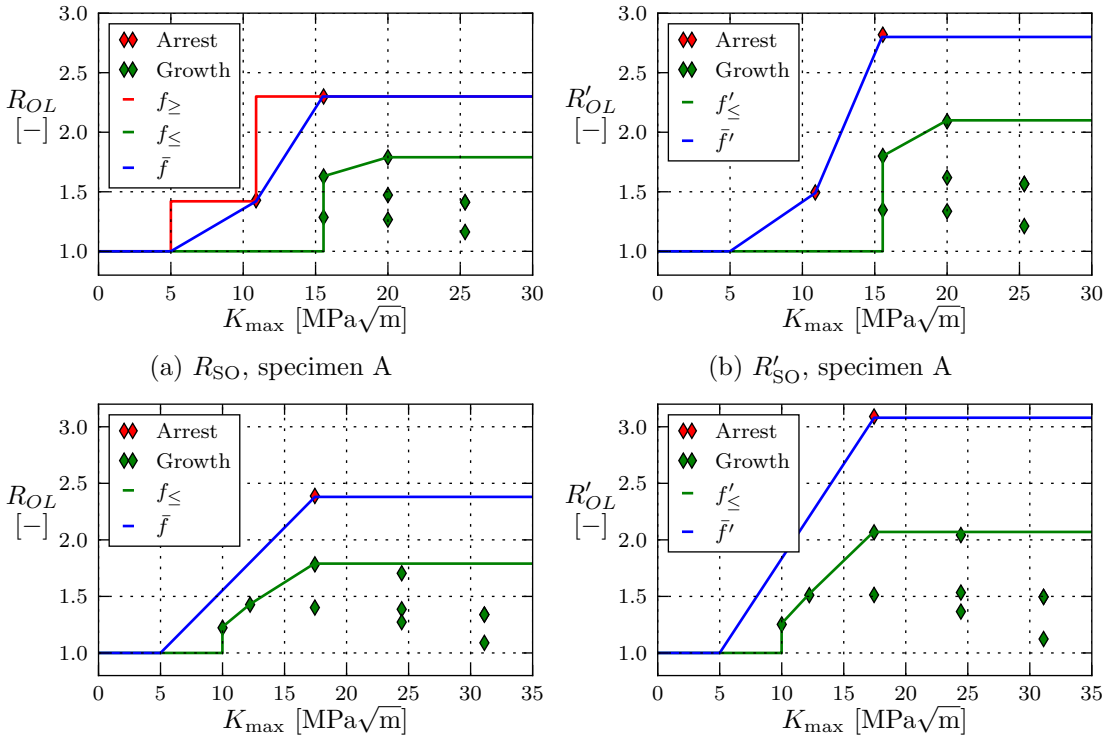

(a) R_{SO}, specimen A

(b) R'_{SO}, specimen A

(c) R_{SO}, specimen B

(d) R'_{SO}, specimen B

Figure 4.28.: Estimation of (corrected) shut-off overload ratio

and so on. The moment from which retardation can be observed is indicated by the red line. In the remainder of this section only simulations for the last 4 blocks will be displayed in order to improve the level of detail. For specimen A crack arrest was observed during the last 2 blocks, while the crack in specimen B kept growing until the very end, although rather slowly. Ideally, simulations should predict the occurrence of crack arrest. In the following paragraphs, Wheeler and Willenborg models will be discussed separately.

Wheeler models Simulation results of the different Wheeler implementations for specimens A and B can be found in Figures 4.30a and 4.31a respectively. The first model to discuss is the original Wheeler model. A plane strain plastic zone estimated with the LEFM approach is used, as Wheeler did initially [6]. By fitting this model an optimized value for w is obtained, which will later be used for the semi-random sequence in order to check its general applicability. It should be noticed that retardation is both under- and overestimated for separate blocks. Therefore, the obtained optimized value is the result of averaging out overestimations and underestimations.

Next, the modified Wheeler model is examined for the upper and lower bounds presented in Figure 4.28. Consequently, the possible range for modified Wheeler pre-

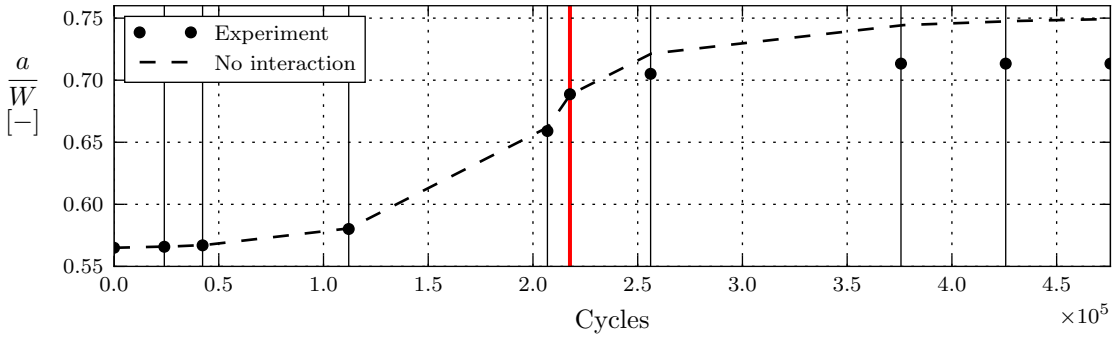

(a) specimen A

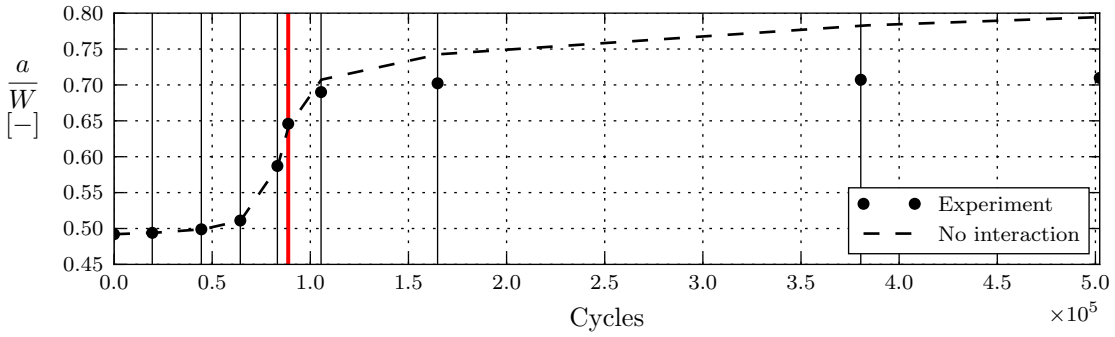

(b) specimen B

Figure 4.29.: Comparison of non-interaction model prediction and measured crack growth for the low-high-low sequence

dictions based on the plane strain SY plastic zone is given by the blue and green dashed lines. For specimen A, crack arrest is correctly predicted by both bounds as expected, since the definition of these bounds is based on the very same experiment that we are trying to predict. For specimen B, the lower bound simulation incorrectly predicts crack arrest. This is due to the fact that the retardation effect caused by the block before the last overload block is still present.

The last Wheeler model to discuss is the extended Wheeler model, which was introduced in this dissertation. A major increase in retardation is observed when this model is employed. By comparing the extended Wheeler model (solid blue line) to the modified Wheeler model (dashed blue line) for the upper bound, it can be observed that the proposed correction mainly has influence for the first two blocks. It is exactly for these blocks that $K_{\max,\mathrm{OL}}$ is relatively high (τ relatively small) and that the largest deviations from plane strain conditions occur. Although α is similar to the LEFM-value for these smaller τ-values, more retardation is predicted by the extended Wheeler model. The reason for this is the smaller α after the overload. The smaller regular plastic zones results in lower ϕ-values and more retardation. The modified Wheeler prediction for an LEFM plane strain plastic zone was added to illustrate this argument, and the prediction is indeed in between the others. The lower bounds on

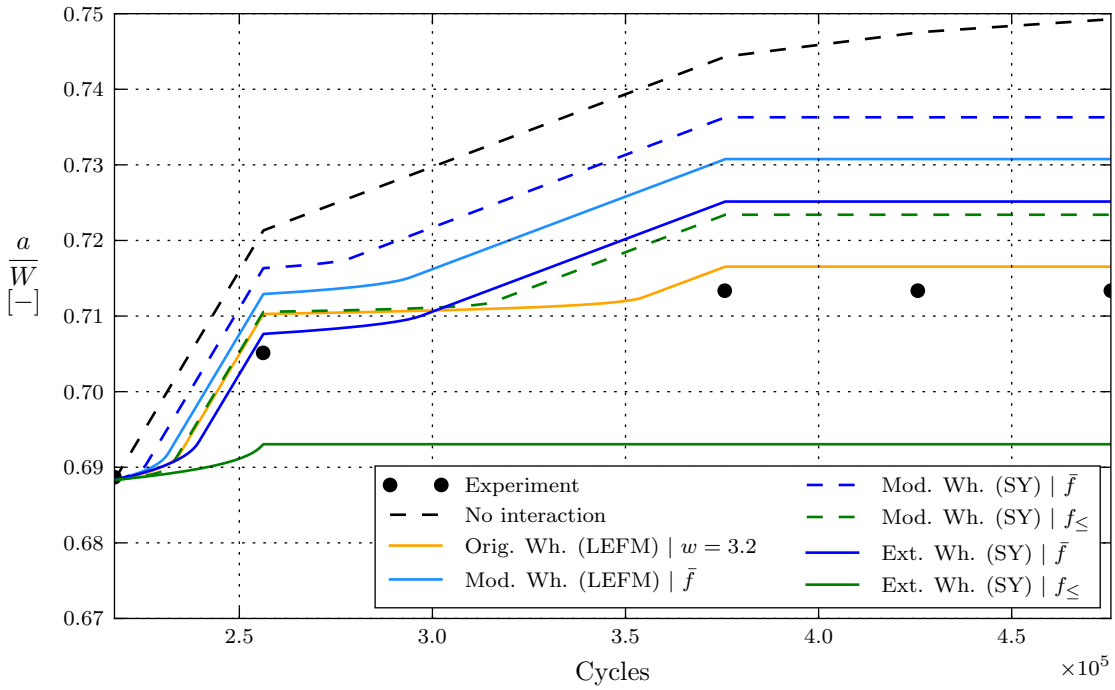

(a) Wheeler models

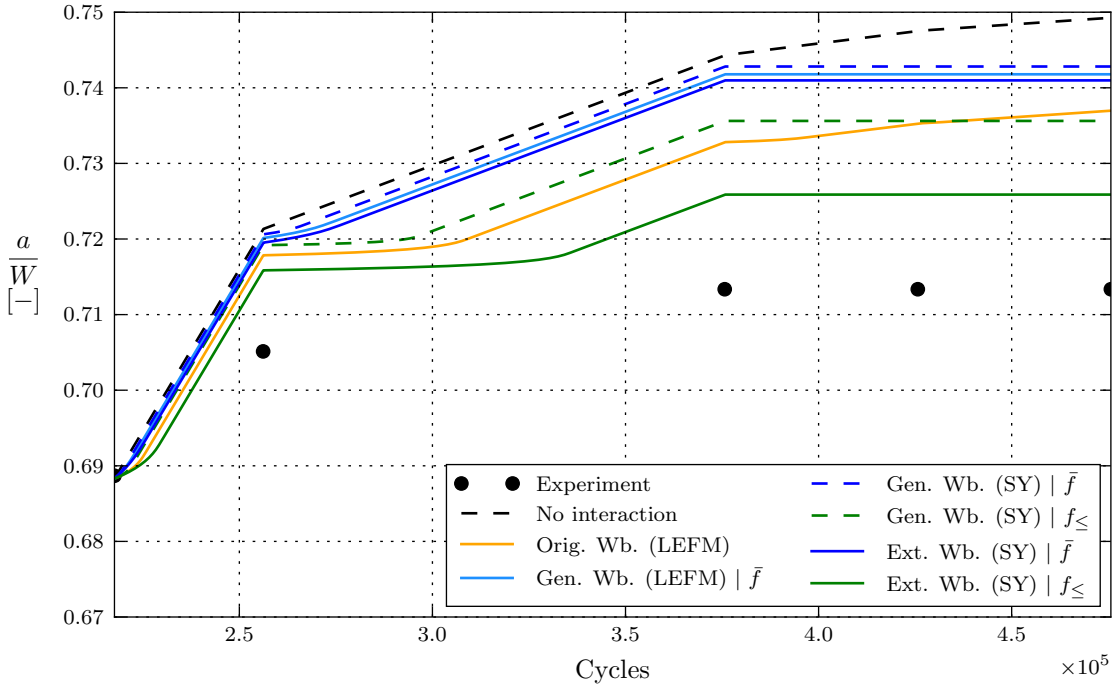

(b) Willenborg models

Figure 4.30.: Simulation results for LHL sequence of specimen A

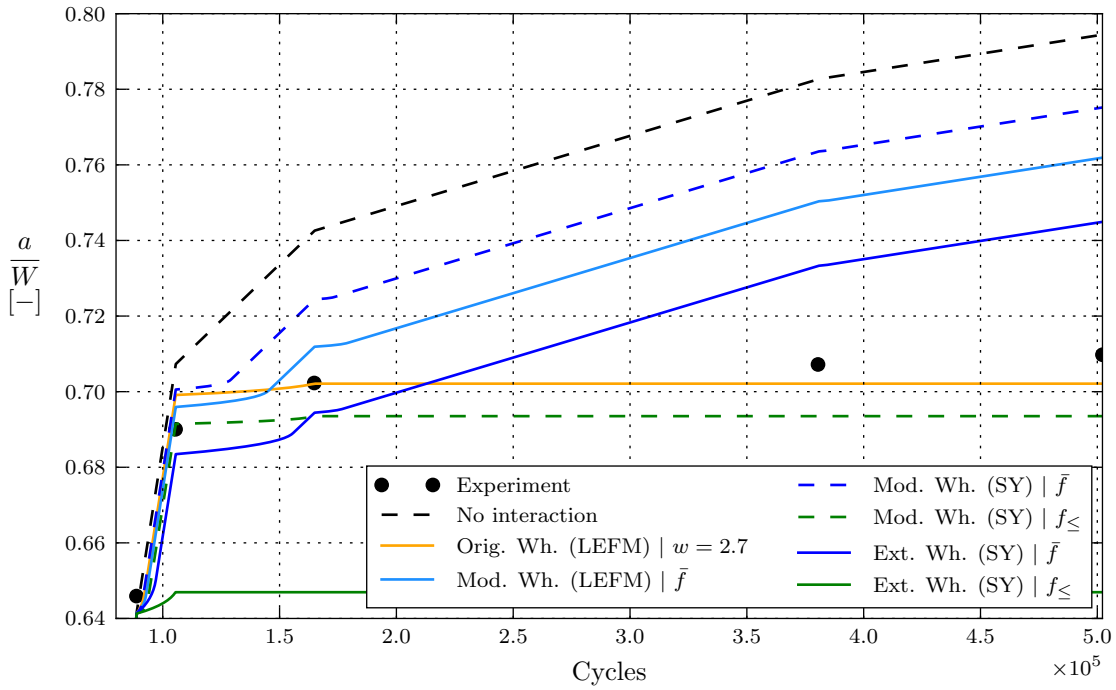

(a) Wheeler models

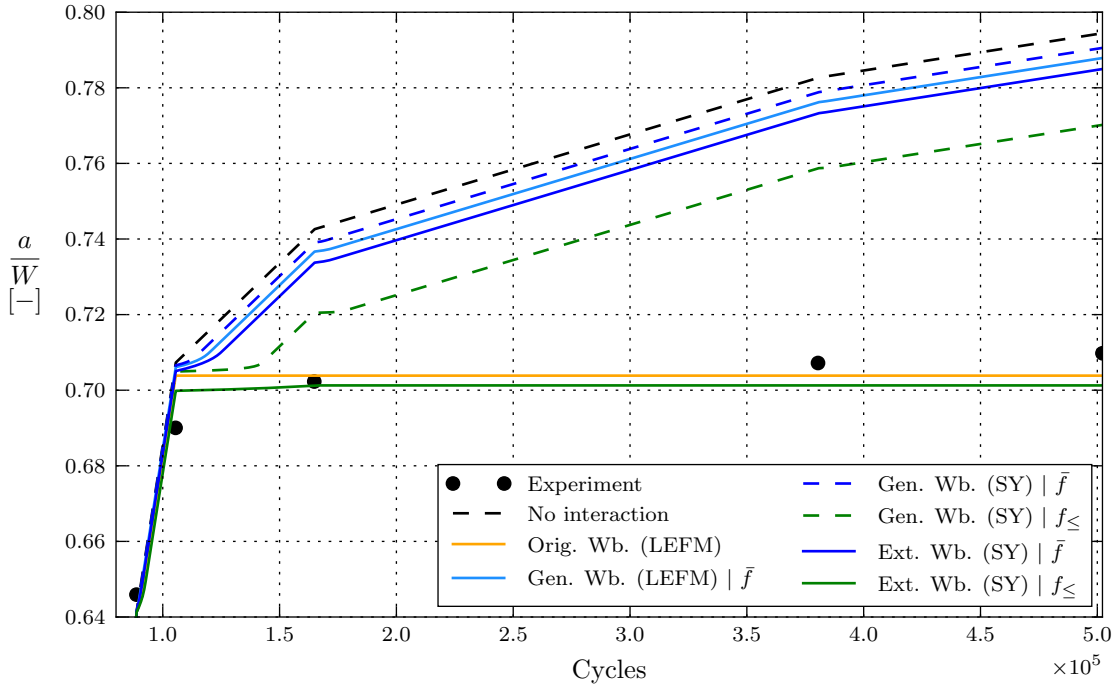

(b) Willenborg models

Figure 4.31.: Simulation results for LHL sequence of specimen B

the other hand predict too much retardation from the start on. This may be caused by the fact that for higher $K_{\max}$, R_{SO}-values are probably more towards the upper bound. For the extended Wheeler model in general, care should be taken to transform R_{OL} to R'_{OL} as described. It was observed (not shown) that failure to take this correction into account often resulted in premature crack arrest predictions.

Willenborg models Simulation results for the Willenborg models are found in Figures 4.30b and 4.31b. First of all, the original Willenborg model is examined. Since no experimental parameters are involved, the curves are as they are. A large difference between specimen A and B can be observed. For specimen A the prediction is actually quite good, except for the failure to predict crack arrest. For specimen B crack arrest is predicted prematurely despite an overload ratio below 2. These two errors are due to the fact that the original Willenborg model does not account for R_{SO} and ΔK_{th} respectively.

As for the generalized and extended Willenborg models, observations and explanations are quite similar to those given for the modified and extended Wheeler models. As expected, the LEFM-variant of the generalized Willenborg model lies between the models based on an SY plastic zone. The overall impression is that Willenborg models generally predict less retardation than the Wheeler models.

4.3.3. Semi-random block load sequence

The simulation results for the semi-random (SR) block load sequence are given in Figure 4.32. The original models (both Wheeler and Willenborg) give good correlation for one (specimen A) and bad correlation for another (specimen B). This might explain why these original models are still widely used in literature, as both may agree well in different circumstances. Discrepancies might be explained by their lack of a solid theoretical background. It can be concluded that these models are not suitable for application in general.

For the more advanced models, only predictions for the upper bound estimation of R_{SO} are shown. For the Willenborg models, the same trend as for the LHL sequence is noticed: retardation is underestimated. The prediction of the modified Wheeler model is somewhat better. The most significant result however is the accurate performance of the extended Wheeler model, especially for specimen B as correlation is near-perfect. These results might be explained by having a look at the applied load histories in Figures 4.27b and 4.27d. The maximum load (for which the correction for variable α had the largest influence) occurs multiple times. The effect of variable α was not accounted for by the other models, therefore explaining the difference in performance.

It should be noted that for specimen A, agreement of original Wheeler model is better than that of the extended Wheeler model. However, comparing both is 'unfair' since the original Wheeler model has an empirically tuned w-value, whereas the extended Wheeler model has a fully theoretical background.

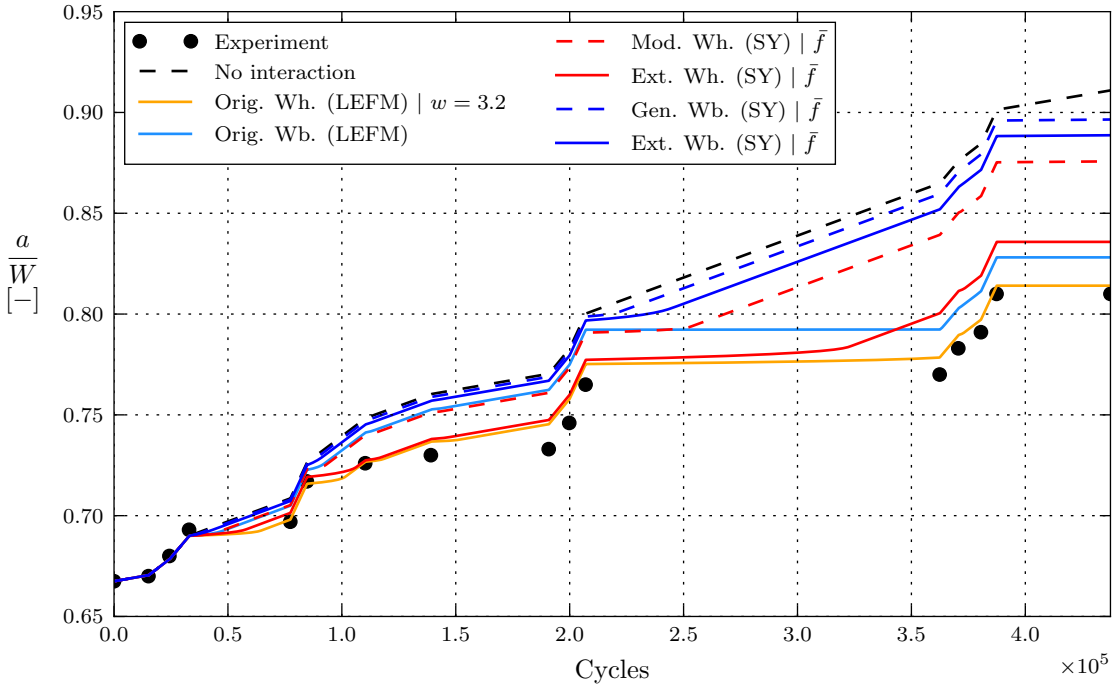

(a) specimen A

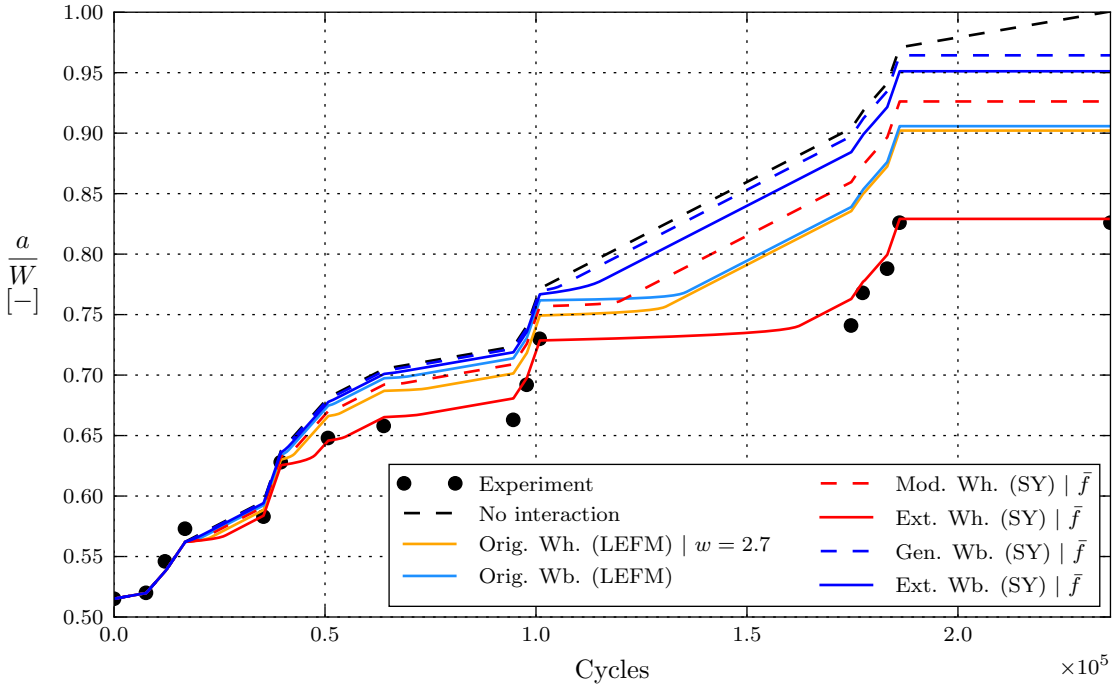

(b) specimen B

Figure 4.32.: Simulation results for SR sequence

5. Analytical vs. XFEM-based stress intensity factor solution

5.1. The eccentrically-loaded single edge crack tension specimen

The standardized geometry of an ESET specimen, which was introduced earlier, is repeated here in Figure 5.33 for practical purposes. W, the width of the specimen, characterizes the specimen size as all other dimensions are scaled accordingly, except for the thickness t. It is recommended in ASTM Standard E647-13a that t is between $1/20$ and $1/4$ of the specimen width [39]. When comparing this criterion to Table 4.1, it is clear that the maximum allowed thickness was chosen for both specimens. This explains why the specimen is predominantly in plane strain according to our analysis.

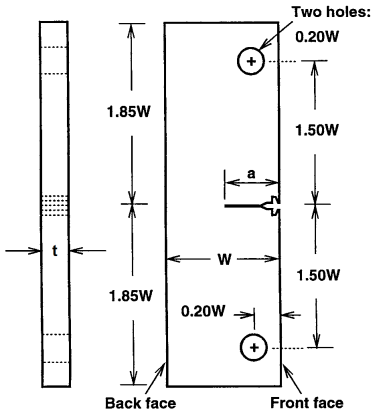

Figure 5.33.: Standard eccentrically-loaded single edge crack tension specimen [39]

Some advantages of the standard ESET specimen over other specimen types are [39]:

- elongated design provides additional working space for attaching complex displacement or strain gage measurement systems and environmental cells
- design reduces the stress parallel to crack surface, causing crack fracture paths that are more self-similar than in the standard compact tension specimen; crack curvature corrections are only required if thickness exceeds the specified limits
- lower applied forces are required for equivalent K-values compared to other specimen configurations (e.g. the middle-crack tension specimen), resulting in lower net section stress

Besides a limitation on allowed thickness, an additional validity requirement is imposed by ASTM Standard E647-13a. The K-solution presented in the next section is only valid if Eq. (5.1) is fulfilled. For specimens A and B this comes down to a maximum dimensionless crack length a/W of 0.91 and 0.85 respectively. There values were not attained during experiments so all experimental results can be considered valid. Initial crack length a_0 (denoted as a in Figure 5.33) after pre-cracking is often aimed around an a/W-value of 0.5 [39]. In the experiments a_0 was sometimes taken higher in order to reduce loads demanded from the test rig [2].

$$W - a \geq \frac{4}{\pi}\left(\frac{K_{\max}}{\sigma_y}\right) \tag{5.1}$$

5.2. Standardized solution

A standardized solution exists for calculating the stress intensity factor K at the crack tip from the applied load P. This solution is found in Eqs. (5.2)–(5.4). K is calculated by multiplying P with a factor related to absolute size and a factor F accounting for the changing crack length. F is solely dependent on the dimensionless crack length a/W. $\xi = a/W$ is introduced to improve readability of the formulas but will not be used further.

$$K = P \cdot \frac{1}{t\sqrt{W}} \cdot F \tag{5.2}$$

$$F = \xi^{1/2}\left(1.4 + \xi\right)\left(1 - \xi\right)^{-3/2} G \tag{5.3}$$

$$G = 3.97 - 10.88\xi + 26.25\xi^2 - 38.9\xi^3 + 30.15\xi^4 - 9.27\xi^5 \tag{5.4}$$

5.3. XFEM solution

5.3.1. Modelling

First, the ESET specimen geometry is modelled in Abaqus. For this, the dimensions of specimen A (see Table 4.1) were chosen. The modelled specimen is shown in Figure 5.34. In Chapter 3 it was stressed that XFEM is claimed to be mesh-independent. Therefore, the crack can be drawn without knowledge of the mesh. The crack, indicated in red, is assumed to be a through-crack with a straight crack front. Additionally, the crack propagation direction is chosen parallel to the notch. This way, the result can be compared to the standardized solution. The starting point of the crack is at the notch tip and the crack length is input for the analysis.

In Figure 5.35, a detail of the mesh around the crack is given. Two mesh features immediately stand out, namely geometry and size. In terms of geometry, it is clear that the mesh was generated without taking the location of the crack into consideration, as the crack does not conform to the element edges. Second, the chosen mesh is extremely coarse relative to mesh sizes used in conventional FEM. No refinement was done towards

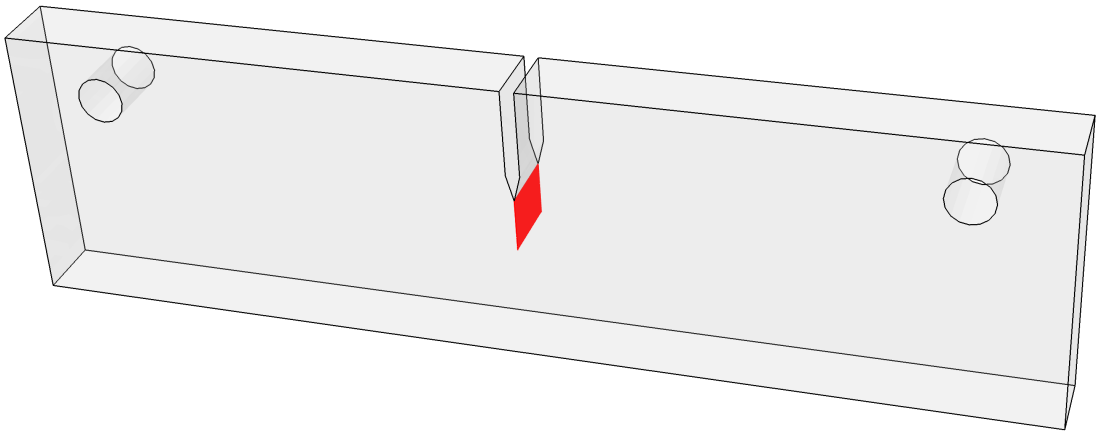

Figure 5.34.: Model of the ESET specimen

the crack tip specifically. However, a slightly increased mesh density can be noticed in the region where the crack might propagate. The reason for this is that the crack must pass through 5 to 10 elements in order to enable convergence [42]. Only linear brick continuum elements are supported [40].

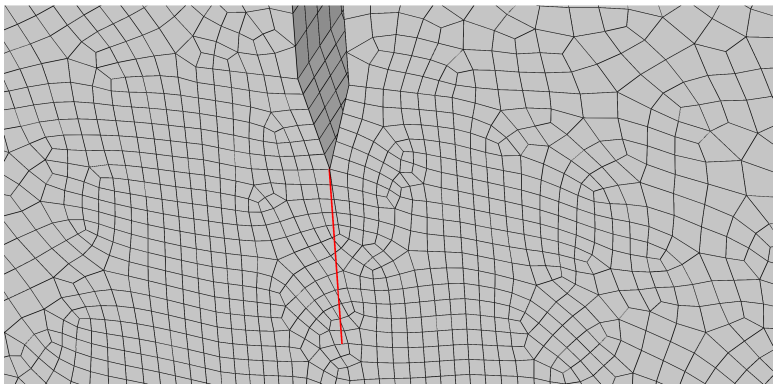

Figure 5.35.: Detail of mesh in crack region

5.3.2. Analysis

In the analysis step, an arbitrary tensile load is applied to the specimen. Here, $P = 1\,\mathrm{N}$ was chosen. This way, Abaqus returns the stress intensity factor for a unit load, denoted K_{unit}. According to Eq. (5.2) F can then be found by multiplying K_{unit} by $t\sqrt{W}$. Using this dimensionless factor F, K can be calculated for every load P independent of the absolute dimensions of the ESET specimen, since F is only dependent on a/W. In Figure 5.36a the resulting stress distribution for a unit load is given. It is clear that this distribution has little to no detail due to the coarse mesh that was used. In Figure 5.36b it can be seen that elements in which the crack has propagated are enriched. These

are indicated in red. In Figure 5.36c visualization of the XFEM crack was turned of. It gives an intuitive idea of how these enriched elements behave within a finite element analysis. The discontinuity-enriched elements stretch without taking up any load. The element containing the crack tip is clearly visible. From this figure, it is indeed clear that XFEM does not consider the crack to be part of the geometry.

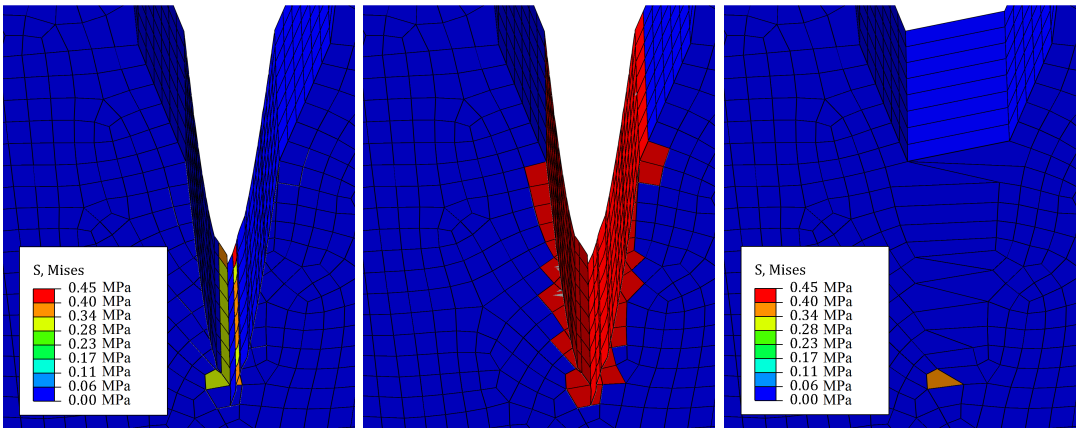

(a) open stresses (b) status (c) closed

Figure 5.36.: Visualisation of output and XFEM in Abaqus

Once the stresses are solved, Abaqus calculates the stress intensity factors according to the procedure described in Chapter 3. As previously mentioned, only output for K_I will be considered here. In the thickness direction, a stacked mesh of 8 layers was chosen. Therefore, there are 9 evaluation points along the crack front. At every evaluation point, 15 contour integral calculations are performed. These results are shown in Figure 5.37a. Only the results for points 1 up to 5 (middle element) are plotted because of symmetry. The values converge for increasing contour number and the results of the first few integrals have to be discarded. It was chosen to use contours 8 up to 12 for further calculations. These are plotted against their evaluation points in Figure 5.37b. Results deviate depending on the location of the evaluation point along the thickness direction. It is recommended to discard the results from the outer elements [45]. The remaining 25 values (contours 8 to 12 for evaluation points 3 to 7) are averaged and the final value for F is found.

Remark 5.1. During analysis it was observed that for higher a/W the results no longer converge. This instability is possibly caused by the fact that their is a lack of elements in between the crack tip and the back face. Therefore, not all element rings can be formed. Further research is needed to elucidate this anomaly.

5.4. Comparison

In Figure 5.38 the XFEM results are compared to the standardized solution given by Eqs. (5.2)–(5.4). Initial crack length was 30 mm and the crack was propagated for 20

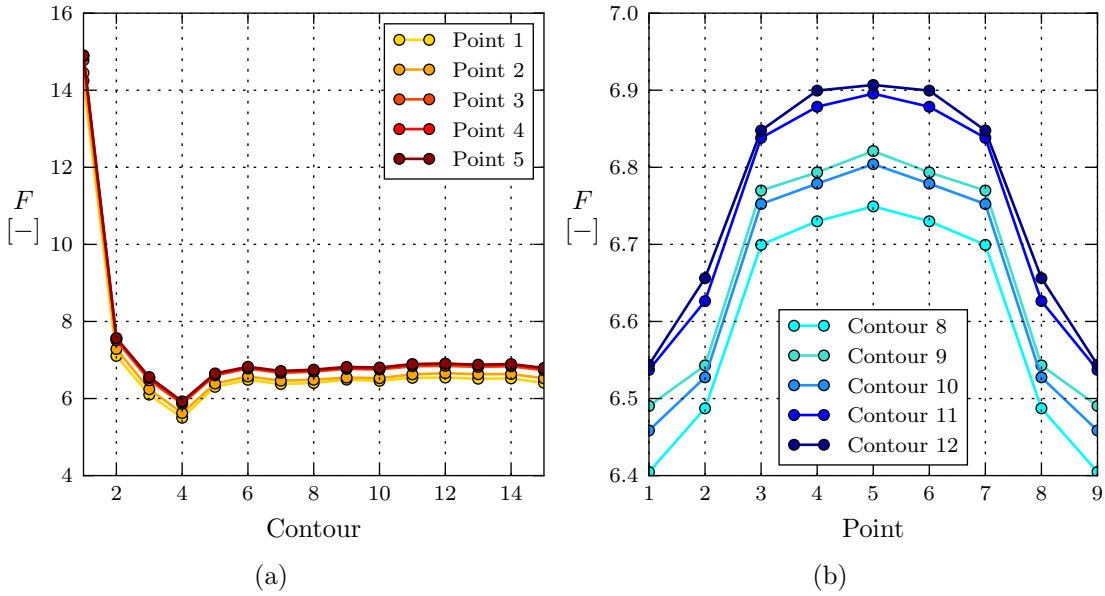

Figure 5.37.: Contour integral output

increments of 0.5 mm. Correlation is found to be near-perfect. The mean percentage error is about 0.1% and maximum absolute percentage error is only about 3%. This gives confidence to the application of XFEM for other specimen geometries.

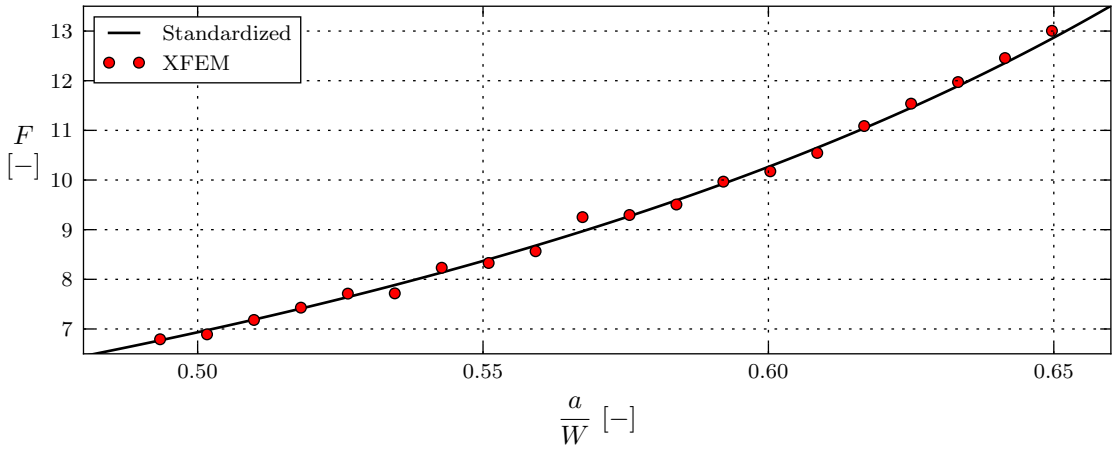

Figure 5.38.: Comparison

Part III.

SOFTWARE IMPLEMENTATION

6. Program structure

In Chapter 1 two kinds of loading conditions were distinguished. K-controlled loading is the most straightforward to use in an analysis because it is direct input for most variable amplitude fatigue crack propagation models. However, K-controlled loading can only be achieved in a lab setup. In real-life applications, force or stresses on the structure are recorded and used as input for an analysis. These must be converted to corresponding K-values before they can be used in any plastic zone model. This conversion is done by the methods described in Chapter 3.

In Section 6.1 a cycle-by-cycle algorithm is built that takes a K-controlled loading history as input. Afterwards, in light of our aim to achieve a modular program framework, the conversion of applied force to a K-value is developed as a separate module. This is discussed in Section 6.2. In Section 6.3, both parts of this thesis are finally joined as the module is implemented in the global cycle-by-cycle algorithm without modifying program flow.

6.1. Stress intensity factor-controlled loading

A schematic overview of the cycle-by-cycle algorithm that was developed to apply the plastic zone models to K-controlled loading data in order to predict crack propagation, is given in Figure 6.39.

At execution of the algorithm the actual cycle-by-cycle processing phase is preceded by an initialisation phase, consisting of two parts. The first part is initialisation of the loading history, which is broken down into a series of M blocks. Every block b is fully characterized by 3 parameters, namely the characteristics of block-specific fatigue cycle, $K_{\mathrm{min,b}}$ and $K_{\mathrm{max,b}}$, and the number of fatigue cycles N_{b}. The division in blocks is a way of efficiently representing the load history. It does not exclude spectra in which every fatigue cycle is different, since this can be represented as a series of blocks with $N_{\mathrm{b}} = 1$. Once the load history is converted into a series of blocks, the first block is loaded and cycle counter i is reset. The other initialisation part is specific to plastic zone models, which require knowledge on the initial load interaction zone state, as discussed in Chapter 2. In lab testing, the initial K_{max} is given by the precracking procedure. From this the size of the current PZ is calculated according to one of the methods described in previous chapters. Together with the initial crack length (also known from the precracking procedure) the current PZ is fully characterized. The current plastic zone is always the one formed by the latest cycle. The active plastic zone may be equal to the current one, or might be larger due to an earlier overload cycle. It can be safely assumed that at the end of this procedure no retardation effects

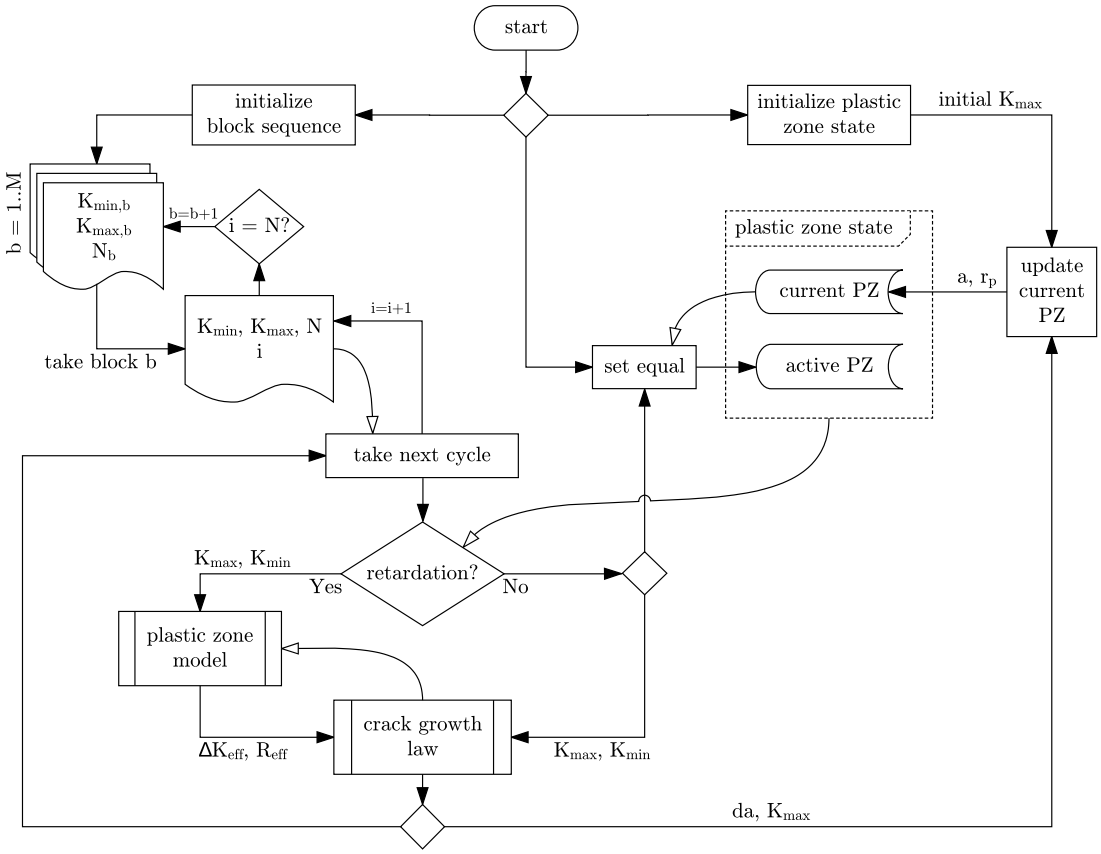

Figure 6.39.: Cycle-by-cycle algorithm for K-controlled loading history

were in play, meaning that both plastic zones are equal.

The cycle-by-cycle processing phase is started by taking the first cycle from the loaded block and increasing the cycle counter by one. Next, the condition for retardation is checked by comparing the active to the current PZ. Since both are equal at first, normal crack growth occurs and the cycle characteristics $K_{\min}$ and $K_{\max}$ (or ΔK and R) can be used directly into one of the crack growth laws presented in Chapter 2. Afterwards, the current PZ is advanced based on the obtained crack growth increment and its size is decided upon by $K_{\max}$ of the considered cycle. This normal crack growth will go on for the remaining cycles of the considered block.

Suppose now that the first cycle after an overload block is taken. Both the current and the active PZ will be relatively large beforehand, as they are the remnant of the overload block. For the first fatigue cycle of the lower block load no retardation will be predicted as the current PZ will be slightly bigger than the active PZ after the overload block. An unmodified crack increment is calculated and the location and size of the current PZ is updated by the calculated increment and by the size corresponding to $K_{\max}$, respectively. Although the location of the crack tip has advanced, the plastic zone size will be much smaller. Therefore, the elastic-plastic interface falls within the

elastic-plastic interface of the active PZ and retardation will be predicted for the next fatigue cycle of the block. In concrete terms, this means that there is a delay of 1 fatigue cycle needed for adapting the plastic zones. This is unimportant for block loading, but may become relevant in random loading conditions where each block consists of 1 cycle.

If the condition for retardation is fulfilled, the values $K_{\min}$ and $K_{\max}$ are transmitted to the plastic zone model, which will send an altered output ΔK_{eff} and possibly R_{eff} as input for the crack growth law. The obtained increment is then used to update the current PZ again. Note that the active PZ is not changed as long as retardation occurs, since it remains the largest PZ.

6.2. Implementation of stress intensity factor calculation

In case a force-controlled loading history is put into the algorithm, it is required to convert this input to the corresponding K-values. This conversion is dependent on the geometry of the structure/specimen and the current crack length. As crack growth is not known beforehand, conversion must be performed on the go. Possible ways to go about this were explored in Chapter 3 and tested in Chapter 5. The most straightforward approach is to use a standardized specimen, so that conversion from P to K can be done by standardized formulas, e.g. Eqs. (5.2)–(5.4).

To widen the application scope of the presented analysis techniques to arbitrary geometries, the XFEM method for calculating K was presented. Integrating this conversion technique into a cycle-by-cycle algorithm is not as straightforward, since it is unfeasible time-wise to do an XFEM analysis for every cycle due to the high cycle count. Therefore, a method is required that enables the calculation of K for every cycle, but only executes an XFEM analysis intermittently. The logic of this method is based on the standardized solutions, e.g. Eq. (5.2). Apparently, the proportionality between K and P is only dependent on crack geometry. This makes sense from a LEFM point of view and it can be safely assumed that this trend is applicable for other geometries as well [39]. In Eq. (6.1) this proportionality is presented by the function g and its dependence on crack geometry is explicitly shown by the argument a. The value of g can be directly found from an XFEM analysis in which the unit load is applied. This analysis yields K_{unit}, the stress intensity factor corresponding to the current geometry for a unit load.

$$\frac{K}{P} = g(a) \tag{6.1}$$

Figure 6.40 illustrates how the value of g, which is only updated intermittently, is used in order to provide a cycle-by-cycle conversion. For simplicity, it was chosen to update g whenever the crack has propagated over a user-defined distance $(da)_{\max}$. Within this distance, little variation of g is expected and neglected. At first use an analysis has to be performed to establish an initial value for g. a_k, the crack length at the last update, is set to a_0, the initial crack length. Once an initial g is established, it is

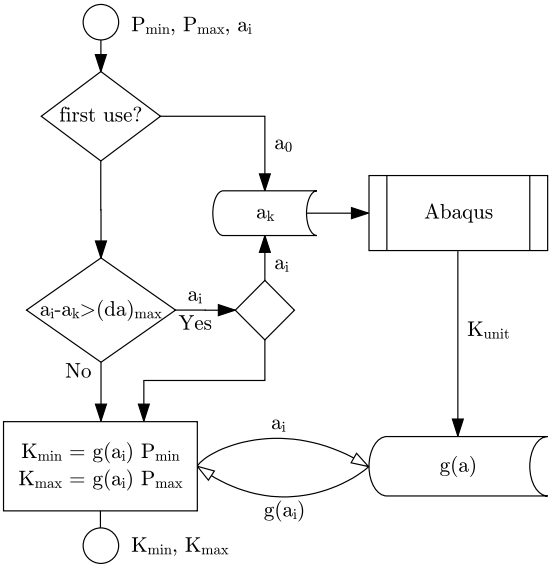

Figure 6.40.: P to K conversion algorithm

used for conversion of all subsequent fatigue cycles as long as the total crack increment since the last update does not exceed a limit value.

In between updates $K_{\min}$ and $K_{\max}$ are calculated from the 'old' solution. A possible accuracy improvement may be to extrapolate based on 2 or more previous values instead of only taking the most recent one. This is not examined in this dissertation.

6.3. Force-controlled loading

This conversion algorithm that was discussed in the previous section is added as a separate module within the cycle-by-cycle algorithm and can be considered a black box, the so called 'K solution'. In Figure 6.41 this is shown in red, along with other minor changes. A fatigue cycle is no longer characterized by K-values but by $P_{\min}$ and $P_{\max}$. Furthermore, conversion requires the current crack length, which is read from the current plastic zone. Other than that, no changes to the algorithm have to be made and the program logic is preserved.

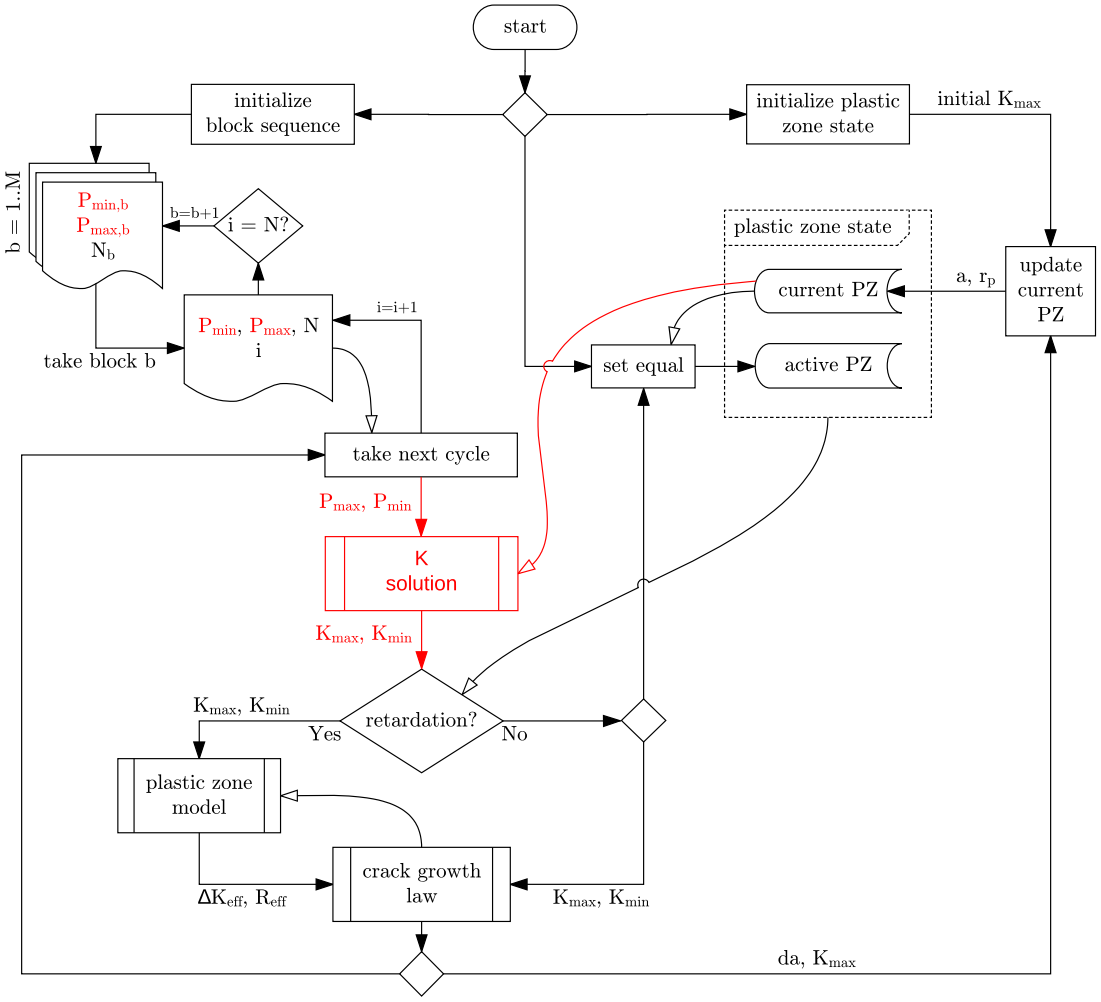

Figure 6.41.: Cycle-by-cycle algorithm extended for force-controlled loading history

Part IV.

CONCLUSIONS AND PERSPECTIVES

7. Conclusions and perspectives

In the first section, general conclusions are made by comparing the achieved results to the challenges stated in the problem statement. More detailed conclusions are omitted here as these were provided at the end of relevant chapters. Afterwards, the shortcomings and potential for extension are recognised and recommendations are given regarding the aspects that future research should focus on.

7.1. Main conclusions of this dissertation

Concerning the first challenge of this dissertation, namely variable amplitude fatigue crack propagation modelling, three requirements were imposed: cycle-by-cycle analysis, limited computational cost and the ability to yield accurate results with only a limited amount of input data. Suitable models were selected from literature and improvements were suggested. Judging by the very promising results, it can be stated that the objective of the first challenge was reached and that a potentially powerful model was developed that exceeds the state of the art. The second challenge was also successfully tackled by employing XFEM. This technique enables to convert applied forces to K-values while fulfilling the requirement of low computational cost combined with high accuracy. The third aspect, numerical implementation of the aforementioned approaches, was also successfully dealt with and special attention was paid to modularity.

7.2. Perspectives for future research

Recommendations for follow-up research are based on previously drawn conclusions in which important parameters and performance of different techniques were identified. This section is structured in accordance with the structure used throughout the dissertation.

Fatigue crack propagation modelling Based on the discussed models, their improvements and their limitations, numerous directions in which future research can go spring to mind. A distinction is made between advancing the theoretical background of the models and validating the models experimentally.

Theoretical aspect In terms of improving the theoretical foundation of the plastic zone models, the extended plastic zone models are already approaching the limit of what can be done, as all influential parameters were assumed variable and assumptions

were kept to a bare minimum. One of those assumptions was that only the retardation effects was important in the considered load histories. One could not make such an assumption and expand these models for other interaction phenomena.

As retardation is often the most prevalent effect, it is additionally advised to focus efforts on aspects in which more gains might be achieved. Such an aspect might be the influence of block length on the amount of retardation. The author believes that the main hiatus and therefore the main opportunity in improving the theoretical background of these models further lies in accounting for the number of subsequent overload cycles. This will however be a challenge as the idea that the length of a block has influence on the amount of retardation does not fit very well with the load interaction zone concept, which states that the relevant plastic zone is the one of which the elastic-plastic interface is located furthest away from the crack tip. In a block overload, such plastic zone will always be caused by the last overload cycle, therefore the length of the overload block should not have any influence. This was the main argumentation behind the assumption that the regular plastic zone models, which were developed for single overloads, are also applicable for block loading. If such an assumption is not desired, a possible way of incorporating the block load length could be to assume that α is also dependent on the plastic zone state ahead of the crack tip. This way, previous overload cycles are taken into account when the effect of the last overload cycle is calculated. This suggested method would be compatible with the load interaction zone concept and the developed models and framework could still be employed.

Note that it is not advised here to explore more accurate solutions for α as extensive research and validation can be found in literature.

Experimental aspect Before trying to characterize the different experimental input parameters in detail, attention should be paid to validate the proposed modifications of the extended plastic zone models. The main candidate that requires validation is the correction for the shut-off overload ratio used in the extended Wheeler model. A suitable experiment for this is to obtain R_{SO} for a fixed $K_{\max}$ and for different values of τ, as to capture the value in plane strain, the transition zone and plane stress. In full plane strain and plane stress (for both $K_{\max}$ and $K_{\max,\mathrm{OL}}$) $R_\alpha = 1$ since α will be constant. In the transition zone however $R_\alpha \geq 1$. If the assumed correction is indeed valid, all measurements $(K_{\max}, R_{\mathrm{SO}}, \tau)$ should collapse on the same point $(K_{\max}, R'_{\mathrm{SO}})$.

A logical continuation of this validation would be to repeat the same block sequence tests for specimens in which the τ-range is more towards plane stress. Especially for the Willenborg models, which is particularly dependent on α, such tests would unambiguously decide on its capabilities and whether any of its variants should be considered in future research.

After the correction used in the extended plastic zone models is validated, one could look at characterizing the R_{SO}-function in more detail, since it was identified as a main influencing parameter. Preferably, these experiments are performed independently in order to avoid that the values have to be derived from the block sequences that are being analysed.

Additional accuracy could of course also be attained by improving the crack growth law in the near-threshold region and by obtaining an additional Paris law curves for another load ratio so that the Walker equation parameters are experimentally established. This perspective is of minor importance since the expected gains might not outweigh the additional experimental effort.

Stress intensity factor solution The second aspect of this dissertation, determining the stress intensity factor based on XFEM, offers even more potential for expansion since a lot of assumptions were made during this basic exploration and application of the technique. When a two-dimensional analysis is desired, one could introduce a hole in the geometry to make the crack deviate from a straight path. This has to be coupled by accounting for K-components other than K_I. Also instability problems when the crack approaches the back face could be further examined. Another expansion would be to go three-dimensional. Instead of having one value for a and r_p, the plastic zone would have an actual depth and be represented by an array. The algorithm would than have to be applied for all depth positions within the vector. The crack front does no longer have to be straight and can take a more realistic shape.

Software implementation All suggested improvements, whether it be accounting for block length or enabling three-dimensional crack propagation, can be implemented into the developed framework as modules without necessitating major software changes. No extreme difficulties should be expected here. Some specific modifications to the algorithm are suggested here for residual stresses and corrosion fatigue, two effects present in offshore welded structures. Residual stress field distributions can be programmed in Abaqus and their influence is indirectly reflected in the K-value. The proportionality between P and K may then no longer be valid. The work of Acevedo et al. [42] can serve as a good starting point. A first step to facilitate corrosion fatigue in the algorithm is to add an extra characteristic to a block load, namely the frequency at which the fatigue cycles were applied, since corrosion fatigue is frequency-dependent.

References

[1] R. C. Dragt, J. Maljaars, and J. T. Tuitman. Including load sequence effects in the fatigue damage estimation of an offshore wind turbine sustructure. In *Proceedings of International Ocean and Polar Engineering Conference*, pages 199–205, Rhodes, Greece, 2016. International Society of Offshore and Polar Engineers (ISOPE).

[2] S. De Tender. *Variable amplitude fatigue in offshore structures.* Master dissertation, Ghent University, 2016.

[3] N. Micone and W. De Waele. Comparison of Fatigue Design Codes With Focus on Offshore Structures. In *Proceedings of the 34th International Conference on Ocean, Offshore and Artic Engineering.* OMAE2015-41931, ASME, 2015.

[4] S. Hertelé. *Fracture Mechanics.* Msc. course, Faculty of Engineering and Architecture, Ghent University, 2016.

[5] S. De Tender, N. Micone, and W. De Waele. Online fatigue crack growth monitoring with clip gauge and direct current potential drop. *International Journal Sustainable Construction & Design*, 7(1):1–6, 2016.

[6] O. E. Wheeler. Spectrum Loading and Crack Growth. *Journal of Basic Engineering*, 94(1):181–186, 1972.

[7] T. L. Anderson. *Fracture Mechanics: Fundamentals and Applications.* ISBN 978-1-4200-5821-5, CRC Press, 3rd edition, 2005.

[8] P. C. Paris and F. Erdogan. A critical analysis of crack propagation laws. *Journal of Basic Engineering*, 85(4):528–533, 1963.

[9] S. M. Beden, S. Abdullah, and A. K. Ariffin. Review of Fatigue Crack Propagation Models for Metallic Components. *European Journal of Scientific Research*, 28(3):365–397, 2009.

[10] X. Huang and T. Moan. Improved modeling of the effect of R-ratio on crack growth rate. *International Journal of Fatigue*, 29(4):591–602, 2007.

[11] N. E. Dowling, C. A. Calhoun, and A. Arcari. Mean stress effects in stress-life fatigue and the Walker equation. *Fatigue and Fracture of Engineering Materials and Structures*, 32(3):163–179, 2009.

[12] N. Micone, W. De Waele, and S. Chhith. Towards the understanding of variable amplitude fatigue. *Mechanical Engineering Letters*, 12:110–121, 2015.

[13] M. Sander and H. A. Richard. *Influence of loading changes on the fatigue crack growth.* PhD thesis, Gruppo Italiano Frattura, Paderborn, Germany, 2010.

[14] M. Sander and H. A. Richard. Fatigue crack growth under variable amplitude loading Part II: Analytical and numerical investigations. *Fatigue and Fracture of Engineering Materials and Structures*, 29(4):303–319, 2006.

[15] T. Machniewicz. Fatigue crack growth prediction models for metallic materials. *Fatigue & Fracture of Engineering Materials & Structures*, 36(4):293–307, 2013.

[16] J. Willenborg, R. M. Engle, and H. A. Wood. *A crack growth retardation model using an effective stress concept.* Technical memorandum 71-1-fbr, Wright-Patterson Air Force Base, Dayton, USA, 1971.

[17] J. P. Gallagher. *A generalized development of yield zone models.* Technical memorandum fbr-74-28, Wright-Patterson Air Force Base, Dayton, USA, 1974.

[18] J. P. Gallagher and T. F. Hughes. *Influence of yield strength on overload affected fatigue crack growth behavior in 4340 steel.* Technical memorandum affdl-tr-74-27, Wright-Patterson Air Force Base, Dayton, USA, 1974.

[19] T. D. Gray. *Fatigue crack retardation following a single overload.* Technical memorandum affdl-tm-73-137-fbr, Wright-Patterson Air Force Base, Dayton, USA, 1973.

[20] T. D. Gray and J. P. Gallagher. Predicting Fatigue Crack Retardation Following a Single Overload Using a Modified Wheeler Model. In *Mechanics of Crack Growth*, pages 331–344. ASTM STP 590, Philadelphia, USA, 1976.

[21] G. A. Harmain and S. H. Qureshi. A simulation study on fatigue with single and block overloads. *Transactions of The Indian Institute of Metals*, 63(2-3):581–585, 2010.

[22] B. K. C. Yuen and F. Taheri. Proposed modifications to the Wheeler retardation model for multiple overloading fatigue life prediction. *International Journal of Fatigue*, 28(12):1803–1819, 2006.

[23] X. Huang, T. Moan, and W. Cui. An engineering model of fatigue crack growth under variable amplitude loading. *International Journal of Fatigue*, 30(1):2–10, jan 2008.

[24] G. R. Irwin. Linear fracture mechanics, fracture transition, and fracture control. *Engineering Fracture Mechanics*, 1(2):241–257, 1968.

[25] D. S. Dugdale. Yielding of steel sheets containing slits. *Journal of the Mechanics and Physics of Solids*, 8(2):100–104, 1960.

[26] M. A. S. Torres and H. J. C. Voorwald. Effects of Selective Variable Amplitude Loading on Fatigue Crack Growth. In *8th International Conference on Fracture*, pages 151–155, Kiev, Ukraine, 1993. Gruppo Italiano Frattura.

[27] H. J. C. Voorwald, M. A. S. Torres, and C. C. E. Pinto. Modelling of fatigue crack growth following overloads. *International Journal of Fatigue*, 13(5):423–427, 1991.

[28] W. Guo. Three-dimensional analyses of plastic constraint for through-thickness cracked bodies. *Engineering Fracture Mechanics*, 62(4-5):383–407, 1999.

[29] J. Schijve. Four lectures on fatigue crack II. Fatigue cracks, plasticity effects and crack closure. *Engineering Fracture Mechanics*, 11(1):182–196, jan 1979.

[30] W. Ramberg and W. R. Osgood. Description of stress-strain curves by three parameters. *National Advisory Committee For Aeronautics*, Technical, 1943.

[31] B. Tummers. *DataThief*. Software, http://datathief.org, 2006.

[32] H. Alawi. Designing reliably for fatigue crack growth under random loading. *Engineering Fracture Mechanics*, 37(1):75–85, 1990.

[33] B. C. Sheu, P. S. Song, and S. Hwang. Shaping exponent in wheeler model under a single overload. *Engineering Fracture Mechanics*, 51(1):135–143, 1995.

[34] W. Elber. Fatigue Crack Closure Under Cyclic Tension. *Engineering Fracture Mechanics*, 2(1):37–45, 1970.

[35] R. Pippan and A. Hohenwarter. Fatigue crack closure: a review of the physical phenomena. *Fatigue & Fracture of Engineering Materials & Structures*, 40:471–495, 2017.

[36] M. A. Meggiolaro and J. T. P. Castro. Comparison of load interaction models in fatigue crack propagation. *Proceeding of COBEM: Fracture Mechanics and Structural Integrity*, 12:247–256, 2001.

[37] N. Micone. *Variable amplitude fatigue report*. Internal report, Soete Laboratory, Ghent University, 2016.

[38] M. Abdelkader, Z. Mokhtar, B. Mohamed, M. Mohamed, and A. Abdelwaheb. Crack propagation under variable amplitude loading. *Materials Research*, 16(5):1161–1168, 2013.

[39] ASTM Standard E647-13a. Standard Test Method for Measurement of Fatigue Crack Growth Rates, 2013.

[40] J. Zhang, W. De Waele, and S. Hertelé. *Literature Review of Fatigue Simulation Approaches*. Internal report, Soete Laboratory, Ghent University, 2015.

[41] S. Pommier, A. Gravouil, A. Combescure, and N. Moës. *Extended Finite Element Method for Crack Propagation*. ISBN 978-1-84821-209-1, John Wiley & Sons, Inc., Hoboken, NJ USA, 2013.

[42] C. Acevedo, A. Nussbaumer, and J. Drezet. *Influence of Residual Stresses on Fatigue Response of Welded Tubular K-Joints*. Phd dissertation, École Polytechnique Fédérale de Lausanne, 2011.

[43] H. Dirik and T. Yalçinkaya. Fatigue Crack Growth Under Variable Amplitude Loading Through XFEM. *Procedia Structural Integrity*, 2:3073–3080, 2016.

[44] A. Hansbo and P. Hansbo. A finite element method for the simulation of strong and weak discontinuities in solid mechanics. *Computer Methods in Applied Mechanics and Engineering*, 193(33-35):3523–3540, aug 2004.

[45] M. Levén and R. Daniel. *Stationary 3D crack analysis with Abaqus XFEM for integrity assessment of subsea equipment*. Master's thesis, Department of Applied Mechanics, Chalmers University of Technology, Goteborg, Sweden, 2012.

[46] P. A. Rushton, F. Taheri, and D. C. Stredulinsky. Threshold and Variable Amplitude Crack Growth Behavior in 350WT Steel. In *Computational Mechanics: Developments and Applications*, pages 81–89. ASME, 2002.

CYCLE-BY-CYCLE SIMULATION OF VARIABLE AMPLITUDE FATIGUE CRACK PROPAGATION

L. Muys[1], J. Zhang[2,3], N. Micone[3], W. De Waele[3] and S. Hertelé[3]

[1] Ghent University, Belgium
[2] SIM vzw, Technologiepark 935, BE-9052 Zwijnaarde, Belgium
[3] Ghent University, Laboratory Soete, Belgium

Abstract: In variable amplitude fatigue of high strength low alloy (HSLA) steel components, overloads can severely retard subsequent crack propagation for a number of cycles. In order to be able to predict fatigue crack propagation with a reduced degree of conservatism, retardation has to be taken into account. Of all numerical models that have been developed over time, crack tip plasticity models are selected based on the need for a detailed and fast cycle-by-cycle simulation of high cycle. After introducing the load interaction zone concept, common to all crack tip plasticity models, the Wheeler and Willenborg models are discussed, implemented and compared to experimental data. It is concluded that the Modified Wheeler model provides the most promising results, whereas the main limitation of Willenborg models is the need for extensive experimental data.

Keywords: fatigue; variable amplitude; retardation; crack tip plasticity models; wheeler; willenborg

NOMENCLATURE

a	crack length	m
a_{OL}	overload crack length	m
ΔK	stress intensity factor range	$\mathrm{MPa}\sqrt{\mathrm{m}}$
ΔK_{th}	threshold stress intensity factor range	$\mathrm{MPa}\sqrt{\mathrm{m}}$
$K^*_{\max}$	'no retardation' stress intensity factor	$\mathrm{MPa}\sqrt{\mathrm{m}}$
r_{p}	plastic zone size	m
$r_{\mathrm{p,OL}}$	overload plastic zone size	m
r^*_{p}	'no retardation' plastic zone size	m
R_{SO}	shut-off overload ratio	-
β	plastic zone size factor	-
σ_y	yield strength	MPa

1 INTRODUCTION

The effects of variable amplitude loading on fatigue crack propagation were first observed by the airplane industry. It was found that linear cumulative damage evolution (as predicted with Miner's rule) was often ultra-conservative. Experiments revealed that after applying a single overload cycle in between constant amplitude loading cycles, crack propagation was slower than for constant amplitude fatigue [1]. This effect was called *retardation*. In an attempt to lower the degree of conservatism of a fatigue design – and thus indirectly the safety factor, material usage and cost – researchers tried to account for the retardation effect. Most studies have focused on the behavior of aluminum alloys, which were frequently used in that industry at the time [1–5].

Lately, there has been a lot of interest in the offshore industry for simulating variable amplitude fatigue crack propagation [6,7]. Offshore constructions are continuously subjected to variable loading conditions, due to various influences from sea and wind current amongst others. As this problem concerns high cycle fatigue, a first requirement for a suitable cycle-by-cycle fatigue crack propagation model is a reasonable total computation time. Additionally, the model should be able to yield satisfactory results without requiring extensive experimental material characterization. As most models have been developed for aluminum, good correlation for offshore steel grades is not guaranteed.

The ambition of this work is to study the influence of single overload cycles or a sequence of overloads, and thus to analyze a complete load history cycle by cycle. Over time, numerous methods have emerged, but most can be classified in one of 2 main categories: crack tip plasticity models and crack closure models. In general, crack closure models require extensive experimental characterization and/or numerical calculations, and thus do not meet the requirements stated above. Crack tip plasticity models however are better suited. These models are reviewed in detail in Section 2 and their implementation into an algorithm is explained in Section 3.

The behavior and correlation of the chosen models is demonstrated and discussed in Section 4. Input is taken from the work of De Tender [7,8], who performed variable amplitude block loading tests on offshore steels. The definition of the block loading schemes was based on an extensive analysis of wave spectra acting on a monopile structure. These were translated into a series of ΔK-blocks applied to eccentrically loaded side edge tensile (ESET) specimens.

2 CRACK TIP PLASTICITY MODELS

Crack tip plasticity models account for variable amplitude effects by considering the state of the material in front of the crack tip, where some regions have undergone yielding while others have not. To this purpose, the plastic zone induced at the crack tip is discussed first. Based on this, the load interaction zone concept, common to all crack tip plasticity models, is introduced and illustrated with two prominent models, the Wheeler model and the Willenborg model.

2.1 Plastic zone

Linear elastic stress analysis of sharp cracks predicts infinite stresses at the crack tip. In reality however, the stresses are finite due to a finite crack tip radius and plastic deformation in front of the crack tip [9]. The general formula for calculating the plastic zone size is given by Eq. (1).

$$r_{\mathrm{p}} = \frac{1}{\beta\pi}\left(\frac{K}{\sigma_y}\right)^2 \tag{1}$$

Two main methods for calculating the size of the plastic zone are proposed in literature [9]: Irwin's approach and the strip-yield model. According to Irwin, the plastic zone size factor β has a value of 1.0 for plane stress. For plane strain, the value is 3.0, due to suppression of yielding by the triaxial stress state. The strip-yield model predicts a value of 0.81 for plane stress, resulting in a slightly larger plastic zone as opposed to Irwin's result. For plane strain the predicted value of 5.07 deviates significantly from Irwin's calculations [10]. As neither plane stress nor plane strain are real-life scenarios, relations have been developed to include the influence of applied load and specimen thickness [11]. Willenborg [2] originally used Irwin's pane stress result while Wheeler [1] employed a plane strain value of $2\sqrt{2} \approx 2.8$, also deduced from Irwin's work.

2.2 Load interaction zone concept

The state of the material in front of the crack tip considered by crack tip plasticity models is illustrated in Figure 1. It contains the locations of all relevant elastic-plastic yield interfaces caused by current or previous fatigue cycles, and is therefore a representation of relevant loading history. In case of a single overload occurring at crack length a_{OL}, the material yields in the vicinity of the crack tip and a plastic zone of size $r_{\mathrm{p,OL}}$ is caused. Subsequent nominal loads, applied at increasing crack length a, will cause plastic zones of size r_{p} in front of the propagating crack tip. Since $r_{\mathrm{p}} < r_{\mathrm{p,OL}}$, the current plastic zone will be fully embedded in the overload plastic zone for a certain number of cycles. It is assumed that crack growth rate is reduced during these cycles. Once the current elastic-plastic interface intersects the one caused by the overload, the current plastic zone becomes the relevant plastic zone and the interaction effect disappears. Based on this reasoning, the condition for retardation becomes $r_{\mathrm{p}}^* > r_{\mathrm{p}}$ [1]. r_{p}^* represents the hypothetical size that the current plastic zone should have in order for it to touch the overload elastic-plastic interface.

As the crack propagates, r_{p}^* approaches r_{p}, and the retardation effect weakens. Willenborg [2] proposed to quantify the retardation effect by using a combination of both values, since their difference represents the proximity of both elastic-plastic interfaces. Later, the hypothetical stress intensity factor K_{max}^*, Eq. (2), corresponding to r_{p}^* was introduced [3] by assuming a constant plastic zone size factor. Evidently, load interaction occurs when the 'no retardation' stress intensity factor (SIF) K_{max}^* exceeds K_{max}.

$$K_{\mathrm{max}}^* = K_{\mathrm{max,OL}}\sqrt{1 - \frac{a - a_{\mathrm{OL}}}{r_{\mathrm{p,OL}}}} \tag{2}$$

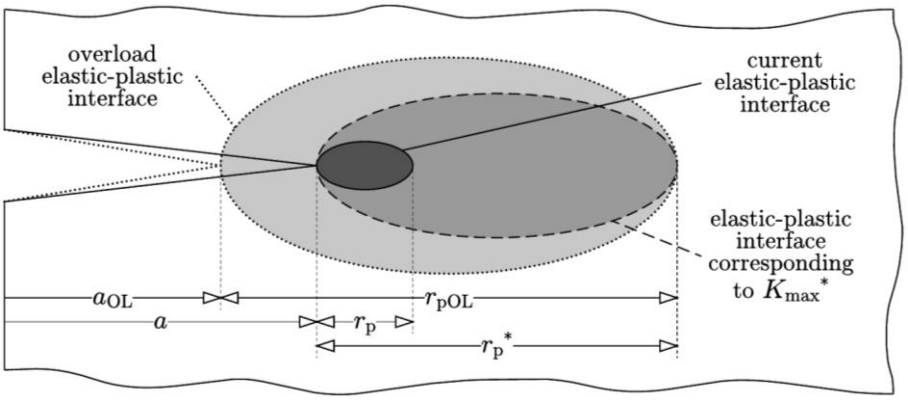

Figure 1: Post-overload plastic zones considered in crack tip plasticity models

Although the Wheeler model, Section 2.3, and the Willenborg model, Section 2.4, are based on the same load interaction zone concept, they differ in two ways: the stress intensity factors $K_{\max}^*$ and $K_{\max}$ are differently combined and the influence on the net crack growth rate is either direct or undirect, respectively. In the following sections, the model equations will be stated in terms of $K_{\max}^*$ for the sake of simplicity. However, in case the assumption of a constant plastic zone shape factor is not acceptable, the model equations have to be expressed in terms of r_{p}^*.

2.3 Wheeler

Wheeler [1] observed that fatigue lifetime predictions based on linear cumulative crack growth (as calculated with Miner's rule) were often found to be ultra-conservative. Therefore, he modified Miner's rule by introducing a retardation factor ϕ_{wh}, which takes a positive value below 1, with 1 being the case of no interaction. The Wheeler model does not alter input for the crack growth law (e.g. ΔK and R), so the straightforward Paris equation can be employed, provided that it was obtained under the correct load ratio. This is illustrated in Eq. (3), in which n is the number of applied cycles and ΔK_i is the SIF range of cycle i. Load interaction effects can potentially be simulated as the net crack growth rate is no longer independent of prior load history.

$$a_n = a_0 + \sum_{i=1}^{n} \phi_{wh,i}\, C(\Delta K_i)^m \tag{3}$$

The retardation factor, given in Eq. (4), is obtained by combining $K_{\max}^*$ and $K_{\max}$ as a ratio and raising it to the power $2w$. Originally, the shaping exponent w had to be determined experimentally for a given material and type of loading, as dependence on these factors was observed [1,12,13]. Typical reported values range from 1.0 up to 4.0. The factor 2 in the exponent is due to historical reasons. As $\phi_{wh} = 0$ is not possible (unless $K_{\max} = 0$), the Wheeler model will never predict crack arrest. This is a major difference to the Willenborg model.

$$\phi_{wh} = \begin{cases} \left(\frac{K_{\max}}{K_{\max}^*}\right)^{2w}, & K_{\max}^* > K_{\max} \\ 1, & K_{\max}^* \leq K_{\max} \end{cases} \tag{4}$$

The experimental parameter w was, besides being impractical, not applicable in general. Therefore, a theoretical relation, Eq. (5), was proposed [5,14]. It is based on the observation of crack arrest for overload values above a specific load ratio value R_{SO}, typically ranging from 1.5 to 3.0, depending on the material. It was reasoned that at the onset of crack arrest, the effective SIF range must not exceed the threshold SIF range for the material. As m is the Paris exponent, the shaping exponent can be determined from readily available material data. It is no longer a constant but a function of the material and the subsequent loading cycles.

$$w = \frac{m}{2}\left(\log\frac{\Delta K_{th}}{\Delta K} \Big/ \log\frac{1}{R_{SO}}\right) \tag{5}$$

2.4 Willenborg

Willenborg [2] assumed that retardation occurs because the stresses caused by the current load cycle are reduced due to residual compressive stresses within the overload plastic zone. This reduction was redefined in terms of a reduction in stress intensity factor [4]. Whereas Wheeler defined a ratio, Willenborg quantifies K_{red} through subtraction, without the use of an experimental parameter. The effective SIF range and load ratio are calculated by reducing both $K_{\max}$ and $K_{\min}$ by K_{red} and requiring them to be non-negative. The governing equations are given by Eqs. (6-8).

$$K_{\mathrm{red}} = K_{\max}^* - K_{\max} \tag{6}$$

$$R_{eff} = \begin{cases} \frac{K_{\min} - K_{\text{red}}}{K_{\max} - K_{\text{red}}}, & K_{\text{red}} < K_{\min} \\ 0, \; K_{\min} \leq K_{\text{red}} < K_{\max} \end{cases} \tag{7}$$

$$\Delta K_{eff} = \begin{cases} \Delta K, & K_{\text{red}} < K_{\min} \\ K_{\max} - K_{\text{red}}, \; K_{\min} \leq K_{\text{red}} < K_{\max} \end{cases} \tag{8}$$

Crack arrest happens for high overload ratios, leading to high residual stress in the overload plastic zone and $K_{\text{red}} \geq K_{\max}$. For small overload ratios ($K_{\text{red}} < K_{\min}$) only the load ratio R is modified and a crack growth law dependent on both ΔK and R is required [3].

A deeper study of Eqs. (6-8) shows that crack arrest is predicted for an overload ratio of 2 at all times. However, literature indicates that the overload value at crack arrest is variable, as discussed in Section 2.3. This can lead to unconservative predictions [4]. In reality, crack arrest happens at both a characteristic threshold SIF range and a characteristic overload ratio. To accommodate for this, a correction factor λ for K_{red} is introduced, given by Eq. (9). If this correction is used, the model is called the Generalized Willenborg Model [15]. The use of the Paris equation combined with Willenborg models was found to be a decent option in cases where the load ratio effect cannot be quantified [4].

$$\lambda = \frac{1 - \frac{\Delta K_{th}}{\Delta K}}{R_{SO} - 1} \tag{9}$$

3 CYCLE-BY-CYCLE ALGORITHM

As previously stated, crack tip plasticity models analyze each applied cycle individually. Therefore, an algorithm was developed in Python to be able to process a large amount of cycles in an automated way. A schematic overview of this algorithm is given in Figure 2.

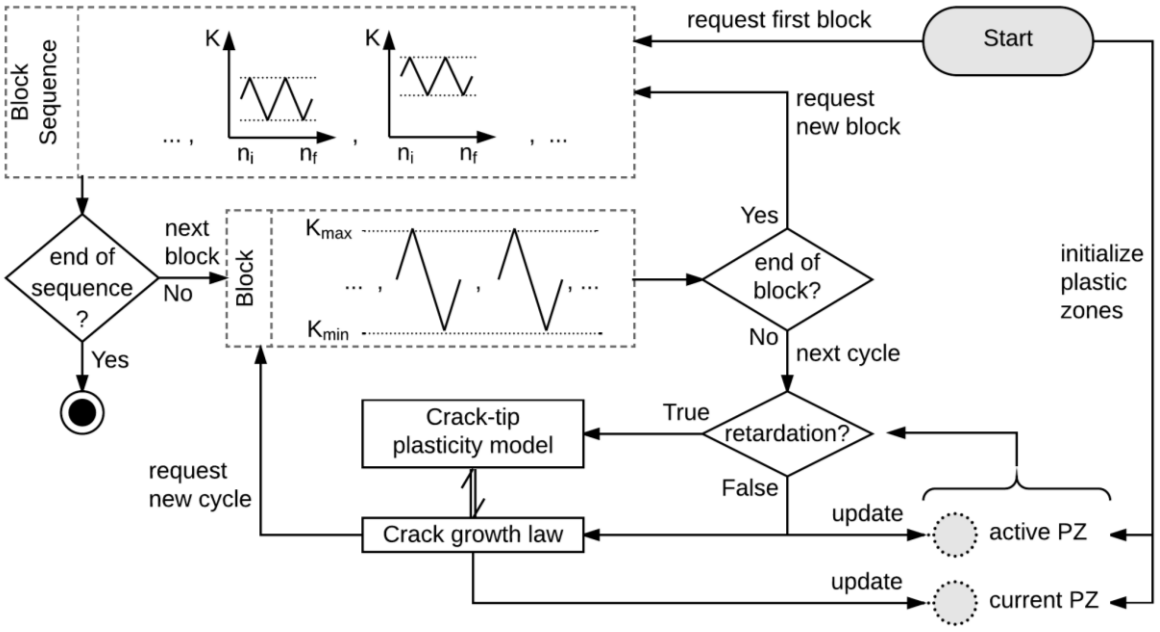

Figure 2: Schematic overview of cycle-by-cycle algorithm

Before the analysis is started, the input load history is translated into a block sequence. It is basically a series of blocks in which every block contains the maximum and minimum applied SIF of the block-specific fatigue cycle and the number of experimentally applied cycles. Once the analysis is started, the state of the load interaction zone has to be initialized. The active plastic zone is the largest plastic zone (PZ), possibly caused by an earlier overload cycle, while the current plastic zone is formed by the latest cycle. The input needed for initializing both plastic zones is derived from a fatigue pre-cracking history. It can be safely assumed that at the end of this procedure no load interaction effects were in play, meaning that both plastic zones are equal and can be defined by the initial crack length and the maximum SIF applied during pre-cracking.

After initialization, the first cycle of the first load block is loaded and analyzed. First the sizes of the current and active plastic zones are compared to decide whether load interaction occurs. After pre-cracking this is not the case, so the active PZ is updated to the current plastic zone. The crack growth law calculates the increment based on the unaltered SIF values and updates the current PZ based on the calculated increment. Further in the load spectrum, an overload can be applied. If the condition for retardation is true, the unmodified

SIF values are sent to the crack tip plasticity model, which will alter the input for – or output from – the crack growth law. The modified increment is then used to update the current PZ. Note that the active PZ is not updated since load interaction is occurring.

4 ANALYSIS RESULTS

This section compares crack growth predictions using different crack tip plasticity based retardation models against experimental data.

In the previous sections, disagreement between employed plastic zone shape factors was brought to attention. In order to compare both crack tip plasticity models objectively, a common β-factor has to be employed. This factor is dependent on both the applied load and specimen thickness, and a condition for plane strain was introduced [11]. Based on this condition, the thickness of our specimen is well above the required thickness for plane strain, even for the maximum applied load. A value of $\beta = 2\sqrt{2}$ will be used throughout this analysis.

The applied load history, a low-high-low sequence [16] is visualized in the upper part of Figure 3. The ΔK-values have been plotted with respect to the cumulative number of cycles. All loads were applied with $R = 0.1$. For the material used, the Paris law constants are available for this specific load ratio only. The influence of this limitation will be discussed further. During the first 5 blocks, no interaction effect is predicted as the load is increased for every block. For these blocks, all simulations correlate well with measured crack growth, as can be observed in the bottom part of Figure 3. For the last 4 blocks, retardation manifests and the shortcomings of linear cumulative crack growth (illustrated by the dashed line) become clear. For the purpose of visibility, graphs further in this analysis will only show the last 4 blocks.

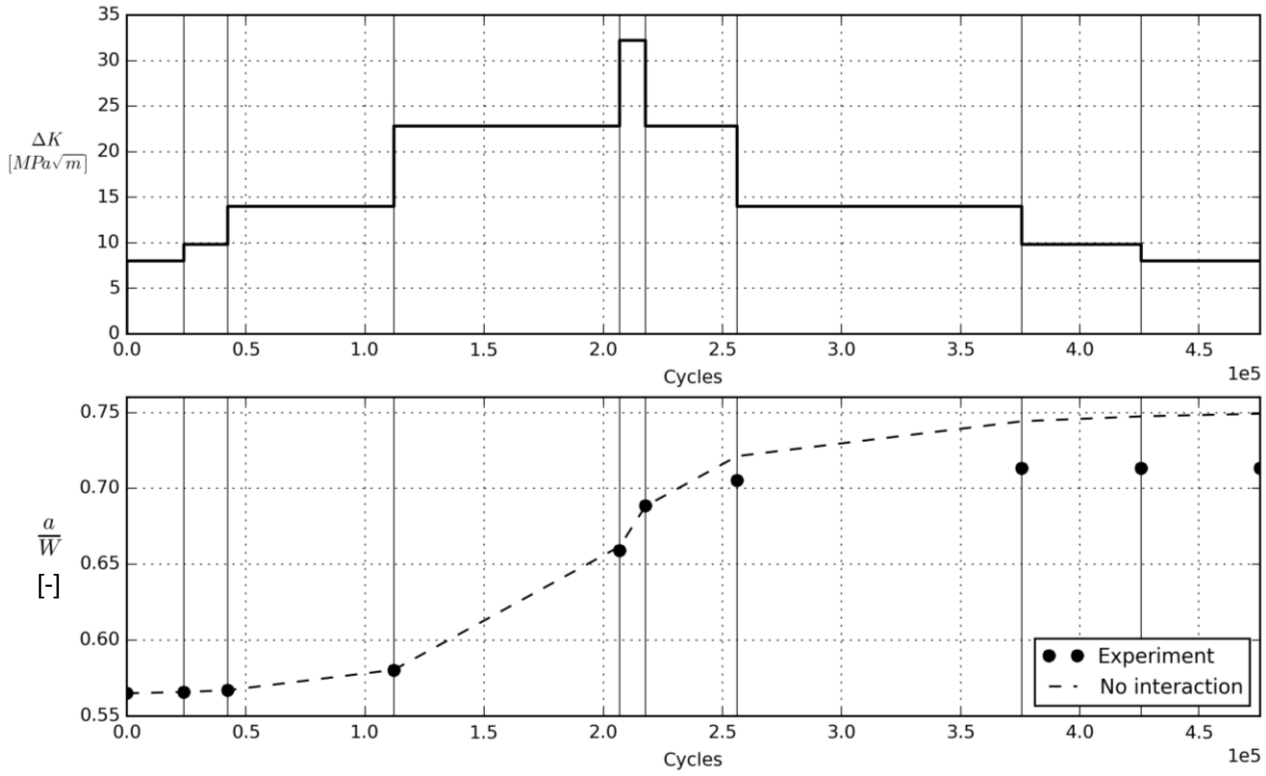

Figure 3: Input loading history (top) and experimental and predicted crack growth (bottom)

The importance of the shut-off overload ratio R_{SO} (for which crack arrest happens) has been discussed higher. For the material under investigation, a dependency on the applied load has been observed. For low SIF ranges, crack arrest even occurred for values below 2. Due to the small number of observations, only an upper bound for $R_{SO}(\Delta K)$ could be established. Therefore, the simulated Modified Wheeler and Generalized Willenborg models provide an upper bound on the predicted crack growth. Improvement of the results is likely if $R_{SO}(\Delta K)$ could be obtained in more detail.

In order to gauge the improvement that the crack tip plasticity models provide, the predictions have to be compared to the linear cumulative crack growth curve, which provides an upper bound. This upper bound is drawn as a dashed line in Figure 4 and Figure 5. The real crack growth was only measured in between loading blocks and is represented by the dotted line. Crack arrest can be noticed after the second block. Ideally, the employed models should predict such crack arrest.

The results of a comparison of the different Wheeler models are shown in Figure 4. For the original model, $w = 3.4$ was found to give the best fit with the experiment. Retardation is underestimated in the first block and overestimated elsewhere. A potential cause is the constant shaping exponent, which does not account for load and proximity to crack arrest. This inconsistency is resolved in the modified Wheeler model, which systematically underestimates the retardation effect. While the original model seems to provide better agreement, it has to be noted that it is the result of arbitrary fitting without much scientific foundation. The modified Wheeler model on the other hand is analytically derived and its earliest results are satisfactory, taking into account that it is merely an upper bound. Both models incorrectly predict crack propagation (instead of crack arrest) after the second block. This is an implication of the direct approach, i.e. correcting the normal non-zero crack growth rate by a non-zero factor, instead of altering the input for the crack growth law.

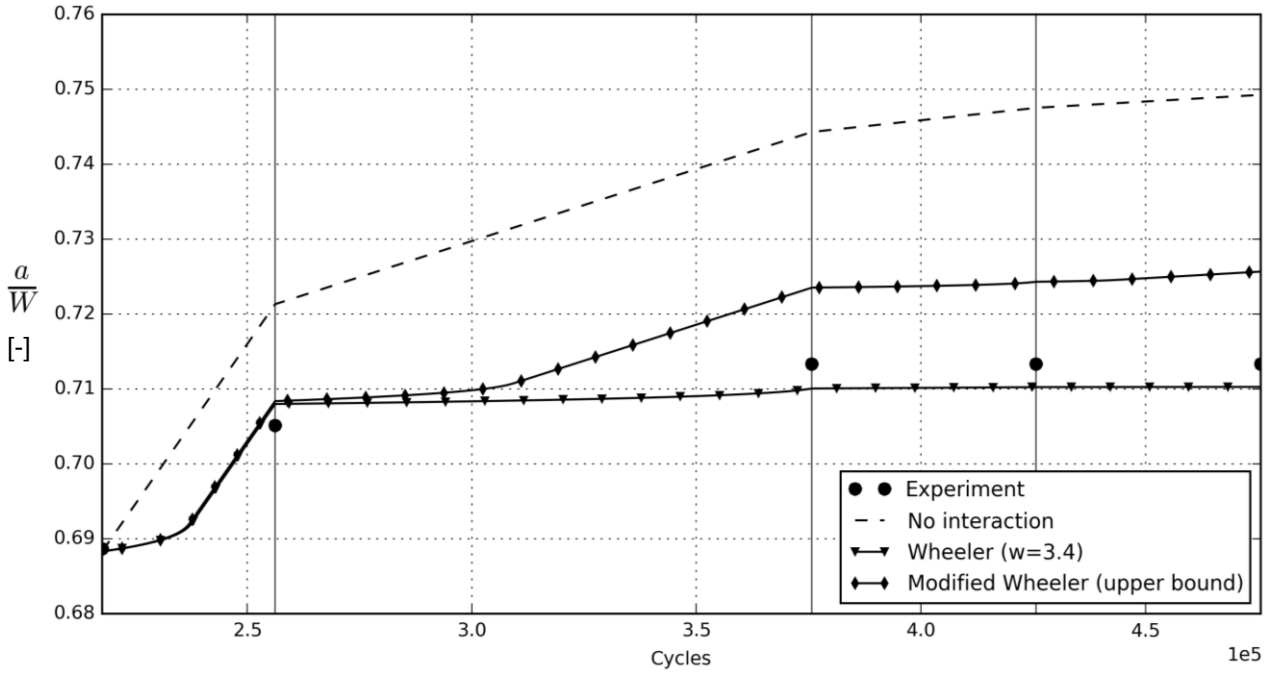

Figure 4: Comparison of the Wheeler and Modified Wheeler model

Both Willenborg models have been analytically established and do not require a fitting parameter, so they can be compared objectively. The original Willenborg model severely underestimates the retardation effect. A potential and most obvious reason is the fact that the influence of the effective load ratio R_{eff} is ignored by

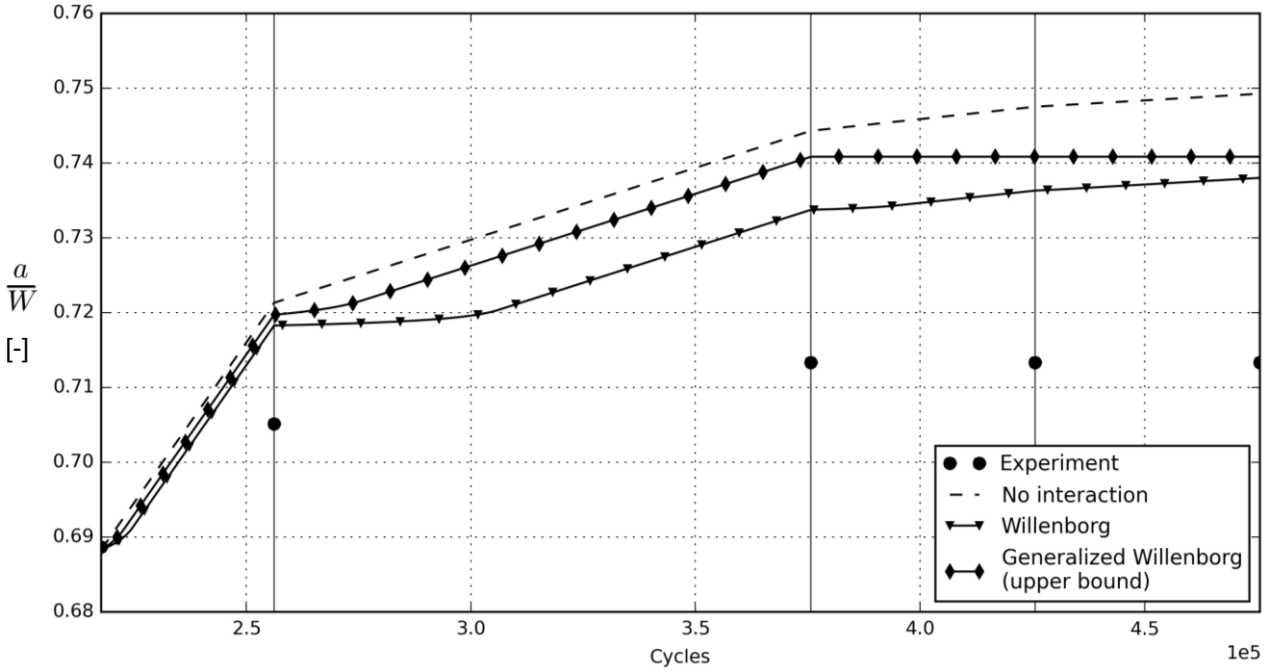

Figure 5: Comparison of the Willenborg and Generalized Willenborg model

employing the Paris law for crack growth rate calculations. It can be deduced from Eq. (6) that retardation is only quantified through the reduction of ΔK by $(K_{\mathrm{red}} - K_{\mathrm{min}})$. This way only part of the effect is captured. As $R_{\mathrm{eff}} < R$, incorporating the load ratio effect would improve predictions as crack growth rate would be lower and retardation would be higher. The Generalized Willenborg model underestimates the retardation effect even more, although crack arrest is correctly predicted. The most obvious cause is the shut-off overload ratio of the material, which takes values below 2. The proportionality factor λ thus generally decreases K_{red}, and therefore the amount of retardation, as is shown in Figure 6. An advantage of the proportionality factor is the correct prediction of crack arrest.

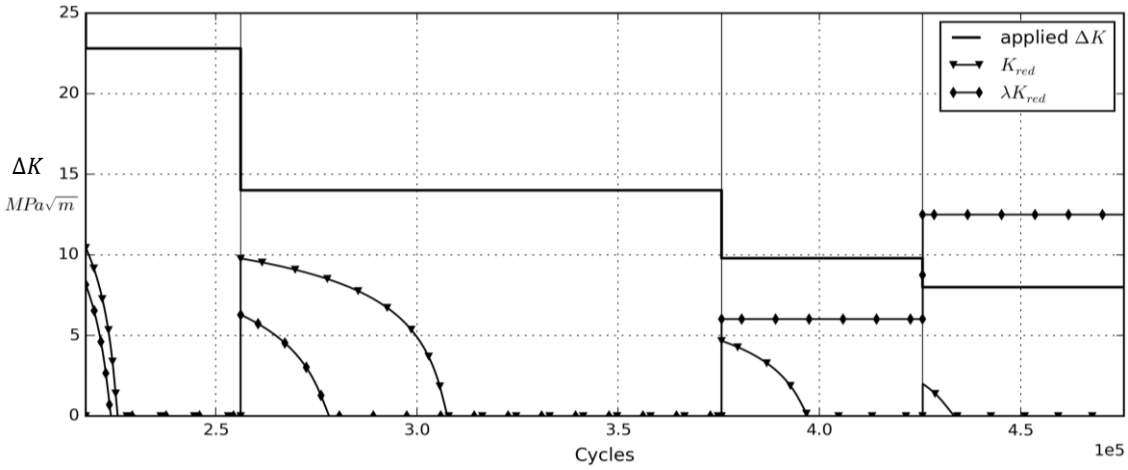

Figure 6: Influence of the proportionality factor λ on K_{red}

5 CONCLUSIONS

In this work, the capabilities of several crack tip plasticity models were compared regarding the prediction of retardation and crack arrest in variable amplitude fatigue. It is concluded that the Modified Wheeler model offers the most potential for applications in which only basic fatigue properties of the material are known. Consequently, the capabilities of the Willenborg model cannot be objectively assessed in this case, as at least one additional Paris curve is required, so that the load ratio effect can be estimated. Furthermore, all crack tip plasticity models would benefit from a more detailed determination of the shut-off load ratio as a function of applied SIF range.

6 REFERENCES

[1] O. E. Wheeler, “Spectrum Loading and Crack Growth,” *Journal of Basic Engineering*, vol. 94, no. 1, p. 181, 1972.

[2] J. Willenborg, R. M. Engle, and H. A. Wood, “A crack growth retardation model using an effective stress concept,” *Technical memorandum 71-1-FBR*. Wright-Patterson Air Force Base, Dayton, USA, 1971.

[3] J. P. Gallagher, “A generalized development of yield zone models,” *Technical memorandum FBR-74-28*. Wright-Patterson Air Force Base, Dayton, USA, 1974.

[4] J. P. Gallagher and T. F. Hughes, “Influence of yield strength on overload affected fatigue crack growth behavior in 4340 steel,” Dayton, USA, 1974.

[5] T. D. Gray and J. P. Gallagher, “Predicting Fatigue Crack Retardation Following a Single Overload Using a Modified Wheeler Model,” in *Mechanics of Crack Growth*, Philadelphia, USA: ASTM STP 590, 1976, pp. 331–344.

[6] R. C. Dragt, J. Maljaars, and J. T. Tuitman, “Including load sequence effects in the fatigue damage estimation of an offshore wind turbine sustructure,” in *Proceeding of International Ocean and Polar Engineering Conference*, 2016, pp. 199–205.

[7] S. De Tender, “Variable amplitude fatigue in offshore structures,” Master dissertation, Ghent University, 2016.

[8] S. De Tender, N. Micone, and W. De Waele, “Online fatigue crack growth monitoring with clip gauge and direct current potential drop,” *International Journal Sustainable Construction & Design*, vol. 7, no. 1, p. 6, 2016.

[9] T. L. Anderson, *Fracture Mechanics: Fundamentals and Applications*, 3rd ed. CRC Press, 2005.

[10] W. Guo, “Three-dimensional analyses of plastic constraint for through-thickness cracked bodies,” *Engineering Fracture Mechanics*, vol. 62, no. 4–5, pp. 383–407, 1999.

[11] H. J. C. Voorwald, M. A. S. Torres, and C. C. E. Pinto Júnior, “Modelling of fatigue crack growth following overloads,” *International Journal of Fatigue*, vol. 13, no. 5, pp. 423–427, 1991.

[12] H. Alawi, “Designing reliably for fatigue crack growth under random loading,” *Engineering Fracture Mechanics*, vol. 37, no. 1, pp. 75–85, 1990.

[13] B. C. Sheu, P. S. Song, and S. Hwang, “Shaping exponent in wheeler model under a single overload,” *Engineering Fracture Mechanics*, vol. 51, no. 1, pp. 135–143, 1995.

[14] T. D. Gray, “Fatigue crack retardation following a single overload,” *Technical memorandum AFFDL-TM-73-137-FBR*. Wright-Patterson Air Force Base, Dayton, USA, 1973.

[15] T. Machniewicz, “Fatigue crack growth prediction models for metallic materials,” *Fatigue & Fracture of Engineering Materials & Structures*, vol. 36, no. 4, pp. 293–307, 2013.

[16] N. Micone, W. De Waele, and S. Chhith, “Towards the understanding of variable amplitude fatigue,” *Mechanical Engineering Letters*, vol. 12, pp. 110–121, 2015.

XFEM-based cycle-by-cycle simulation of fatigue crack growth

Louis Muys

Supervisors: Prof. dr. ir. Wim De Waele, Prof. Stijn Hertelé
Counsellor: Jie Zhang

Master's dissertation submitted in order to obtain the academic degree of
Master of Science in Electromechanical Engineering

Department of Electrical Energy, Metals, Mechanical Constructions & Systems
Chair: Prof. dr. ir. Luc Dupré
Faculty of Engineering and Architecture
Academic year 2016-2017

GHENT
UNIVERSITY